Many-Body Processes in the Photophysics of Colloidal Semiconductor Nanocrystals

by

Gautham Padmanabhan Nair

Submitted to the Department of Chemistry
in partial fulfillment of the requirements for the degree of

Doctor of Philosophy

at the

MASSACHUSETTS INSTITUTE OF TECHNOLOGY

September 2009

© Massachusetts Institute of Technology 2009. All rights reserved.

Author . . . .
Department of Chemistry
July 30, 2009

Certified by. . . . .
Moungi G. Bawendi
Professor of Chemistry
Thesis Supervisor

Accepted by . . . .
Robert W. Field
Chairman, Department Committee on Graduate Students

This doctoral thesis has been examined by a committee of the Department of Chemistry as follows:

....
Professor Keith A. Nelson
Thesis Committee Chairman

....
Professor Moungi G. Bawendi
Thesis Adviser
Thesis Committee Member

....
Professor Robert W. Field
Thesis Committee Member

Many-Body Processes in the Photophysics of Colloidal Semiconductor Nanocrystals

by

Gautham Padmanabhan Nair

Abstract

In this work we have experimentally studied several aspects of two Coulomb processes that change the number of electrons and holes in colloidal semiconductor nanocrystals (NCs). Carrier Multiplication (CM) is the production of additional electron-hole pairs by collision of a highly excited carrier with valence electrons. Efficient CM would improve the performance of solar energy conversion devices, but it is weak in the bulk. Recent reports by several groups suggested highly efficient CM in semiconductor NCs. We describe here our assessment of CM using transient photoluminescence in CdSe and lead chalcogenide NCs. Biexciton radiative and nonradiative rates were determined. In our study, no detectable CM was found in CdSe NCs photoexcited at a photon energy of up to 5.9 eV, and the CM yields observed for PbSe NCs at 3.1 eV were found consistent with bulk values. Reasons for the strong disagreement with prior measurements are discussed, and the low yields are theoretically accounted for. The second part of the thesis describes two studies of the "Auger" nonradiative recombination process whereby an electron-hole pair recombines while transferring its energy to a third particle. This mechanism is responsible for the short multiexciton lifetimes in NCs. In one study, we demonstrate a direct method for determining biexciton quantum yields in single nanocrystals by photon cross-correlation (antibunching) measurements. We find significant inhomogeneity in these values, indicating a previously obscured variation in Auger recombination rates. Another set of experiments tests the conventional charging model of NC fluorescence intermittency ("blinking") which attributes off-state quenching to Auger decay, by studying single NCs with relatively long multiexciton Auger lifetimes. We find that off-state exciton quantum yields are significantly lower than the quantum yield of a biexciton and we demonstrate that multiexciton emission also shows strong intermittency. Both of these findings contradict the standard charging model. Alternatives are discussed.

Thesis Supervisor: Moungi G. Bawendi
Title: Professor of Chemistry

Acknowledgments

This thesis work and my scientific training during this time are under the joint ownership of many, as coworkers and contributors. I do not intend here primarily to express gratitude, but to attempt to answer the question of who made this work and what all it was built upon. Uniformly, they contributed freely and willingly to this project, and it does not seem they are in a hurry to be paid back. I hope they are well rewarded by watching their investment grow.

My adviser Moungi Bawendi has set up and managed this lab in such a way that freedom, resources, and good nature have been in abundance. In the context of this work, he did not go in for repairing what he perceived was already well taken care of, but focused throughout on the aspects that were in danger of being overlooked. This work is therefore simultaneously the product of independence and guidance. Aside from the scientific work, he has also set a good example to me of how to treat other scientists, be they competitors, collaborators, or simply colleagues, with humility and straightforwardness. Keith Nelson and Robert Field, my thesis committee members, have suggested interesting directions and have been there to ensure that this work remained on a productive trajectory. Like the guardrails on a mountain-side road, they contribute something important even to an uneventful journey.

The most abundant of the resources I mentioned in the lab has been expertise and a willingness to share it. The nanocrystalline materials studied in this work were prepared by Venda Porter, Yinthai Chan, Scott Geyer, Liang-Yi Chang, Jon Halpert, Hao Huang, Juwell Wu, Cliff Wong, Brian Walker, or Hee-Sun Han, either initially for their own projects or specifically for the measurements described here. Learning how to process and handle the samples was easy in a lab with the people ours has. August Dorn could be counted on to help with electronics issues and device fabrication, including making a small mirror that was very useful for the upconversion experiment. Brent Fisher and Jean-Michel Caruge were my mentors when I came in. Their attitude towards experiments and their aptitude in carrying them out has been an influence on this work. Lisa Marshall came in a year after me and acquired experience through her projects that became useful for some portions of this work. Advice from outside the group was also important. People from the Tokmakoff, Nelson, Field, and Feld groups helped our optics and spectroscopy effort when we have met challenges we have not had experience with. In particular, Kenan Gundogdu and Randy Ellingson contributed advice on how to set up the upconversion apparatus. Jing Zhao and I worked together on the blinking portion of this work, using an apparatus that she primarily constructed.

Being able to rely on things running relatively smoothly has been a luxury provided by the various staff at MIT. Li Miao, our group's administrative assistant, has taken care of many of the logistical issues essential to our work. She has cared for me well. Susan Brighton and the people at the Chemical Education office have made it as easy as possible for me to comply with the institute's regulations and procedures related to graduate education. MIT facilities and other staff have kept the institute and our lab operating.

Most of the funding for this work and my training was channeled through the Department of Energy, the National Science Foundation and, through the use of shared equipment, the National Institutes of Health. In a financial sense, this work is therefore almost entirely an investment made by the American people.

Science runs on people, but to keep this person running it was necessary for many things to come together. The lab has been an enjoyable and fun atmosphere for me because of the people in it. For instance, Brian, Scott and Lisa did not know how much time they spent talking to me until they saw a large productivity boost when I moved to another office. Peter and I would go blast the peak together. Jon, Cliff and Yinthai sparred with me in 2d electronic combat with widely varying degrees of success. Jon in particular did not hesitate to have me over at their place, sometimes just to watch a game. There were many more instances of friendship. Be assured that those that were not mentioned are not the lesser, because amongst them is also the greatest. Outside the lab I have enjoyed the company of my schoolmates. Becky Nicodemus and Taeho Shin I was fortunate to routinely run into. Outside MIT, David Chen, Joy Uyeno and Michael Owens were reliably there for me. Dalina Thrift-Viveros gave me companionship when I first came to MIT. Diane Hendrix, my housemate, has been happy to have me as a tenant for all but the first year of my study, giving me the delight of living in a home which she has so nicely kept. Then there are all the other things that make up one's existence, and usually go without saying. The people who work at the places that served me food and at the coffee shops, a city fit for wandering, smiling strangers, music from my CD player, books, and even the cold breeze and air have been a part of keeping this person running. Lastly, towards the end of these five years, just as I was anticipating the hardest part, I was fortunate to meet a true peer and best friend in Seungeun Oh. Her nuna effect made the last part not so difficult.

As to my amma, my achen, and my aniyan, I do not write about them here for the same reasons why I do not elaborate on the contributions of my arms, my eyes or my lungs.

Contents

List of Figures

Chapter 1

Introduction

Quantum systems of interacting particles often display surprising new phenomena. This text describes our efforts to understand and quantify the effects of many-particle interactions on the photophysics of colloidal semiconductor nanocrystals (NCs), also known as colloidal quantum dots.

Over the past ten years colloidal semiconductor NCs have emerged as a new material class with a wide range of promising scientific and technological applications stemming from their processing flexibility and optical properties. LEDs [1, 2], photodetectors [3], and lasers [4, 5] with NCs as optically active media have been demonstrated, and their use as single photon sources is being explored [6, 7] . In addition, a strong research effort is focused on unlocking their potential in biological imaging.

To help guide applications, the fundamental optical properties of NCs have been studied extensively, and most relevant aspects of the single exciton state structure and fluorescence are well understood. A handful of potential applications, however, rely heavily on less understood multiexcitonic effects. For example, the biexciton-exciton transition is responsible for the optical gain necessary for NC lasing [8, 9]. Carrier multiplication, which is the direct production of multiple electrons and holes after single photon absorption, could have important consequences for light-harvesting technologies. Importantly, the fluorescence intermittency that NC emission displays [10] is also thought to be due to a many-body process.

In this work we study new aspects of the photophysics of multiexcitons in NCs, we quantify carrier multiplication in NCs, and we critically examine the role of many-body processes in blinking. Before introducing those specific topics, this chapter begins with a brief description of the chemical structure of NCs and a conceptual discussion of their electronic structure.

1.1 Colloidal Semiconductor Nanocrystals

Colloidal nanocrystals are small $d \sim$ 1-10 nm crystals of semiconductors, which include CdSe and lead chalcogenides in this study, coated with an organic ligand that confers solubility (see Fig. 1-1). As with many areas of solid state physics, fundamental research has been driven by advances in the synthesis of materials. Modern preparation schemes, typically relying on pyrolysis of organometallic precursors, yield high quality, single-crystals with narrow size distributions [11, 12]. As-prepared, they are usually soluble in organic solvents like hexane for ensemble solution studies and, after purification, can be deposited by spin or drop casting for studies of single NCs.

The chemical structure of semiconductor NCs is the source of many of the advantages and disadvantages associated with them. Compared to epitaxial semiconductor dots, which are trapped within a bulk semiconductor matrix, colloidal NCs are highly versatile due to their solution processability. They can be applied as films, dispersed in polymers, or introduced into biological specimens. At the same time, the fact that the electronic excitation in an NC is delocalized over a very large number of atoms makes their optical properties less sensitive to localized chemical degradation, unlike molecular dyes which bleach rapidly when illuminated under ambient conditions.

1.2 NC Electronic structure: Envelope wavefunctions and effective mass

We discuss here the electronic structure of a semiconductor NC using a molecule as a starting point and introduce the concepts of an envelope wave function and
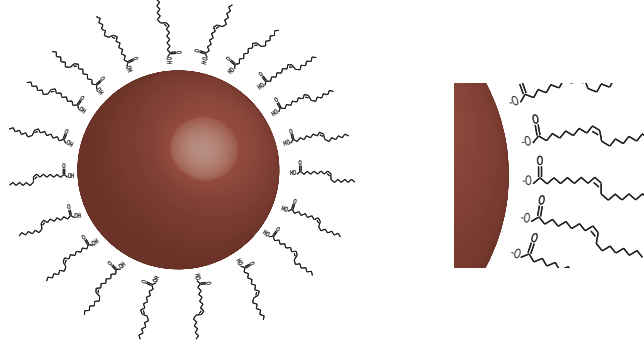
Figure 1-1: Schematic of a lead chalcogenide nanocrystal. The crystallites are capped with organic ligands (in this case oleic acid) typically present during growth. The ligands passivate the surface and confer solubility. Figure credit: Scott Geyer

an effective mass. We begin by contemplating states like those that make up the conduction band (i.e. the lowest unoccupied molecular orbital (LUMO) and higher states). The construction of the single particle electronic states in a semiconductor is not different from the problem of constructing the molecular orbitals of a molecule. We start with the Hamiltonian for the electronic degrees of freedom for a system analogous to the H_2^+ ion:

$$H = T + V_1(r) + V_2(r),$$

where T is the kinetic energy operator and V_1 and V_2 are the potential energy from Coulomb attraction to the two nuclei. The LCAO approximate solution for the molecular orbitals can be written in terms of the solutions to the isolated hydrogen atom Hamiltonians $H_1 = T + V_1$ and $H_2 = T + V_2$ as $|\psi\rangle = c_1|\varphi_1\rangle + c_2|\varphi_2\rangle$, where $H_1|\varphi_1\rangle = \varepsilon_0|\varphi_1\rangle$ and $H_2|\varphi_2\rangle = \varepsilon_0|\varphi_2\rangle$. The Hamiltonian then takes the following approximate shape:

$$H \quad \approx \quad +\varepsilon_0|\varphi_1\rangle\langle\varphi_1| \quad +\varepsilon_0|\varphi_2\rangle\langle\varphi_2| \quad \underbrace{-t|\varphi_1\rangle\langle\varphi_2| \quad -t|\varphi_2\rangle\langle\varphi_1|}_{\text{hopping term}} \qquad (1.1)$$

The latter two terms are responsible for bonding and antibonding behavior. When the "hopping parameter" t is > 0, as is the case for ssσ molecular orbitals in H_2^+, the in-phase combination $|\phi_1\rangle + |\phi_2\rangle$ is stabilized (bonding) to an energy $\varepsilon = \varepsilon_0 - t$ and the out of phase combination $|\phi_1\rangle - |\phi_2\rangle$ is pushed to a higher energy $\varepsilon = \varepsilon_0 + t$

(antibonding). In the bonding orbital, density is increased in the overlap region, so the electron is on average closer to the nuclei. These ideas extend to the case of a crystal, which we begin to analyze by considering a chain of many atoms. In the LCAO treatment:

$$H = T + \sum_i V_i(r) = \varepsilon_0 \sum_i |\varphi_i\rangle\langle\varphi_i| - t \sum_i |\varphi_i\rangle\langle\varphi_{i+1}| + |\varphi_i\rangle\langle\varphi_{i-1}|$$

Now each i corresponds to an atom position, or the index of each unit cell in a lattice. The general LCAO solution is a linear combination $|\psi\rangle = \sum \psi_i|\varphi_i\rangle$. Like in the diatomic case above, the hopping term reduces the energy of in-phase combinations of the $|\varphi_i\rangle$ and promotes the spreading out of the electron over as many sites as possible. Maximum overlap is achieved if all ψ_i are equal, and for an infinitely long chain one obtains a full $\varepsilon_0 \rightarrow \varepsilon_0 - 2t = \varepsilon_{bo}$ bonding stabilization. One can show that:

$$H|\psi\rangle = \sum \left[\varepsilon_{bo}\psi_i - t\left(\psi_{i+1} + \psi_{i-1} - 2\psi_i\right)\right]|\varphi_i\rangle \qquad (1.2)$$

We now consider only low-lying states, in which ψ_i vary only slowly with i so that $|\psi\rangle$ retains nearly fully bonding character. Then we can write our solutions in terms of a smooth "envelope" function $\psi_{env}(x)$:

$$\psi(x) = \sum \psi_i\varphi_i(x) \approx \psi_{env}(x) \sum \varphi_i(x) \qquad \psi_{env}(x_i) = \psi_i$$

Applying the Hamiltonian as written in Eqn. 1.2, one finds that the physics of the system can be described succinctly in terms of this envelope wavefunction:

$$H\psi_{env} \approx -ta^2\frac{d^2\psi_{env}}{dx^2} + \varepsilon_{bo}\psi_{env} = -\frac{\hbar^2}{2m^*}\frac{d^2\psi_{env}}{dx^2} + \varepsilon_{bo}\psi_{env} \qquad (1.3)$$

Where $a = |x_{i+1} - x_i|$ is the lattice constant. It is seen that the hopping term in the Hamiltonian acts on the curvature of the envelope wavefunction. Under the action of H, the envelope function behaves exactly as though it was the wavefunction of a particle with an "effective" mass $m^* = \frac{\hbar^2}{2ta^2}$. Stronger bonding results in lighter

effective masses, and weak bonding is associated with heavier mass.

1.2.1   Valence band states, holes

In the direct-gap semiconductors we study, the HOMO is a maximally antibonding orbital from a lower band. The localized orbitals $|\varphi_i\rangle$ overlap destructively with each other if combined in phase ($\psi_i = \psi_{i+1}$). This is analogous to the ppσ bonding situation in H_2^+, where the positive lobe of one p orbital nominally overlaps with the negative lobe of the adjacent one, and translates to a negative hopping parameter $t < 0$ in H. The discussion in the previous section can be repeated, but this time paying attention to the highest energy states, closest to the HOMO. Again Eqn. 1.3 is obtained but the effective mass m^* is negative. However, we are mostly concerned with the few unoccupied states, or holes, in the valence band. These holes behave and contribute to the total energy accounts as though they were particles with positive charge and positive mass $m_h^* = |m^*|$, for reasons that are discussed in most solid state physics books [13].

1.3   Quantum confinement

The electronic states near the LUMO and HOMO in a semiconductor nanocrystal, in the effective mass approximation, satisfy Eqn. 1.3 everywhere within the nanocrystal volume. The wavefunctions do not spread appreciably into the ligands and external material, so the electron and hole states are very similar to those of a particle in a sphere confined by a large step-like potential. The shape of the wavefunctions is determined by the geometry of the crystal. The energies of the lowest allowed electron and hole states increase as the particle becomes smaller because of the increasing curvature forced upon the wavefunctions by physical confinement within the crystal boundary. This is the origin of the well-known size effect in the optical properties of an NC, shown schematically in Fig. 1-2.
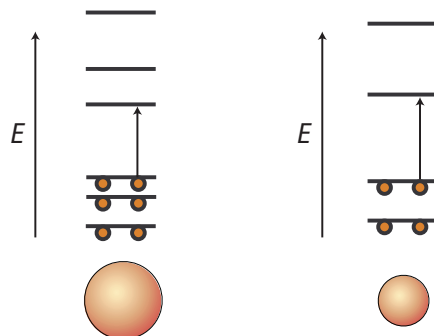
Figure 1-2: Schematic showing the effect of size on the single particle level structure in semiconductor nanocrystals. The level spacing is shorter for a larger NC than a smaller NC. The HOMO-LUMO gap is depicted with an arrow, indicating the electronic occupation change that occurs upon light absorption at the band edge.
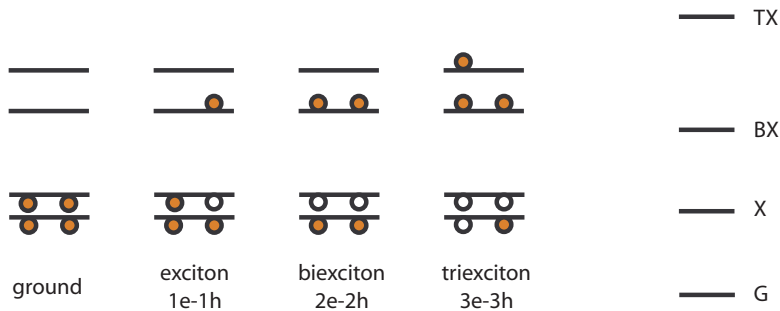
Figure 1-3: (Left) Single particle level occupation diagram. Each diagram represents a particular many-body configuration. (Right) In the many-body picture each state represents a complete specification of all particles in the system

1.4 Many-body states in nanocrystals

The simplest electronic excitation of a nanocrystal from the ground state is the promotion of an electron from the valence band to the conduction band, leaving behind a hole. The electronic states we have described in previous sections are analogous to molecular orbitals. The overall electronic state of the molecule, however, or the NC, is described by completely specifying the occupation of these orbitals. Fig. 1-3 contrasts a molecular orbital/single particle level diagram with the many-body state level diagrams for four states: ground, 1e-1h or "exciton", 2e-2h or "biexciton", and 3e-3h or "triexciton".

The energy difference between the ground state and the lowest energy 1e-1h state can be directly measured from the position of the lowest optical absorption feature

and is commonly referred to as the size-dependent "bandgap" E_g of the nanocrystal. It is equal to the HOMO-LUMO gap plus the Coulomb stabilization energy ($V < 0$) between the electron and hole. In the text we will sometimes refer to this energy as E_g or as E_{X0} when we want to stress its interpretation as the energy of the lowest exciton state. It should be kept in mind that aside from the optical properties near and below E_{X0}, the particles continue to behave in several respects as semiconductors with a bandgap equal to that of the bulk.

1.4.1 Strong confinement

To introduce the concept of strong confinement, we discuss first an exciton in the absence of any confinement at all, as in the bulk. The Hamiltonian for a bulk 1e-1h state within the effective mass approximation is:

$$H = -\frac{\hbar^2}{2m_e^*}\frac{\mathrm{d}^2}{\mathrm{d}r_e^2} - \frac{\hbar^2}{2m_h^*}\frac{\mathrm{d}^2}{\mathrm{d}r_h^2} - \frac{e^2}{4\pi\epsilon|r_e - r_h|} \tag{1.4}$$

This hydrogen-atom like potential has a class of bound solutions, referred to as excitons:

$$\Psi(r_e, r_h) = \psi_{com}(R)\psi_n(r_e - r_h) \qquad E = E_g + T_{com} - \frac{E_{\mathrm{Ryd}}^*}{n^2} \tag{1.5}$$

where R is the center of mass, T_{com} is the kinetic energy of its motion, ψ_n are hydrogen-atom-like wavefunctions, and E_{Ryd}^* is an effective Rydberg constant. The electron and hole positions are strongly correlated by their mutual Coulombic attraction, and they lie approximately within an effective Bohr radius $a_0^* = \frac{4\pi\epsilon\hbar^2}{\mu^* e^2}$ of each other. For CdSe, the Bohr radius is ≈ 5 nm, and for the lead chalcogenides it is > 10 nm. The exciton size a_0^* is determined by a balance of the kinetic energy cost, which is proportional to r^{-2}, and Coulomb stabilization, which is proportional to $-r^{-1}$.

In most colloidal nanocrystals, the electron and hole are confined to shorter length scales than a_0^* due to the finite extent of the crystallite. In this regime, the electron and hole motions are dictated by the kinetic energy term, with little influence from their Coulomb attraction. This is because the kinetic energy cost for co-localizing
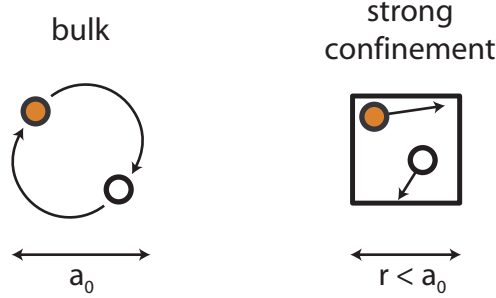
Figure 1-4: Conceptual drawing of electron-hole motion in a bulk exciton state and in a 1e-1h "exciton" state in a strongly confined nanocrystal. a_0 denotes the effective exciton Bohr radius.

them any more than they already are is too large compared to the smaller Coulomb gain. In this, strongly confined regime, the electron and hole behave like independent particles occupying conduction and valence band states ψ_c and ψ_v:

$$\Psi(r_e, r_h) \approx \psi_c(r_e)\psi_v(r_h) \qquad E = E_g + T_e + T_h + \langle V \rangle \qquad (1.6)$$

where T_e and T_h are the kinetic energies of the electron and hole envelope wavefunctions respectively and $\langle V \rangle$ is the Coulomb attraction energy. Although it is common to refer to these 1e-1h configurations as "excitons", the electron and hole are bound to each other mostly because of shared confinement in the NC (Fig. 1-4). Their motions are approximately uncorrelated. The same is the case for multiexcitonic states like the 2e-2h biexciton.

It is important to note that although the wavefunctions cease to be influenced by the Coulomb potential in the strong confinement limit, the Coulomb binding energy $\langle V \rangle \propto -r^{-1}$ in fact grows as the nanocrystal shrinks. Other Coulomb processes can also be enhanced in nanocrystals, even when they are in the strong confinement regime.

1.5 Particle-number changing Coulomb processes

Coulomb processes that change the total number of electrons and holes in a nanocrystal are the main underlying theme of this work. In Fig. 1-5 we show schematically, at
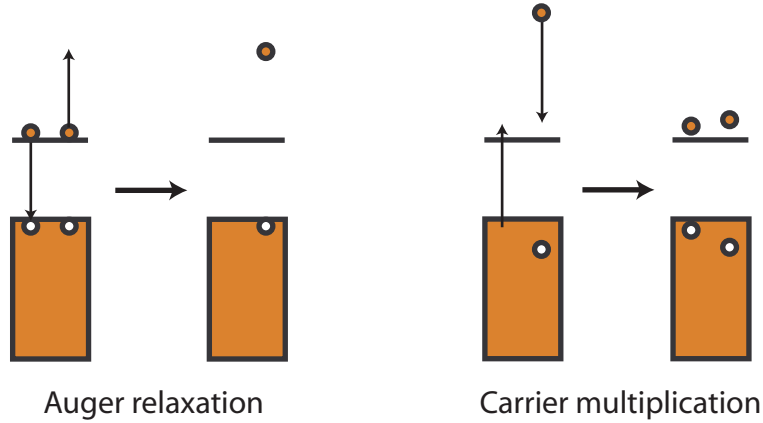
Figure 1-5: (Left) "Auger"-like recombination of an e-h pair in the presence of other carriers. (Right) Multiplication of carriers by collision of a highly excited electron (or hole) with a valence band electron.

left, an "Auger"-like process in which an electron-hole pair recombines while transferring its energy to an additional carrier, which in the diagram is an electron. The resulting hot carrier can relax down to the band edge quickly by phonon emission. The net result of Auger relaxation is the nonradiative recombination of an electron and hole. At right is shown the reverse process, known variously as carrier multiplication (CM), multiple exciton generation (MEG), or, especially in the bulk, as impact ionization (II).

1.5.1 The Auger process in nanocrystals

The fast Auger process in nanocrystals was discovered during early studies on multi-exciton photophysics. Interest in multiexcitonic states originally stemmed from their central role in NC lasing [8, 9] , and the Auger nonradiative process was soon found to be one of the most serious limiting factors to the efficiency of NC lasers. Measurements on ensembles revealed that multiexcitons in NCs have surprisingly short lifetimes, typically tens to hundreds of picoseconds instead of ∼10 ns for a single exciton, and very small quantum yields [14, 15, 9]. It was proposed, from examination of the particle size- and exciton multiplicity- dependence of the non-radiative rates, that the process responsible for the rapid MX decay is an "Auger"-like mechanism as shown in Fig. 1-5. A typical matrix element for an Auger process is given by Eqn.

1.7,

$$\langle \Psi_f | V | \Psi_i \rangle = \langle \psi_h(r_1) \psi_{e*}(r_2) | V(r_1, r_2) | \psi_e(r_2) \psi_e(r_1) \rangle, \qquad (1.7)$$

where the labels h,e and $e*$ denote band-edge valence, band-edge conduction, and hot conduction band states, and V is the Coulomb potential. The Auger process can of course also occur via a hot hole pathway.

The Auger process is not efficient in the bulk or in epitaxially grown quantum dots because of momentum conservation considerations. The initial electrons and holes occupy states close to the band-edge and have low momentum, but the final many-body configuration has a particle in a highly excited state with large momentum. It has been proposed that the Auger process is efficient in NCs because of lattice or surface defects or the abrupt interfaces that disrupt the smoothness of the low energy states' wavefunctions [16, 17], thereby relaxing momentum conservation requirements. In fact, NCs show Auger rates that are not only fast, but broadly similar for different materials, in contrast to the wide variation known to exist for the same materials in bulk form [18].

The Auger process plays an important role in the first part of this thesis, dealing with carrier multiplication in NCs. The rapid Auger decay of multiexcitons imparts a unique dynamical signature that will allow us to quantify multiexciton populations generated after high-energy photon absorption.

1.5.2 The Auger/charging model of blinking

Single nanocrystals under steady excitation display *on-off* fluorescence intermittency ("blinking") [10]. A full understanding of the mechanism behind it is the longest outstanding problem in NC photophysics. Blinking is of great practical importance because of its detrimental role in many potential NC applications. For example, their usefulness as biological trackers and single photon sources is compromised by their unreliable light emission. Efros proposed a charging mechanism [19] that remains widely accepted, in which the Auger process quenches the *off*-state emission, as depicted in Fig. 1-6. In this model, an NC blinks off when it becomes charged. Because

24
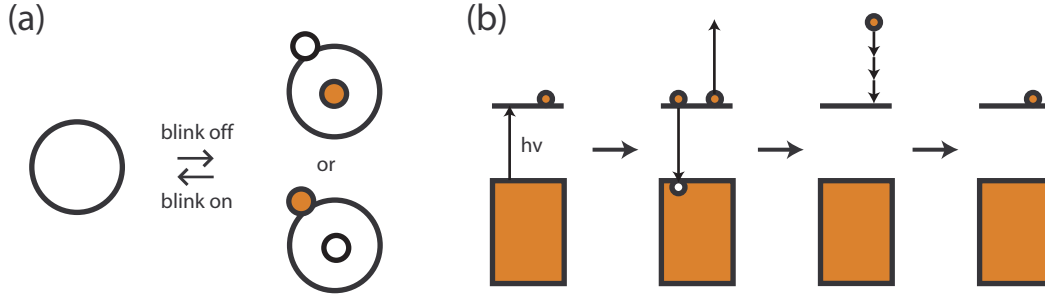
Figure 1-6: (a) The charging model suggests that an NC blinks off when an ionization event leaves the NC interior charged. (b) In a charged NC, e-h pairs generated by light absorption can be quenched by Auger recombination followed by intraband relaxation of the resulting hot carrier.

Auger rates are fast in NCs, it is thought that the nonradiative Auger recombination process mediated by this extra carrier is responsible for the low emission quantum efficiency of the "off" state.

1.5.3   Carrier Multiplication

Carrier multiplication (CM) in the form of impact ionization is a well-understood phenomenon in bulk semiconductors [20, 21]. The process consists of inelastic scattering of energetic charge carriers and valence electrons to create additional *e-h* pairs. In the bulk CM has high energy thresholds and low efficiency due to momentum conservation requirement and competition from ultrafast intraband relaxation. CM in the bulk has nevertheless found a limited but important application in commercial avalanche photo-diodes because the large applied electric fields within the devices supply the excess kinetic energy necessary multiplication. On the other hand, if efficient CM could occur following optical excitation without such an external power source, CM could have wide impact in the area of solar energy conversion.

In a typical photovoltaic cell with a single active layer, photon energy in excess of the bandgap is lost by rapid thermalization. The CM process, if effective, could harvest this excess energy into additional *e-h* pairs, boosting the maximum theoretical power conversion efficiency from 32% to >40% [22, 23], and, more importantly, widening the range of candidate materials for new solar technologies to include previously
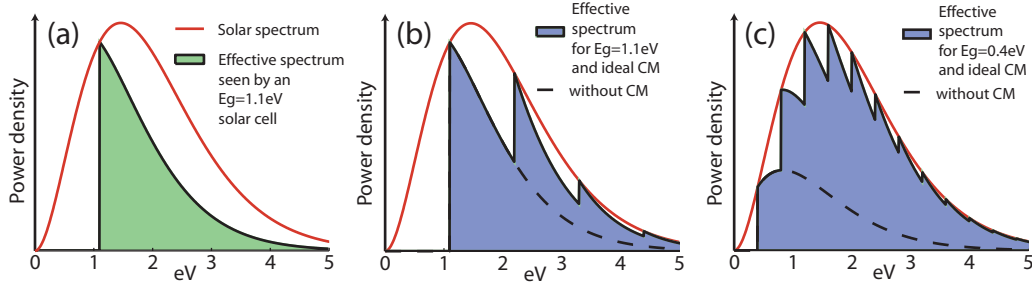
Figure 1-7: (a) Power spectrum of the sun compared to the power spectrum of the energy that can be extracted from it using a conventional solar cell with E_g=1.1eV. Loss of energy to phonon relaxation down to the band-edge limits the useful energy that can be extracted from photons with $\hbar\omega > E_g$. (b) Power spectrum for the same solar cell with carrier multiplication limited only by energy conservation. In this limit, starting at $\hbar\omega = 2E_g$, two electron hole pairs are generated instead of one, starting at $\hbar\omega = 3E_g$, three are generated, and so on. (c) Similar diagram for a smaller bandgap material, showing efficient harvesting of the solar spectrum assuming ideal CM yields.

ignored narrow-gap semiconductors (See Fig. 1-7). Strongly confined semiconductor nanocrystals (NCs) have been proposed as candidate structures for efficient CM [24] because of an anticipated relaxation of momentum conservation constraints [25, 17] and potential slowing of competing phonon-mediated intraband cooling due to the discrete electronic structure ("phonon bottleneck") [24]. The major processes relevant to CM in NCs are shown in Fig. 1-8.

Enhanced CM was first reported for PbSe and PbS nanocrystals (NCs) by Schaller et al. [26] and Ellingson et al. [27] using the transient absorption (TA) technique. Work on this material system was extended, with one report inferring the creation of up to 7 e-h by a single high energy photon based on pump-probe data [28], and a study suggesting that the enhancement occurs not only for NCs in solution but also in close-packed films relevant for potential device applications [29]. Other material systems have also been explored, with work initially showing evidence for strong CM as well in CdSe [30, 31], InAs [32, 33], and Si NCs [34].

The conclusions of the TA measurements suggested new and unique underlying physics and posed some interesting questions. First-principles theories explaining the balance of Coulomb coupling and phonon relaxation rates implied by the experiments have yet to emerge. At the same time, studies on intraband relaxation in CdSe
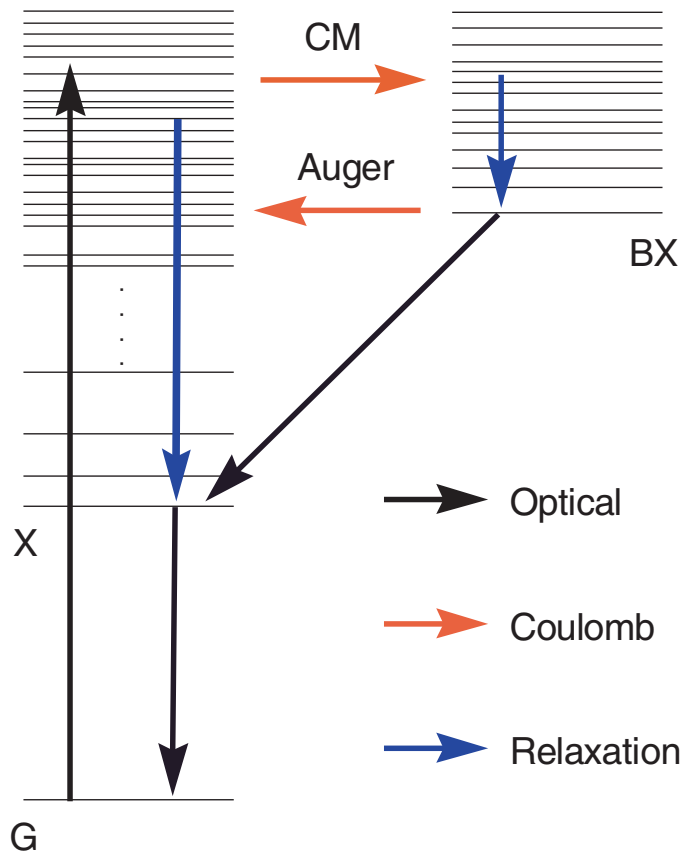
Figure 1-8: Diagram showing ground, exciton, and biexciton states and the physical processes relevant to Carrier Multiplication. Upon UV photon absorption, a highly excited X state is created that can either decay by phonon relaxation or undergo CM via the Coulomb interaction to become a BX state. Any BX population generated will later relax to an X state either by radiative decay or Auger (Coulomb) non-radiative decay.

and PbSe NCs at room temperature have found fast cooling dynamics that do not appear consistent with a phonon bottleneck [35, 36, 37]. In addition, some aspects of the experimental data are intriguing, such as similar CM effects seen in PbSe and CdSe despite the very different state structures at threshold, and the observed linear dependence of CM yields on excess energy [30].

1.6 Thesis Overview

Our initial study of carrier multiplication in CdSe NCs using transient photoluminescence (tPL), described in Chapters 2 and 3, was motivated by a need to confirm the extraordinary results found by TA and to explore in detail the material dependence of the CM enhancement. While complementary to TA in some ways, tPL is a background-free measurement better suited to the low excitation fluences necessary in CM studies. It is also more selective than TA since it relates to the number of e-h pairs instead of single-particle state filling. Chapter 2 describes our characterization of the spectral and dynamical signatures of exciton and multiexciton populations in transient PL. We find an enhancement of the biexciton radiative rate and discuss its origin theoretically. Following this "calibration" step, in Chapter 3 we describe our assessment of CM yields in CdSe NCs. Contrary to the CM enhancement reported in the literature, we found that CM efficiency in CdSe and CdTe NCs is close to zero even for photon energies for which $\hbar\omega = 3.1E_g$.

In chapters 4 and 5 we present our subsequent work on CM assessment by tPL in PbSe and PbS NCs. These materials are of more interest for practical applications because their size-dependent bandgaps can be tuned from the mid- to the near- infrared. Chapter 4 describes the PL upconversion apparatus we constructed and our characterization of exciton and multiexciton tPL features. Chapter 5 describes our measurement of CM yields. We distinctly observe a signal consistent with CM for all of our PbS and PbSe NC samples, but the CM yields we estimate are significantly lower than those of previous reports.

Our experimental findings have suggested that there is little or no CM enhance-

ment in NCs. In Chapter 6 we put these results in a theoretical context. We discuss the various theoretical models and calculations that have been put forward in an attempt to explain the initial findings of strong CM. We consider NC CM from a bulk physics perspective and discuss some aspects of NC photophysics, particularly of highly excited states, that are poorly understood but ultimately determine the carrier multiplication efficiency.

Chapter 7 deals with one of the practically useful consequences of the otherwise undesirable Auger recombination. The efficient suppression of multiphoton emission made possible by the Auger process is what allows colloidal NCs to be operated as triggered single photon sources [38, 6]. We show in Chapter 7 that the photon emission statistics of a single NC, as captured in the second order correlation function, $g^{(2)}(\tau)$, directly encodes information about the efficiency of the Auger non-radiative decay. We use this to determine biexciton emission quantum yields from single NCs. We found significant dot-to-dot inhomogeneity of the biexciton quantum yields within a sample, which we attribute to a variation in the biexciton Auger decay rates that has to date been obscured by ensemble averaging.

In Chapter 8 we test the charging theory of blinking by measuring blinking time traces of NCs which are known to have comparatively slower Auger multiexciton decay rates. In addition, we demonstrate that multiexciton emission also blinks on and off. We show how these findings are inconsistent with the standard charging model and propose directions for alternatives.

Chapter 9 concludes this work by offering some perspectives and suggesting avenues for future research. Appendix A contains derivations of the relationship between the radiative rates of various excitonic species relevant to the work presented. In Appendix B we present a mathematical development of the connection between measured $g^{(2)}(\tau)$ and the underlying NC photophysics.

Chapter 2

Photophysics of CdSe-based nanocrystals

To determine carrier multiplication yields by transient PL it is first necessary to establish a relationship between exciton populations and features in transient PL traces. This chapter describes the observed dynamics of X and BX photoluminescence and the rate equation model used to interpret the PL data. The most important novel result presented here is our experimental finding that the BX radiative rate is larger than that of the X by a factor of ~ 4.

2.1   Single Exciton dynamics

The lowest exciton in CdSe-based nanocrystal samples emits in the visible at wavelengths depending on their size. The breadth of the ensemble emission of highly monodisperse samples is ≈ 25nm, or about ≈ 100 meV. The dynamics of this decay has contributions from radiative and non-radiative processes. The radiative decay lifetimes of traditional type-I CdSe-based nanocrystals at room temperature is of approximately 20-30 ns [39, 40]. The strength of the nonradiative pathways is sample dependent and works to reduce the luminescence quantum yield. PL decays for all but the highest quality CdSe NC samples are multiexponential with notable subnanosecond features which are typically attributed to subpopulations with fast
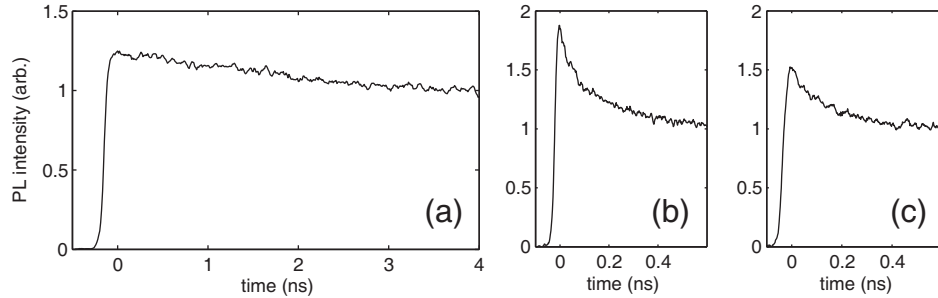
Figure 2-1: (a) Band edge luminescence decay of high quality overcoated CdSe/CdZnS NCs (QDOT655 from QDot Corp.) dispersed in hexane. (b) PL decay of a hexane dispersion of CdSe core NCs (first absorption feature at 1.99 eV), showing a pronounced fast component, attributed to a subpopulation with fast nonradiative decay. (c) Sample from NCs of the same batch, but treated with octylamine. The fast component is reduced and the luminescence quantum yield is higher than in the untreated sample. However, when a purification step was carried out to remove excess amines, the NC quality became worse than in (b). Untreated samples as in (b) were used in all subsequent CdSe NC experiments.

nonradiative processes. These X PL decays can be adequately described by a biexponential $f(t) = \exp\left(-t/\tau_{Xslow}\right) + c_{fast} \exp\left(-t/\tau_{Xfast}\right)$ for the purposes of data reduction. Previous work in our group has shown that at least some of the lifetime inhomogeneity may be dynamic [40].

Because a homogeneous population with a monoexponential decay would have facilitated subsequent analysis, especially of the exciton and biexciton radiative rates, we attempted to reduce the size of the fast component in the PL decays by chemical surface passivation of the NC samples with various compounds [41]. Octylamine treatment of the NCs gave the best results, shown in Fig. 2-1. However, sample quality tended to become even worse than the original untreated samples if any attempt was made to purify the NCs to remove excess unbound amine. Because the excess amines otherwise absorb strongly at the deep UV excitation wavelengths of interest for CM, we did not pursue this strategy further. All CdSe-based NC samples were used without surface treatment.

2.2   Multiexciton spectra

With increasing excitation fluence, spectra of the photoluminescence at early times show BX emission at the band edge and a further, blue-shifted feature corresponding to 1P-1P emission from higher multiexcitons (see Fig. 2-2). The BX state then decays quickly with a size-dependent lifetime $\tau_{BX} \approx$ 0.1-1 ns due to the fast nonradiative "Auger" process. As shown in Fig. 2-2b, the measured tPL decays are well described by a superposition of X dynamics and an additional single exponential BX component, $a_{BX} \exp\left(-t/\tau_{BX}\right) + a_X f(t)$. At very high excitation fluence we also observe an additional faster component at the band edge. Its dynamics appear consistent with $1S$-$1S$ emission from higher multiexcitonic states. The impact of these features on further analysis was minimized by omitting early time $(t \sim \frac{1}{2}\tau_{BX})$ data from fitting.

The biexciton lifetimes of various core and core/shell NC samples extracted from tPL data are shown in Fig. 2-2c. When plotted against the energy of the first absorption feature, both types of samples appear to fall on a universal curve. The first absorption feature is used for comparison instead of the NC size because it is a better indicator of the spatial extent and volume of the electronic wavefunctions for core/shell particles.

2.2.1   Kinetic model for transient PL

We analyzed the experimentally observed PL dynamics with a first order kinetic model of multiexciton relaxation:

$$
\begin{aligned}
\frac{\mathrm{d}p_1(t)}{\mathrm{d}t} &= -k_1 p_1(t) + k_2 p_2(t) \\
\frac{\mathrm{d}p_2(t)}{\mathrm{d}t} &= -k_2 p_2(t) + k_3 p_3(t) \\
&\vdots \\
\frac{\mathrm{d}p_j(t)}{\mathrm{d}t} &= -k_j p_j(t) + k_{j+1} p_{j+1}(t)
\end{aligned}
\tag{2.1}
$$

where $p_j(t)$ are the relative populations of NCs in the j-th multiexcitonic state (i.e. j electrons and holes), and k_j are the state decay rates. The transient photolu-
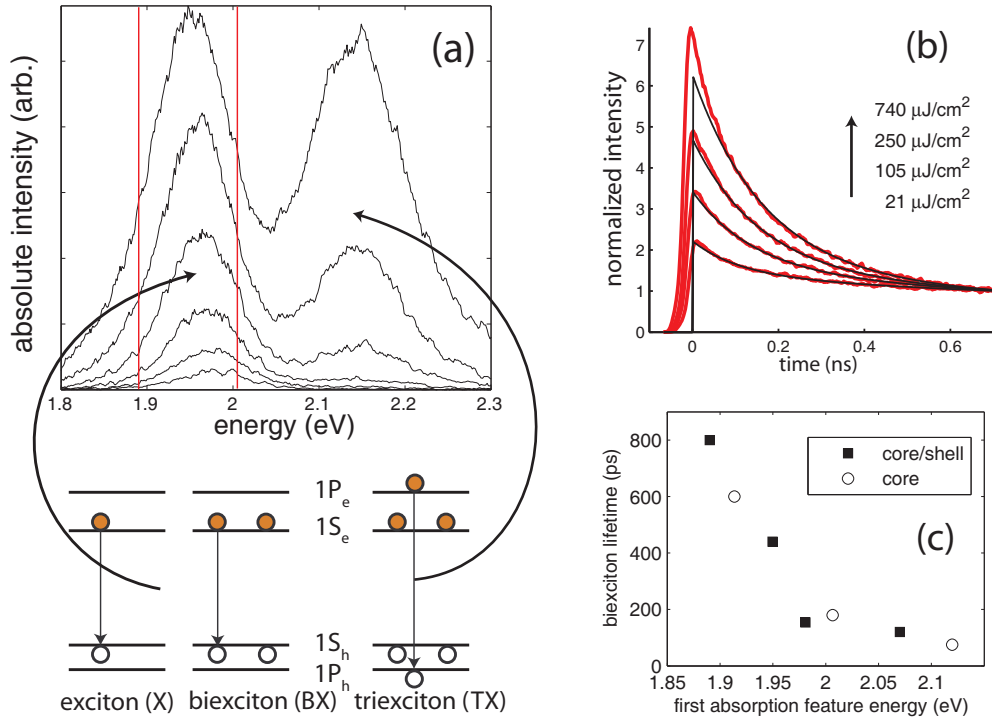
Figure 2-2: (a) Transient PL spectra integrated from $t = -10$ ps to $t = 10$ ps of CdSe core NCs with a first absorption feature at 2.0 eV under 3.1 eV excitation with increasing peak fluences of 20, 40, 80, 170, 340 and 740 μJ/cm^2. (b) Normalized PL decays integrated from 1.89 to 2.02 eV (red lines in (a)) showing the growth of a fast component due to biexciton decay. The black lines are fits to the form $a_{BX}e^{-t/\tau_{BX}} + a_X f(t)$ where $\tau_{BX} = 185$ ps and $f(t)$, the single X dynamics, are kept constant. (c) Biexciton lifetimes extracted from tPL decays of several CdSe samples plotted against the position E_{x0} of the lowest energy peak in each sample's absorption spectrum.
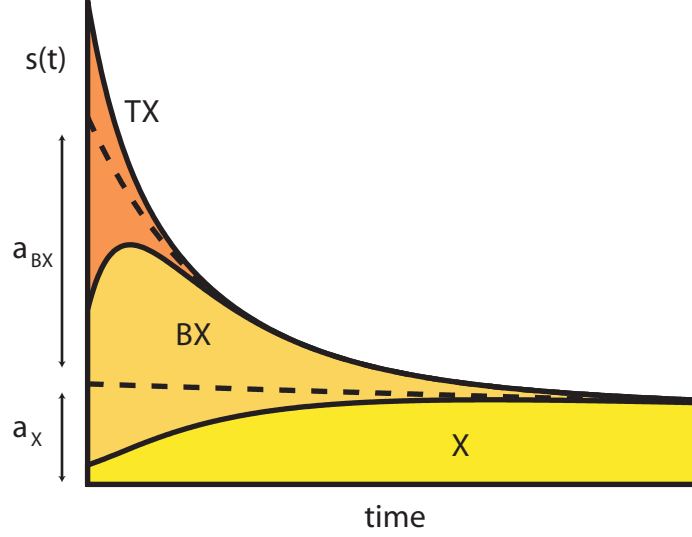
Figure 2-3: Decomposition of a tPL decay according to multiexcitonic state of origin. Solid areas show emission by X, BX, and TX states. The dashed lines show the decomposition of $s(t)$ into a sum of exponentials, $s(t) = a_X e^{-k_X t} + a_{BX} e^{-k_{BX} t} + a_{TX} e^{-k_{TX} t}$.

minescence (tPL) signal will have contributions from all populated states. We are particularly interested in the dynamics of emission from the $1S_e - 1S_h$ transition (i.e. band-edge luminescence), which we denote by $s(t)$ and is given by:

$$s(t) \propto k_1^{rad} p_1(t) + k_2^{rad} p_2(t) + \ldots = \sum_j k_j^{rad} p_j(t) \qquad (2.2)$$

where k_j^{rad} is the radiative rate of the j-th multiexciton state from the $1S$-$1S$ transition. In the case of $j = 1$ and $j = 2$, the k_j^{rad} values correspond to the total radiative decay rates of the X and BX, k_X^{rad} and k_{BX}^{rad}, respectively.

Fig. 2-3 illustrates the contributions to $s(t)$ in a typical case in which the excitation pulse creates a nonzero population in the X, BX and TX states at $t = 0$. The solid areas show the decomposition of the time-dependent PL, $s(t)$ according to the state the emission originates form. The dashed lines show the decomposition of $s(t)$ into a sum of exponentials, $s(t) = a_X e^{-k_1 t} + a_{BX} e^{-k_2 t} + (\ldots) e^{-k_3 t}$, as would be obtained from a multiexponential fit to measured tPL data.

Solving the rate equations using the fact that the single exciton lifetime is more than an order of magnitude longer than any of the multiexciton lifetimes gives the

following decomposition of $s(t)$:

$$a_X = k_1^{rad}(p_1^o + p_2^o + \ldots) = k_1^{rad}p_{j>0}^o \tag{2.3}$$

$$a_{BX} = (k_2^{rad} - k_1^{rad})p_{j>1}^o\left(1 + \frac{k_2}{k_3 - k_2}\frac{p_{j>2}^o}{p_{j>1}^o} + \ldots\right) \tag{2.4}$$

$$s(t) = a_X e^{-k_1 t} + a_{BX}e^{-k_2 t} + (\ldots)e^{-k_3 t}$$

where the $\{p_j^o\}$ denote initial populations at $t = 0$. The $e^{-k_1 t}$ component of $s(t)$ is proportional to the X radiative rate multiplied by the population of NCs that start in an X state or higher, since MX states eventually decay to the X state. The BX component has three factors. It is firstly proportional to the difference of X and BX radiative rates because BX luminescence is partially offset by a dip in X luminescence, as it is still in the process of being populated. The second factor in the expression for a_{BX} is proportional to the number of NCs initially in a BX or higher state. The third term captures the small delaying effect of cascaded decay from the TX. In NCs originally in the TX state, there is a short $t \sim k_3^{-1}$ delay before the BX state is populated, which then decays normally at a rate k_2. Thus, if the $e^{-k_2 t}$ dependence of the subsequent BX decay is extrapolated back to $t = 0$ one expects to find a slightly larger value of a_{BX} than would be expected in the absence of the delay.

2.2.2 Determination of X and BX radiative rates

To determine the radiative rate of the biexciton from tPL decays it is necessary to estimate the populations $p_{j>0}^o$ and $p_{j>1}^o$ following pulsed excitation. The p_m^o are related to the incident laser power by Poissonian photon absorption statistics. We explicitly account for the inhomogeneous excitation profile of the beam, measured directly with a CCD camera, because our apparatus collects emission from a large volume in the sample. Then,

$$p_m^o = \int \frac{n(\vec{r})^m}{m!}e^{-n(\vec{r})}\mathrm{d}^3\vec{r} \qquad n(\vec{r}) = j_p(\vec{r})\sigma$$

where $j_p(\vec{r})$ is the measured photon flux at $\vec{r}$, $n(\vec{r})$ is the average number of absorbed photons per NC, and σ is the absorption cross-section at the excitation wavelength.
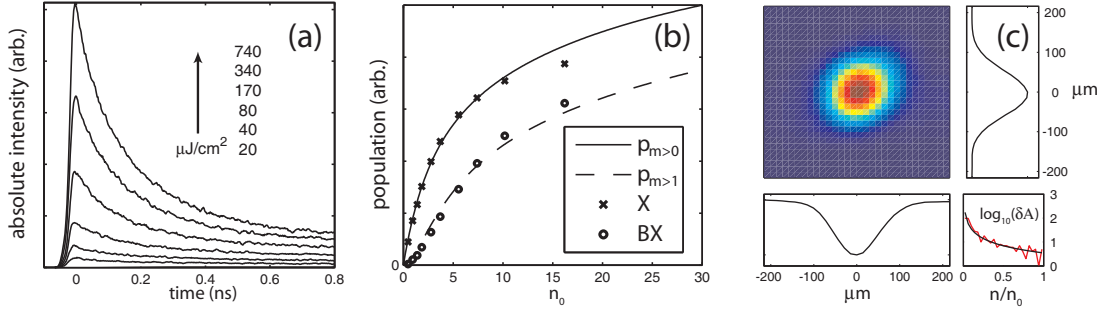
Figure 2-4: (a) Unnormalized PL decays of the same sample as in Fig. 2-2a showing the growth of both long-time exciton and short-time biexciton components in the decay as these levels are increasingly populated by higher excitation powers with peak fluences as noted. (b) (lines) Predicted initial NC populations in an X or higher state ($p_{m>0}$) or in a BX or higher state ($p_{m>1}$) plotted against the peak average number of e-h pairs created, $n_0 = \max\{n(\vec{r})\}$. ($\times$,$\circ$) a_X and a_{BX} PL components extracted from fits to measured decays, scaled horizontally and vertically to fit the population profiles. (c) (top left) Spatial profile of the excitation beam at the sample position measured directly on a CCD camera. (top right and bottom left) Cross sections showing a nearly Gaussian shape. (bottom right) Red: Logarithm of the histogram of the relative area on the sample experiencing a normalized excitation intensity n/n_0. Black: fit to the histogram expected for a perfectly Gaussian beam

We treated σ as an adjustable parameter because it is difficult to measure with sufficient accuracy, especially for core/shell particles, requiring assumptions or detailed measurements of particle shape and composition. For all our particles the σ values that gave the best fit were within an order of magnitude of literature cross sections for comparable CdSe cores [42].

Fig. 2-4b shows that the growth and saturation of the X and BX dynamical features in measured tPL decays is adequately described by the population model we used. From the ratio of the scaling factors between a_{BX}, a_X and $p_{m>1}$, $p_{m>0}$ we obtain the a_{BX}/a_X ratio expected at BX saturation ($p^o_{m=2} = p^o_{m>0}$). The sample-dependent $(a_{BX}/a_X)_{sat}$ value usually lies in the range from 3 to 4.5 but for one sample it was as large as 6. This implies a substantially faster radiative rate of the BX relative to the X and leads to enhanced sensitivity of tPL for detection of small multiexciton populations, as is illustrated by the prominence of BX features in Fig. 2-2.

The population model we have used assumes a homogeneous sample of NCs with identical decay rates $\{k_j\}$, but, as described previously, experimental tPL data show

multicomponent X PL decays. Quantitative determination of the ratio of the BX to X radiative rates is complicated by uncertainty in how to interpret the inhomogeneous population underlying this multiexponential X PL decay. We have shown that [43]:

$$\frac{k_{BX}^{rad}}{k_X^{rad}} = 1 + \left(\frac{1 + c_{fast}}{1 + b}\right)\left(\frac{a_{BX}}{a_X}\right)_{sat} \tag{2.5}$$

Where c_{fast} is as described in Section 2.1 and b is a factor that accounts for a hypothetical subpopulation of NCs that do not show significant BX emission. The latter is unobservable but would be predicted to range from 0 to $\sim c_{fast}$ [43]. Using $b \approx c_{fast}$, we have $k_{BX}^{rad}/k_X^{rad} \approx 1 + (a_{BX}/a_X)_{sat}$, giving an estimated range $k_{BX}^{rad}/k_X^{rad} \approx$ 4-6.

2.2.3   Interpretation of enhanced BX radiative rate

The fast BX radiative rate is a consequence of spin selection rules applied to confined carriers. To put the value of $k_{BX}^{rad}/k_X^{rad} \approx$ 4-6 in perspective we note that for two independent excitons in the bulk one would expect $k_{2X}^{rad}/k_X^{rad} = 2$. In NCs, however, both electrons are spatially overlapped with both of the holes. A quantitative understanding of the BX radiative enhancement requires a discussion of the non-trivial electronic fine structure of X and BX states.

In Zinc-Blende CdSe, the conduction band has a two-fold $S = 1/2$ spin degeneracy and the valence band has a four-fold $J = 3/2$ degeneracy, resulting in nominally 8- and 6-fold degenerate X and BX states. The degeneracy is broken for real nanocrystals which tend to have a wurtzite crystal structure, adopt various approximately ellipsoidal shapes and in which the electrons and holes interact via spin-dependent Coulomb exchange [44]. The calculated splitting between lowest and highest fine structure states for the particle size range used in our study is < 30 meV, which is comparable to $kT \approx 25$ meV at room temperature. For the limit in which all levels are equally populated, it is shown in Appendix A.1 that $k_{BX}^{rad} = 4k_X^{rad}$. Essentially, the fact that there are two electrons gives a factor of two, while the fact that there are two holes makes it twice as likely that each electron can find a suitable hole to

satisfy dipole selection rules for radiative recombination. In the opposite limit where kT is much smaller than the fine structure splitting one would also expect BX radiative enhancement. Emission from the X fine structure ground state is spin-forbidden, so X luminescence is relatively slow and consists mostly of emission from thermally populated spin-allowed bright states [45, 44, 46]. However, transitions from the BX fine structure ground state to some states in the X fine structure are predicted to be optically allowed [46], indicating that k_{BX}^{rad} will be significantly larger than k_X^{rad} in this limit too.

Chapter 3

Carrier Multiplication assessment in CdSe NCs

In this chapter we describe our assessment of Carrier Multiplication (CM) yields in CdSe NCs. We measure PL decays of CdSe NC samples under weak intensity deep UV excitation and look for the features associated with biexciton population that should be present if CM occurs. Contrary to prior studies reporting highly efficient CM in CdSe, we find no observable multiplication. Reasons for the discrepancy are discussed.

3.1   Experiment Design

The CM measurement apparatus and methodology were designed to meet several criteria, with special attention paid to minimizing the possibility for false positive CM signals without compromising sensitivity. Previous reports on CdSe NCs [30] had indicated a $2.5E_{X0}$ threshold for CM, requiring excitation energies above 5 eV. From the various possibilities, we chose to create tunable pulsed excitation at these high energies by nonlinear mixing of pulses from a visible optical parametric amplifier (OPA).

3.1.1 Sample Preparation

Semiconductor nanocrystals (NCs) were synthesized by high temperature pyrolysis of precursors [47, 40]. The product was purified by precipitation once with butanol and methanol and redispersed in hexane, which is both a good solvent for NCs and quite transparent in the UV [48]. This was the minimum processing necessary to remove compounds present in the growth solution that otherwise absorb strongly in the deep UV. Samples were diluted to an appropriate concentration and introduced in quartz cuvettes of 1mm path length. For excitation-fluence studies, dilute solutions with an optical density (OD) of $\approx$ 0.1 at 3.1 eV were used. This facilitates observation of X and BX population saturation in power series (as in Fig. 2-4). Otherwise, the excitation beam would be inhomogeneous not only radially but axially as well, slowing down saturation even further (Eqn. 2.5).

For measurements under UV, however, we employed very concentrated samples (OD $\approx$ 1 at 3.1eV) to minimize the effects of degradation. Because the OD at the $\hbar\omega > 5.6$ eV energies used is at least $\approx$ 5, only a small volume in the sample is being excited. A small magnetic bar was added to the solution. It was positioned near the excitation point and rotated vigorously in a plane parallel to the cuvette surface using an external magnetic stir plate. This, combined with the small excitation volume simulates a continuous flow experiment, thereby minimizing the number of UV photons absorbed per NC while achieving the desired PL signal intensity. Experiments were carried out in front-face geometry, so reabsorption effects are very small despite the high concentrations because the ratio of the deep UV and band edge absorption cross section is very large. Precaution was taken to avoid sample degradation because it can lead to signals that appear misleadingly like those one might expect to see from CM. All measurements and manipulations were carried out at room temperature.

3.1.2 tPL Apparatus and measurement methodology

The experimental setup used for studying CM by tPL with 5.6 eV excitation is shown in Fig.3-1. Tunable UV excitation pulses were generated by type-1 nonlinear mixing of
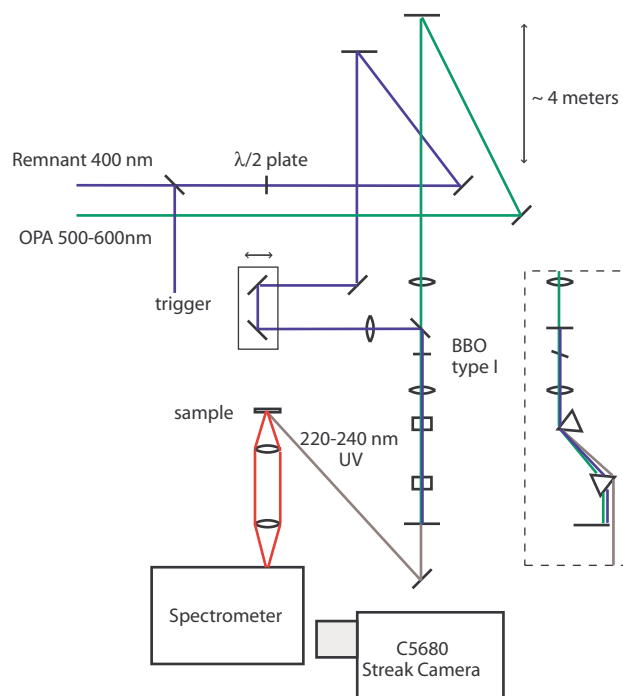
Figure 3-1: Apparatus used for studying tPL of visible-emitting NCs. Excitation energies up to 5.6eV are obtained by sum frequency generation. For 5.9 eV excitation a 3.0eV beam was directly doubled. Not shown: beam path for excitation of the sample with 3.1eV and magnetic stirring plate behind the sample.

the visible output and 3.1 eV remnant of an optical parametric amplifier (Coherent OPA 9400) pumped by a 250 kHz amplified Ti:sapph laser (Coherent RegA 9000) in a 1 mm thick beta-barium borate (BBO) crystal. BBO was chosen because of its transparency in the deep UV. We isolated the 5.6 eV sum frequency generated beam from the 2.5 eV and 3.1 eV fundamental beams using a prism pair. This was confirmed by checking that UV-excited tPL signals vanish if the relative delay of the fundamental beams is adjusted or if a UV absorber (such as a thin glass coverslip) is placed in the beam path. For excitation at 3.1 eV, the OPA was blocked and the 3.1 eV beam was directed onto the same excitation spot on the sample. For excitation at 5.9 eV, the Ti:sapph was tuned to the red and its second harmonic was directly doubled in the same nonlinear crystal. The resulting second harmonic generation beam was weak but sufficiently strong for tPL collection.

The excitation beams were characterized spectrally with a fiber spectrometer (Ocean Optics QE65000) and their spatial profiles were obtained by directly imaging them onto a CCD camera (Roper Scientific MicroMax) placed at the sample position.

CM determination measurements consisted of alternating acquisitions under weak 3.1 eV and UV excitation. Exposure to UV was minimized by using low excitation power (≤ 50 μW) and short integration times (~ 5 min). Under these conditions, tPL decays resulting from weak 3.1 eV excitation remained unchanged throughout the length of the experiment, confirming that sample integrity was not compromised.

3.2 Results

Fig.3-2 shows PL decays of a representative sample of E_g=2.0 eV CdSe NCs under weak and strong excitation at 3.1 eV and 5.6 eV (E_g determined from the lowest absorption feature). At high fluence both decays show an additional fast component consistent with biexciton (BX) emission. Remarkably, and unlike data from Ref. [49] which shows a fast component under UV excitation, we find that the two low-fluence decays follow each other closely.

For all samples we studied, whether of core or core-shell structures, it was seen
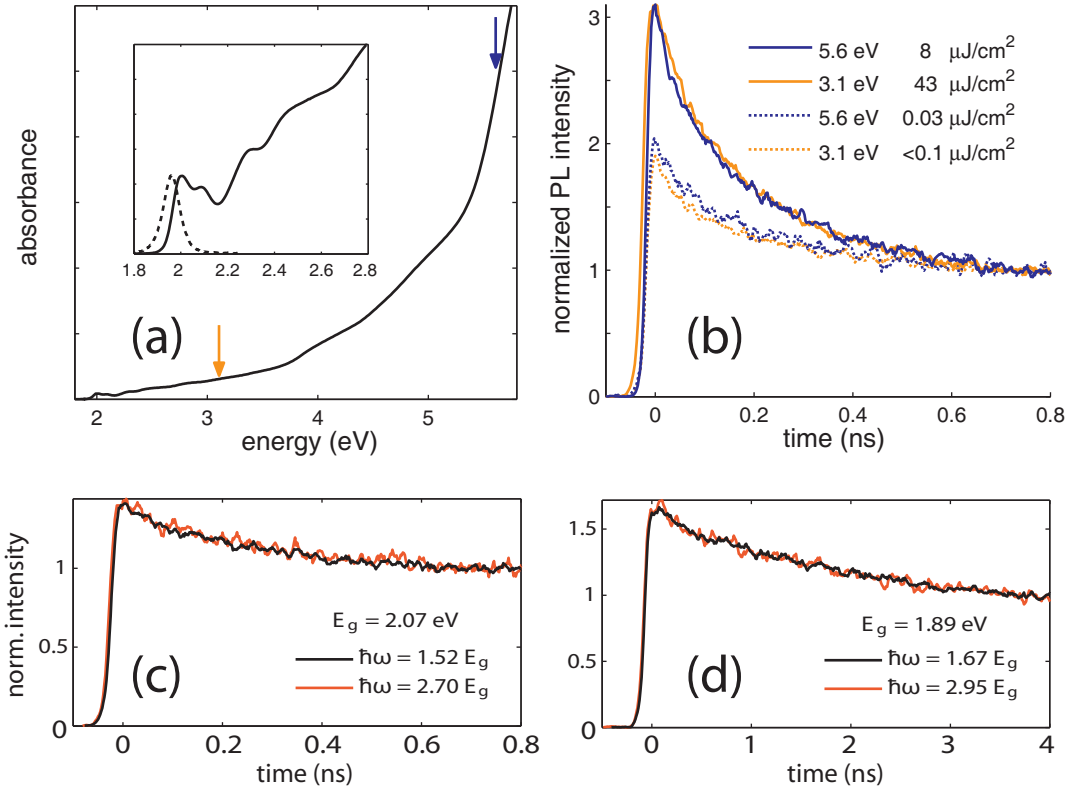
Figure 3-2: (a) Absorption spectrum of a typical CdSe NC core sample used. Excitation energies employed in tPL are indicated by the arrows. (inset) Detail of band edge absorption and emission spectra. (b) Band edge luminescence dynamics of the sample at 3.1 eV and 5.6 eV using peak pulse fluences as noted. The energy of the 5.6 eV excitation is 2.8 times larger than the sample's first exciton energy E_{X0}, well over the energy conservation threshold for CM. (c) & (d) Band edge PL decays of E_g=2.07 eV and E_g=1.89 eV core/shell CdSe NCs under weak ($n_0 < 0.01$) excitation at 3.1eV (black) and 5.6 eV (red). The 5.6 eV excitation corresponds to $\hbar\omega$=2.70E_g and 2.95E_g respectively. Similar results were observed for 5.9 eV excitation.

that while signatures of multiexciton emission appear at high fluence, decays under weak 5.6 or 5.9 eV excitation are close to indistinguishable from decays under weak 3.1 eV excitation (Fig. 3-2) even for large NCs where the excitation energy $\hbar\omega$ exceeds $3E_g$. We have shown in section 2.2.2 that even small BX populations will appear prominently in transient PL. Our data therefore shows that CM is very inefficient in CdSe NCs.

3.2.1 Quantitative Analysis

Although visual inspection of the decays is sufficient to conclude that no significant CM is occurring in these samples at the wavelengths used, we describe here how a quantitative estimate can be obtained because it will be necessary for our later study of CM in lead chalcogenide NCs.

We define the carrier multiplication yield y_{cm} as the number of additional electron-hole pairs generated immediately after absorption of a single excitation photon. For example, if a single photon generated a biexciton state with unity efficiency, we would have $y_{cm} = 1$. The CM yield can be obtained from transient PL studies of an ensemble under very weak excitation so that only one photon at most is absorbed by any single NC:

$$ y_{cm} = \lim_{\langle N \rangle \to 0} \frac{\sum_{m>1}(m-1)p_m^o}{\sum_{m>0}p_m^o} $$

In the numerator the various multiexciton populations are weighed by the number of excess e-h pairs they carry. The denominator normalizes the excess carrier yield by the total population of NCs that absorbed a photon. For the purposes of interpretation of our experiments only the BX contribution needs to be included. Using the results of the population modeling in Chapter 2 we can directly relate y_{cm} to the sizes of the BX and X dynamical components in a fit to the UV-excited data:

$$ y_{cm} = \frac{p_2^o}{p_1^o + p_2^o} = \frac{a_{BX}}{a_X} \left/ \left(\frac{a_{BX}}{a_X} \right)_{sat} \right. \tag{3.1} $$
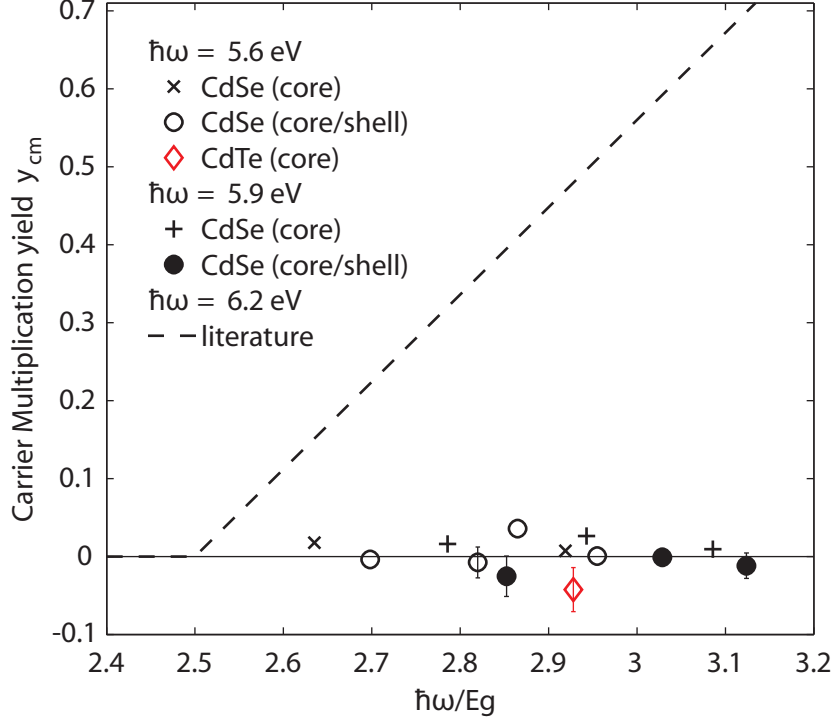
Figure 3-3: Carrier multiplication yields under 5.6 and 5.9 eV excitation extracted from tPL decays using the relationship $y_{cm} = \frac{a_{BX}/a_X}{(a_{BX}/a_X)_{sat}}$. Conservative (small) values $(a_{BX}/a_X)_{sat}$ were used for each sample. 2σ-wide error bars from repeated measurements are shown if larger than the symbols. The dashed line is the y_{cm} vs. $\hbar\omega/E_g$ dependence found in the TA studies of Ref. [30] using $\hbar\omega = 6.2$eV.

Where a_{BX} and a_X are obtained from a fit to the form $a_{BX}\exp\left(-t/\tau_{BX}\right) + a_X f(t)$ and the saturation ratio $(a_{BX}/a_X)_{sat}$ is independently estimated using 3.1 eV excitation as discussed in Section 2.2.2. Fig. 3-3 shows quantitative estimates of the CM yields in the samples we studied. No statistically significant CM was observed, despite the high sensitivity of transient PL experiments to multiexcitons.

3.2.2   Comparison to Literature data

As seen in Fig.3-3, our results do not match the $\hbar\omega/E_g$ dependence of y_{cm} found in TA measurements on CdSe NCs using 6.2 eV excitation [30]. In principle this could be because y_{cm} is not only a function of the ratio $\hbar\omega/E_g$, as suggested by TA on PbSe NCs [26], but also depends explicitly on $\hbar\omega$. However, it is difficult to imagine 5.9 eV and 6.2 eV excitation having such drastically different effects. The large CM

47

yields reported in the literature could probably be attributed to artifacts from sample deterioration under deep UV excitation.

3.2.3 A note on UV sample degradation

We realized the severity of the UV degradation problem when we attempted to carry out excitation power series at 5.6 eV on very dilute samples such that the OD at that energy was low. During the course of the experiment we found that the PL dynamics quickly and irreversibly steepened, until the X decay itself was nearly as fast as MX decays would normally be.

Fig. 3-4 illustrates the strong effect of UV exposure even on a fairly concentrated (OD$\approx$ 0.1 at 3.1 eV) stirred sample. Exposure at the level of milliwatts over a few minutes irreversibly changes the sample's X decay dynamics probed with lower energy 3.1 eV excitation. The additional fast components that appear have timescales that are similar, though distinguishable, from those of BX states generated by multiphoton excitation at higher fluences. Importantly, similar exposure to 3.1 eV excitation does not lead to such rapid degradation. There are several conceivable mechanisms for deep-UV specific degradation. It is possible that ligands on the NC absorb slightly in the deep-UV and could then oxidize or detach themselves from the NC surface, leaving a trap for subsequent carrier capture. Alternatively, the highly excited electron or hole obtained directly after absorption could initiate redox chemistry on the ligands or surface, thereby creating new electronic defects for X recombination.

The observed wavelength-dependent degradation by light exposure could be mistaken for CM, which is similarly expected to become stronger at higher excitation energies. To prevent incorrect assignment, experiments should be carried out under low exposure levels and the dynamics of the PL traces should be carefully analyzed to ensure that any CM-like signal originates from MX states and not from enhanced X trapping.
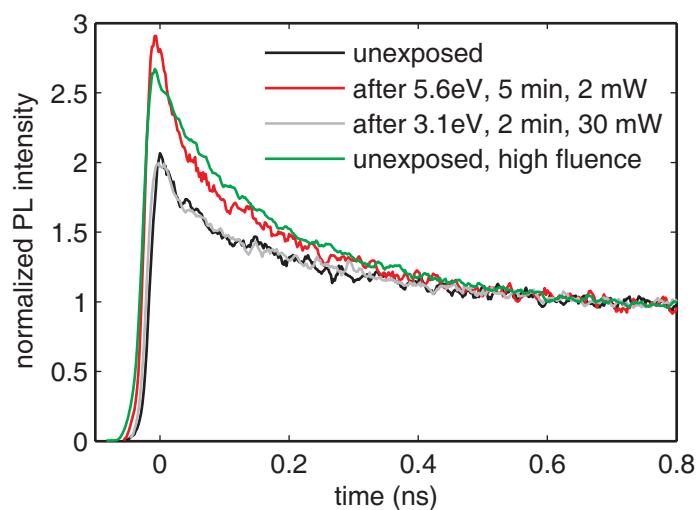
Figure 3-4: Decays of a stirred CdSe core NC sample (same sample as in Fig. 3-2a & b) illustrating the effect of UV degradation. Black and Red: Exciton PL decays under low fluence 3.1 eV excitation before and after a 5 minute exposure to 5.6 eV at an intensity of 2 mW. Grey: X PL decay of a different aliquot after exposure to 30 mW 3.1 eV for 2 minutes. No degradation is observed even after longer exposures. Green: For comparison, a PL decay of a separate aliquot under 3.1 eV excitation of high enough fluence that appreciable BX population is generated.

Chapter 4

Photophysics of PbSe and PbS NCs

In this chapter we present the basic photophysics of exciton and multiexcitonic states in PbS and PbSe NCs. First the fluorescence upconversion apparatus used to take transient PL data in the NIR is described. The X dynamics and the effect of chemical treatments to improve the NC electronic quality are discussed. BX lifetimes and radiative rates were measured and are interpreted theoretically. Preliminary results on the spectroscopy of MX and X photoluminescence are also presented.

4.1   Experimental Apparatus for transient PL in the NIR

The emission maxima of PbS and PbSe NC samples used in this study range from 0.5 eV to 1 eV. Study of MX transient PL in these samples requires fast picosecond time resolution to capture the fast Auger decay, and CM assessment additionally requires high sensitivity so that low excitation fluences can be used. No fast sensitive detectors analogous to streak camera, time-correlated single photon counting or MCP-gated systems are available to cover the desired IR PL range of the lead chalcogenide samples. We therefore chose to construct an apparatus using an optical gating scheme
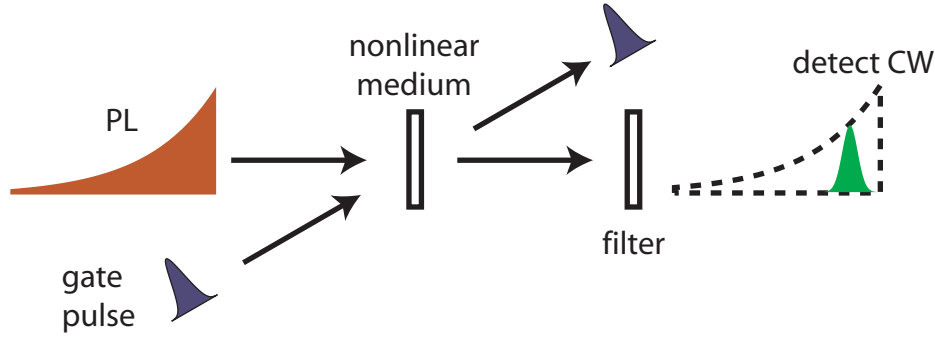
Figure 4-1: General scheme for measuring transient PL signals by nonlinear optical gating.

to obtain our time resolution [50, 51].

In an optically gated tPL experiment, fluorescence produced from pulsed excitation of a sample is focused on a nonlinear crystal along with a second "gate" laser pulse as shown in Fig. 4-1. The ultrafast gate and the fluorescence light present at that time in the crystal interact via the crystal's nonlinearity to produce a third light field that is then separated and detected. By changing the arrival time of the gate pulse at the crystal, different time-slices of the fluorescence are singled out for nonlinear interaction, changing easily measurable properties of the third field like intensity or wavelength. Because the time resolution is obtained from the gate pulse and not the detector, the detector can be optimized for sensitivity without worry about its speed.

In our apparatus, the 1.55 eV gate and the fluorescence interact via sum-frequency generation [51], generating an "upconverted" 2-2.5 eV visible signal for which sensitive detectors are readily available. The main potential alternative would have been a Kerr-gate setup exploiting the change of index of refraction during the gate pulse to slightly rotate the fluorescence. This was not chosen because an IR detector would still be necessary. In addition, we anticipated that typical polarization analyzers do not have large enough extinction ratios to fully isolate the gated signal from the rest of the long-lived exciton fluorescence in lead chalcogenide NCs [36].

A diagram of our ultrafast fluorescence upconversion apparatus based on a 250 kHz regeneratively amplified Ti:sapphire laser is shown in Fig. 4-2. A portion of the
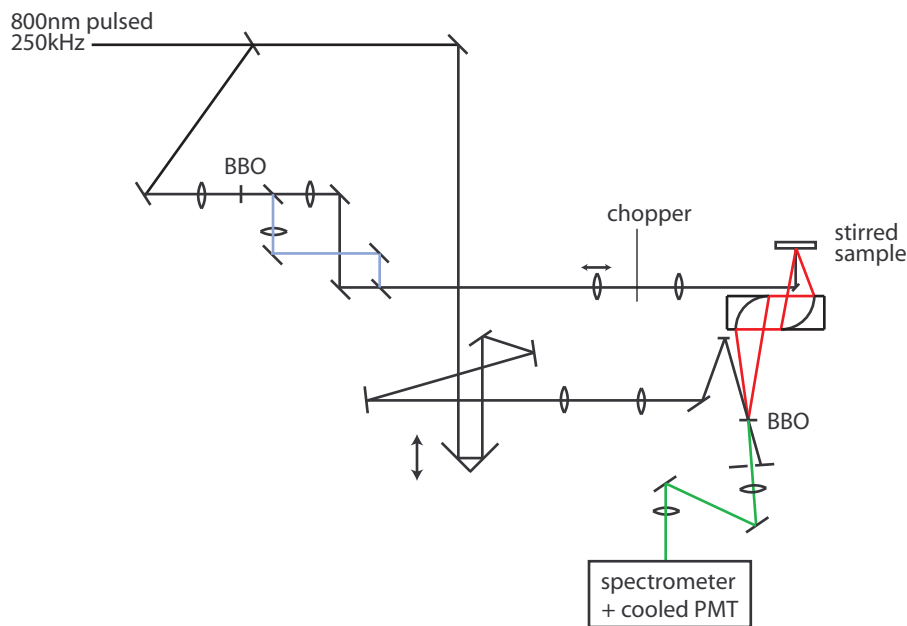
Figure 4-2: Fluorescence upconversion apparatus for measuring transient PL in the NIR with picosecond time resolution. A 1.55 eV beam and a 3.1 eV (blue line) beam can be chosen as the excitation source.

pulse train was passed through a BBO crystal to generate excitation sources at 3.1 eV and 1.55 eV which were separated with two dichroic mirrors and focused on the sample to spot sizes of roughly ~ 100 μm and ~ 50 μm diameter respectively, as determined by measuring transmission through a pinhole. The arrangement allows for reproducible switching between the two excitation wavelengths. Emission was collected in a front-face geometry using off-axis parabolic mirrors and focused onto another BBO crystal. Parabolic mirrors were chosen because they can efficiently collect and collimate light from a single point and have no chromatic aberration, which was useful for system alignment and operation.

Following a variable delay, the rest of the 1.55 eV pulse train was overlapped with the collected emission and the resulting sum frequency generation was separated spatially and spectrally using interference filters and a monochromator. The signal was detected with a cooled photomultiplier tube (PMT) and amplified using a current amplifier (Keithley) followed by a lock-in amplifier. The PMT/lock-in approach was advantageous compared with using a CCD camera and background subtraction because some of our acquisitions were longer than the timescale of changes in the

background level due to laser drift. Since we were mostly interested in high resolution dynamics and not high resolution spectra, our monochromator exit slit could be set large enough to allow simultaneous collection of most of the spectral bandwidth of the signal even with a PMT.

For these experiments, the pulse width was maintained relatively long by tweaking the amplifier compressor away from its optimal short-pulse configuration to avoid excess noise from continuum generation in the BBO upconversion crystal. We have nevertheless maintained a time resolution better than 15 ps as measured from the rise time of the tPL signal.

4.2   Sample Preparation

PbSe and PbS NCs were prepared by high temperature pyrolysis of Pb and Se/S precursors in an oleic acid/octadecene mixture [12, 52]. The growth solutions were purified by a single precipitation, redispersed in hexane, and transferred to quartz cuvettes with 1mm path length in a nitrogen glovebox. The resulting samples, with optical densities of $\sim$ 1-3 at 1.55 eV (OD $\sim$ 10 at 3.1 eV), were sealed and taken out into air for subsequent measurements. As will be described below, some samples of larger particles (first absorption feature <0.8 eV) were treated with Cd^{2+} by adding a few drops of cadmium oleate to the hexane NC dispersions at room temperature [53, 41]. Since we carried out our CM studies at 3.1eV, there was little interference from oleate absorption and no further purification was necessary. All samples were magnetically stirred during data acquisitions, and PL decays under weak 1.55 eV excitation were periodically monitored to check for any degradation. A typical sample's absorption spectrum is shown in Fig. 4-3.

4.3   Exciton PL dynamics

The exciton decay dynamics of PbSe and PbS samples are notably different from those of CdSe-based NCs. In general, samples of small and moderate sized PbSe and
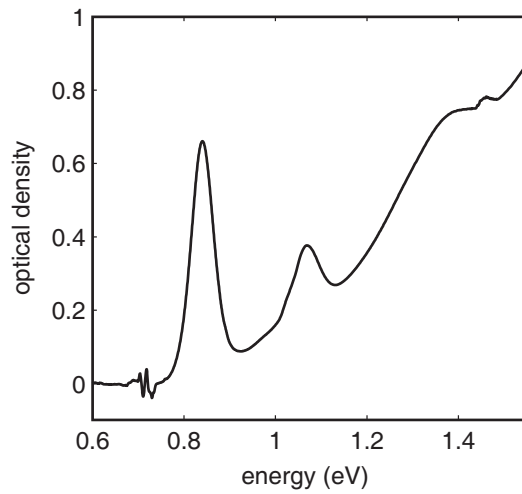
Figure 4-3: Absorption spectrum of a typical PbSe NC sample used in this study. The position of the ground exciton energy level, $E_{X0} = 0.84$ eV, is determined as the peak of the first absorption feature.
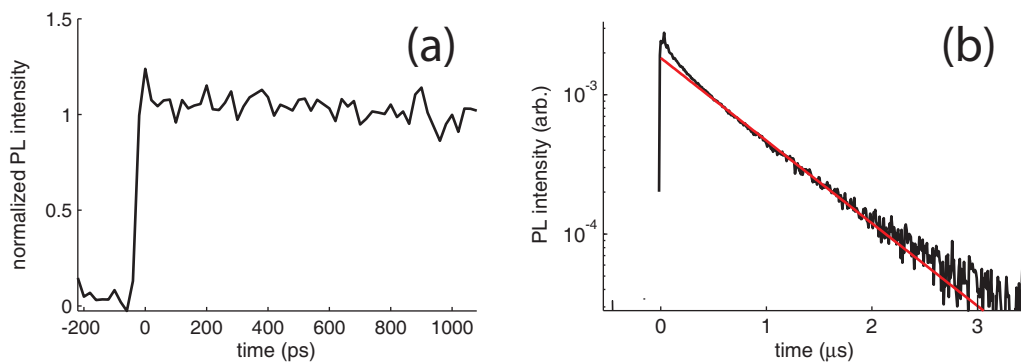
Figure 4-4: (a) Transient PL dynamics of a sample of PbSe NCs in hexane dispersion ($E_{X0} = 0.84$ eV) under weak 1.55 eV excitation. (b) PL decay of a hexane dispersion of PbS NCs (also with $E_{X0} = 0.84$ eV) on a longer timescale collected with a fast photodiode. The red line corresponds to an exponential decay with a $\tau \approx 660$ ns lifetime.
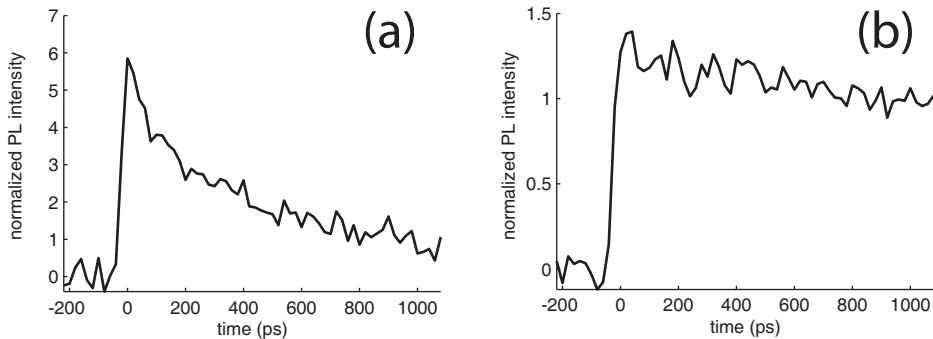
Figure 4-5: Transient PL dynamics under weak 1.55 eV excitation of PbS NCs ($E_{X0} = 0.73$ eV) in hexane dispersion. (a) Without additional chemical treatment. (b) Cadmium-oleate treated sample.

PbS NCs had flat PL dynamics over the full temporal range of our upconversion apparatus (see Fig. 4-4a). In contrast, as-prepared CdSe core particles almost invariably show significant sub-nanosecond dynamics as described in section 2.1 [43, 49]. The flat decays we observe in these PbSe and PbS samples suggest good surface passivation of NCs prepared by these methods and they are consistent with the very high luminescence quantum yields reported in the literature [36]. We measured the PL dynamics over a much longer window for one of our PbS samples using an InGaAs amplified photodiode and found a roughly single exponential fluorescence decay with a ~660 ns lifetime (Fig. 4-4b), consistent with previous studies [36].

The PL dynamics of larger as-prepared particles, those with $E_{X0} <\sim 0.8$eV, typically showed multiexponential X decays with large sub-nanosecond components, suggesting poor surface passivation. Moreover, these dynamics steepened irreversibly upon exposure to 3.1 eV radiation, in a similar way to the photodegradation of CdSe NCs in the deep UV described in section 3.2.3. We attempted to remove non-radiative pathways and to stabilize the particles by various chemical treatments and found that a mild Cd^{2+} treatment was the most successful [41, 53]. Remarkably, addition of cadmium oleate to hexane dispersions of $E_{X0} = 0.73$ eV PbS and $E_{X0} = 0.60$ eV PbSe NCs resulted in nearly flat single-exponential X decays (see Fig. 4-5) and robustness to prolonged 3.1 eV irradiation, while causing no noticeable changes in the absorption spectra and emission wavelength of the samples.

We have chosen to carry out further studies only on samples that show flat tPL decays over our experimental timescale, whether as-prepared or Cd^{2+}-treated, because the interpretation of subsequent results is considerably simplified. A multiexponential X decay entails an inhomogeneous distribution of NC surface passivation which can then support a nontrivial distribution of multiexciton lifetimes [43, 49], complicating both the isolation of MX features in tPL decays and the quantification of the underlying exciton and multiexciton populations. The second and more serious problem was that the X decays of samples with poor surface passivation tended to change irreversibly when exposed to 3.1 eV for the durations necessary to obtain adequately clean data with our apparatus. This was not the case for our CdSe CM study because the much higher sensitivity of the streak camera-based measurement apparatus allowed for exposure levels to be kept very low.

4.4   Multiexciton PL dynamics

An excitation power series for our $E_{X0} = 0.84$ eV PbSe sample is presented in Fig. 4-6a, showing the growth of a large fast feature, which we attribute to the BX, on top of the single X dynamics. These decays are well described as the sum of the slow X component described in the previous section and a fast BX component, $a_{BX}e^{-t/\tau_{BX}} + a_X e^{-t/\tau_X}$ with fixed lifetimes $\tau_X > 1$ ns and $\tau_{BX} \approx 60$ ps. Under strong excitation, additional faster components appear, attributable to emission from higher multiexcitons. As in our CdSe MX study in section 2.2, we delay fitting of the decays excited with 1.55 eV by a time $\sim \tau_{BX}/2$ to minimize unwanted interference from these higher MX tPL components in the determinations of a_X and a_{BX}.

A summary of our measured τ_{BX} is presented in Fig. 4-7. As expected, the Auger decay rate is strongly size-dependent. The BX decay rates we measure are consistent with those measured by pump-probe techniques. For example, we find $\tau_{BX} \approx 58$ ps and $\tau_{BX} \approx 140$ ps for $E_{X0} = 0.84$ eV and $E_{X0} = 0.68$ eV PbSe NCs respectively, while Beard et al.[29] have determined $\tau_{BX} = 67$ ps for $E_{X0} = 0.84$ eV and Schaller et al.[28] report $\tau_{BX} = 149$ ps for $E_{X0} = 0.64$ eV.
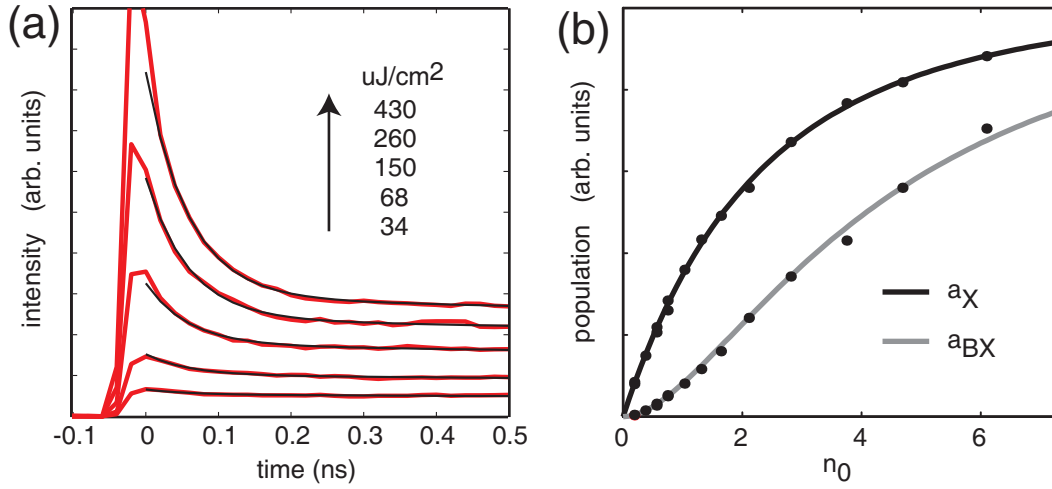
Figure 4-6: (a) Transient PL dynamics of PbSe NCs ($E_{X0} = 0.84$ eV) under increasingly strong 1.55 eV excitation, showing the growth of the BX emission feature. The thin solid black lines are fits to $a_X e^{-t/\tau_X} + a_{BX} e^{-t/\tau_{BX}}$ with $\tau_X > 1$ ns and $\tau_{BX} = 58$ ps fixed. (b) Fits of the X and BX exponential components a_X and a_{BX} to a population profile following Poissonian photon absorption statistics for an inhomogeneous excitation beam. n_0 denotes the maximum average number of photons absorbed
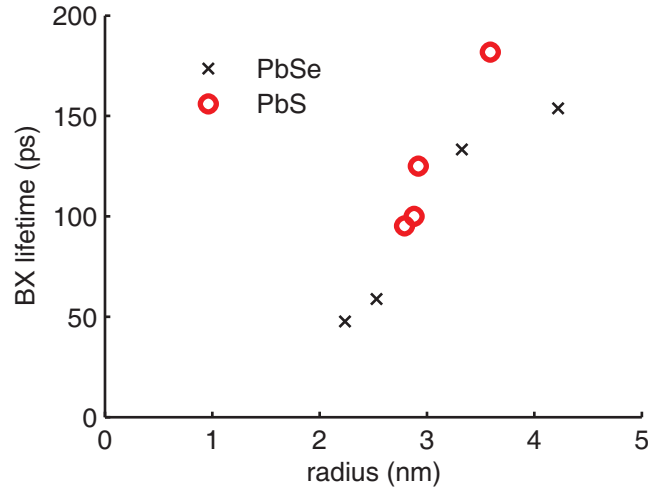
Figure 4-7: Biexciton lifetimes obtained from fits to tPL data from the PbS and PbSe NC samples used in this study. The radius of the PbS and PbSe particles in each sample was inferred from the first absorption feature, E_{X0}, using the E_{X0} vs r relationships reported by Cademartiri et al. [54] and Steckel [55] .

4.4.1 Estimation and interpretation of k_{rad}^{BX}

The population modeling and the analysis of the amplitudes of the dynamical components in tPL decays developed in section 2.2.1 applies for the lead chalcogenide NCs as well. In Fig. 4-6b, we fit the observed exponential components, a_X and a_{BX}, to population profiles assuming Poissonian photon absorption statistics. The fitting itself was done differently from the CdSe study and will be described below. The power series of X and BX features are found consistent with the Poissonian assumption, and we are able to estimate sample-dependent $(a_{BX}/a_X)_{sat}$ values in the range of 2.5-4. This implies that the radiative rate of the biexciton, k_{BX}^{rad}, is $\approx 3.5 - 5$ times greater than k_X^{rad}.

The $k_{BX}^{rad}/k_X^{rad} \approx 4$ values we estimate for the lead chalcogenide NCs are similar to those we observed for CdSe NCs (section 2.2.2). As is described in appendix A.2 a simple accounting of all the possible electronic configurations of band-edge X and BX assuming known selection rules and thermal equilibrium gives $k_{BX}^{rad} = 4k_X^{rad}$ as it also did for CdSe. This value is consistent with our results and suggests that both in CdSe and lead chalcogenides spin fine structure effects do not play an important role in determining the relative radiative rates of biexcitons and excitons at room temperature. As is shown in the appendix, it is more transparently seen in the lead chalcogenide case that the factor of 4 comes from a factor of 2 from having twice as many electrons times another factor of 2 because it is twice as likely for each electron to be matched with a suitable hole for radiative recombination.

4.4.2 Population modeling and fitting

As in the case of CdSe NCs, the exponential components in a tPL decay can be related to the MX and X populations soon after excitation through the following approximate expressions:

$$
\begin{aligned}
a_X &\propto k_X^{rad} p_{\geq 1} \\
a_{BX} &\propto \left(k_{BX}^{rad} - k_X^{rad} \right) p_{\geq 2}
\end{aligned}
$$

where $p_{\geq 1}$ and $p_{\geq 2}$ are the population of NCs that start with at least an exciton or a biexciton respectively at time 0. These populations are given by $p_{\geq m} = \sum_{k \geq m} I_k$, where the population of the k-th multiexciton state, I_k, is determined by Poisson statistics, taking into account excitation beam inhomogeneity and position dependent collection efficiency:

$$I_k = \int \phi(\vec{r}) \frac{n(\vec{r})^k}{k!} e^{-n(\vec{r})} \mathrm{d}^3 \vec{r}; \qquad n(\vec{r}) = \sigma j(\vec{r})$$

where $j(\vec{r})$ and $\phi(\vec{r})$ are the photon flux and collection efficiency at position $\vec{r}$, and σ is the absorption cross section. $n(\vec{r})$ is the average number of photons absorbed per pulse by a NC located at $\vec{r}$. If $j(\cdot)$, $\phi(\cdot)$ and σ were known, it would be possible to compute the I_k up to a common proportionality constant and obtain, by comparison with experiment, the saturation ratio $(a_{BX}/a_X)_{sat}$ (i.e. the value of a_{BX}/a_X when $p_{\geq 2} = p_{\geq 1}$). In the case of our CM study in section 2.2.2 the collection volume was large so $\phi(\cdot)$ was approximated as constant and $j(\cdot)$ was directly measured with a CCD camera, but σ was kept as an adjustable parameter. However, in the upconversion apparatus that we used for PbSe and PbS studies, both $j(\cdot)$ and especially $\phi(\cdot)$ are difficult to determine accurately. The latter, for instance, is determined by the details of the overlap of the focused fluorescence and gate pulse at the nonlinear crystal.

To carry out population modeling for the PbSe and PbS data without the benefit of accurate information on the excitation and collection profiles we adjusted our analysis method to take advantage of the fact that the shape of $p_{\geq 1}$ as a function of excitation power fully determines the shape of $p_{\geq 2}$. During any of our experimental excitation power series, $n(\cdot)$ only changes in magnitude while retaining its shape. Setting $n(\vec{r}) = n_0 h(\vec{r})$, where $h(\cdot)$ is a fixed shape and n_0 is a parameter, one can show that:

$$p_{\geq 2}(n_0) = p_{\geq 1}(n_0) - n_0 \frac{\partial p_{\geq 1}}{\partial n_0}$$

Critically, n_0 can be replaced with any quantity proportional to it, such as average excitation power, which is easily measured. Knowledge of the absorption cross section is also not required and no assumptions about the shape of the excitation beam profile

or the collection volume need to be made. In fact, if one finds any $h(\cdot)$ and $\phi(\cdot)$ so that the calculated $p_{\geq 1}(n_0)$ closely fits the shape of the observed a_X excitation series, then the $p_{\geq 2}(n_0)$ calculated with the same $h(\cdot)$ and $\phi(\cdot)$ will be proportional to a_{BX}.

More explicitly, we used a one-parameter $h(\cdot)$ family of the form $h(\vec{r}) = e^{-x^2-y^2-\alpha z}$ and a family of $\phi(\cdot)$ that cuts off contributions from $x^2 + y^2 > R^2$. Each discrete (α, R) combination was used in fitting the measured a_X vs excitation power by varying the proportionality constants between the power and n_0 and between a_X and $p_{\geq 1}$. Then the a_{BX} vs. power curve was fit by adjusting only the proportionality constant relating a_{BX} to $p_{\geq 2}$. The ratio of the a_{BX} and a_X proportionality constants is the desired estimate of $(a_{BX}/a_X)_{sat}$. For each sample, the value we report and use for CM assessment corresponds to the (α, R) combination that gave the best fit, in a least-squares sense, to the a_X population curve. We point out, however, that the $(a_{BX}/a_X)_{sat}$ estimates are remarkably insensitive to the choice of (α, R).

The results of this procedure, shown in Fig. 4-6b, demonstrate that the a_{BX} we observe match very well the trend we independently predict from the a_X evolution, further supporting our assignment of this fast component in the tPL to the biexciton. We find saturation values $(a_{BX}/a_X)_{sat}$ of 2.5-4 using this method. Since $(a_{BX}/a_X)_{sat} = k_{BX}^{rad}/k_X^{rad} - 1$, the corresponding values of k_{BX}^{rad}/k_X^{rad} are in the range 3.5-5 as discussed in the previous section.

4.5 MX Spectroscopy in PbS NCs

In this section we present preliminary results on the spectroscopy of Multiexcitons in PbS and PbSe NCs. Measurement of the relative spectral position of emission from multiexcitonic and excitonic states reveals information about binding energies and electronic correlation in these nanoscopic systems.

The results are preliminary because the PL upconversion apparatus was optimized for the study of dynamics and sensitive CM assessment, sacrificing ease in acquiring high resolution spectra. For the experiments described in this section the monochromator slits had to be narrowed and the wavelength scanned because we use a point

PMT detector. Signal levels were low despite high excitation intensities, and averaging times were long. In future, the apparatus may be modified to use a spectrograph and CCD camera for detection.

Figure 4-8 summarizes transient PL spectra of a PbS NC sample. The upconversion BBO crystal was rotated automatically as the spectrum was scanned to maintain Type-I phasematching across the entire spectral range shown. Unlike the CdSe case (Fig. 2-2) in which a blue-shifted tPL feature appears when higher MX are generated, the PL of PbSe MX states remains localized at the band-edge because the lead chalcogenides' four-fold degenerate valence and conduction band can accommodate up to 8 electrons and holes in the LUMO and HOMO. From this preliminary data we observe that spectra at early times are red shifted by about 10 meV compared to spectra at times much longer than the MX Auger decay lifetimes. This implies a biexciton binding energy $\Delta_{BX} = E_{BX0} - 2E_{X0} \approx 10$ meV. As shown in Fig. 4-8a, this early-time red shift saturates, remaining fairly constant as excitation fluence is increased and higher MX states are generated. Such behavior would result if the energy spacing between consecutive m and $m + 1$ multiexcitonic states ($m \geq 1$) is constant but smaller by a fixed binding energy Δ than the first exciton energy. Another salient feature of the data is changes in the shape and breadth of the spectrum at different powers and time delays. An exploration of these effects and a systematic determination of the emission energy of each multiexcitonic state may be carried out in future.
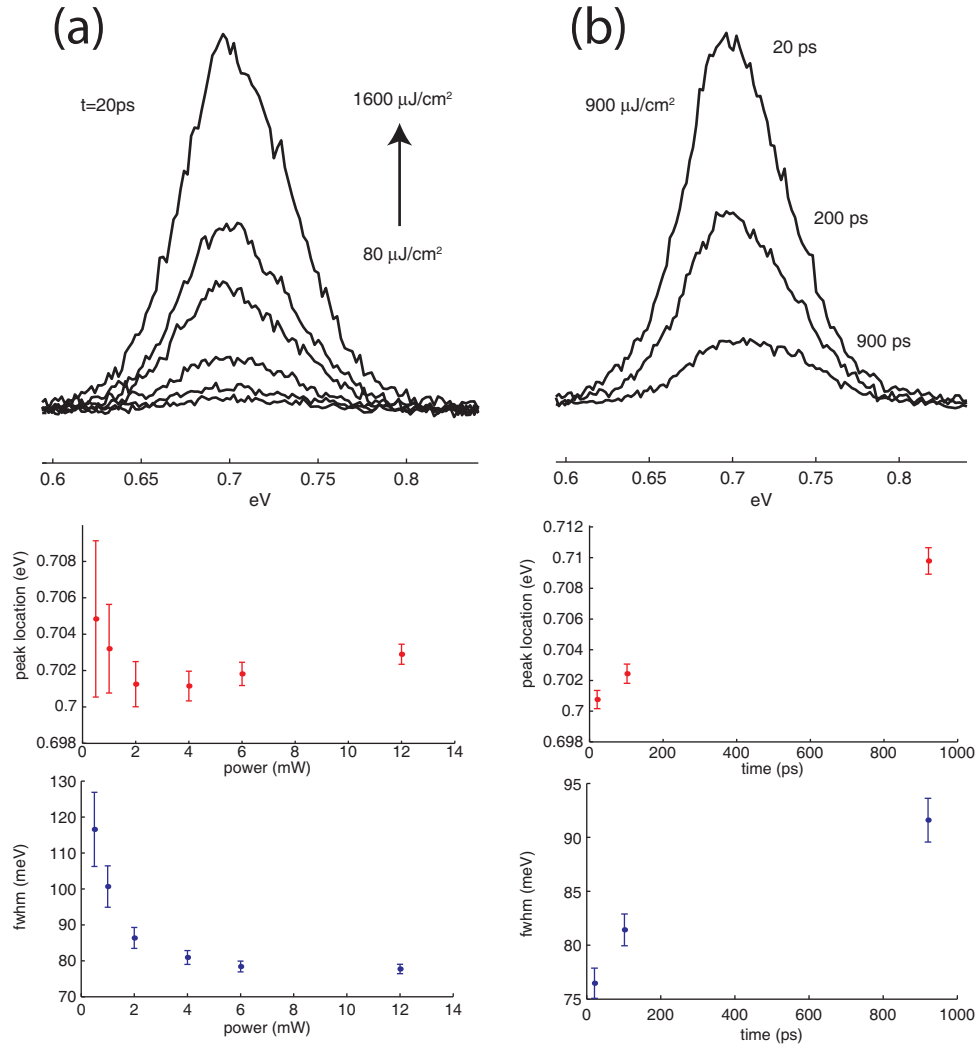
Figure 4-8: (a) Transient PL spectra at t=20 ps of a sample of PbS ($E_{X0} = 0.73$ eV) NCs under 1.55 eV excitation of fluences as noted. (b) Transient emission spectra of the same sample using a fixed 900 $\mu J/cm^2$ excitation fluence 20, 200 and 900 ps after the pulsed excitation. (Bottom) Peak positions and full widths at half maximum extracted from Gaussian fits to the spectra. Error bars represent $\pm 2\sigma$ confidence intervals from uncertainty in the estimates due to noise in the curves.

Chapter 5

Assessment of Carrier Multiplication in PbS and PbSe NCs

To study CM in PbSe and PbS NC samples, we measured tPL decays under 3.1eV excitation. Photons of this energy are well above the CM thresholds that have been previously reported for PbS and PbSe NCs [28, 27]. As in the CdSe case, if carrier multiplication occurs in our samples, it would be captured in the tPL dynamics as a residual BX or higher MX component that persists in the limit of very weak excitation, when no more than one photon is absorbed per NC. We find clear signature of CM in all samples we measured, but contrary to literature reports on CM in lead chalcogenide NCs, the efficiencies are low and we find no enhancement compared to CM in the bulk.

5.1   Experimental results

Fig. 5-1a compares PL dynamics for $E_{X0} = 0.84$ eV PbSe NCs under 1.55 eV and 3.1 eV excitation. As described in Chapter 4, weak 1.55 eV excitation results in flat, single exponential dynamics corresponding to X decay, while at higher power the tPL traces exhibit a fast BX component as well. In contrast, even at low fluence, excitation at 3.1 eV results in decays with a fast component closely following BX dynamics. Fig.

5-1c shows the a_{BX}/a_X ratios obtained from a series of measurements with varying 3.1 eV excitation fluence. Our extrapolation shows that the BX-like feature persists in the zero-power limit $(P \to 0)$, and we thus attribute it to CM. As described in section 3.2.1 the CM yield, y_{cm}, for the sample is then given by Equation 3.1, restated here:

$$y_{cm} = \left(\frac{a_{BX}}{a_X} \right)_{P \to 0} / \left(\frac{a_{BX}}{a_X} \right)_{sat}$$

Because our best estimates of $(a_{BX}/a_X)_{sat}$ are in the range 2.5-4, CM yields are smaller by a factor of ~ 3 than the simple ratio of decay components a_{BX}/a_X would suggest. For the $E_{X0} = 0.84$ eV sample, $y_{cm} \approx 9\%$ at $\hbar\omega/E_{X0} = 3.7$. Fig. 5-1b and 5-1d display similar data for a sample of larger PbSe NCs ($E_{X0} = 0.68$ eV). This sample exhibits a larger fast component in the $P \to 0$ limit, and therefore a larger CM yield of $\approx 23\%$ at $\hbar\omega/E_{X0} = 4.6$.

5.2 Methodology and Analysis

The determination of y_{cm} was done differently than in the CdSe study because of experimental constraints. Our upconversion apparatus is not sensitive enough to accurately measure signals under extremely low excitation levels at which $n \ll 1$. Instead we found that even at the lowest feasible excitation intensities the decays had some power dependence, indicating that BX states were still being created by multiphoton absorption. We therefore had to rely on linear extrapolation to estimate what the decay would look like in the true low power limit. A second difference is that the long integration times prevented us from repeating measurements as many times as we could with CdSe, so we could not obtain estimates of the error or uncertainty in our values by simple repetition.

Measured a_{BX}/a_X are expected to be well described by a linear function of power in the low power limit. Irrespective of CM efficiency at low powers, $p_{\geq 1} \approx n_0$ up to a proportionality constant as it represents the number of NCs that absorbed at least one photon. The BX population in the presence of CM has the form $p_{\geq 2} \approx y_{cm}n_0 + (1 - y_{cm})\frac{n_0^2}{2}$. Amongst the NCs that absorb at least one photon, by definition a fraction
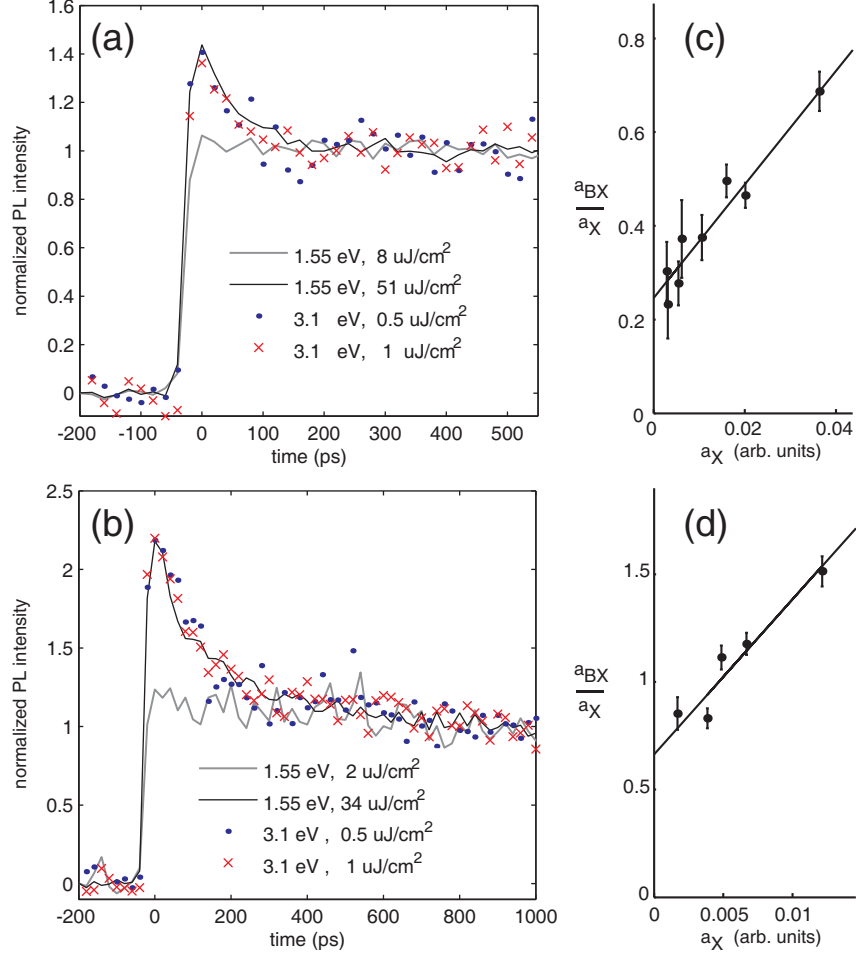
Figure 5-1: (a) Comparison of PL decays from a sample of $E_{X0} = 0.84$ eV PbSe NCs under 1.55 eV and 3.1 eV excitation. Even as the 3.1 eV excitation power reaches the low power limit, the decays continue to exhibit a fast component consistent with BX dynamics. (b) Same as (a) but for $E_{X0} = 0.68$ eV PbSe NCs. (c)-(d) Plots of a_{BX}/a_X vs. a_X for different weak 3.1 eV excitation fluences and extrapolation to the $a_X \to 0$ ($P \to 0$) limit for the samples in (a) and (b) respectively. Dividing this extrapolated value by the $(a_{BX}/a_X)_{sat}$ determined from an independent 1.55 eV power series gives CM yields $y_{cm} = 0.09$ and $y_{cm} = 0.23$ for the two samples at $\hbar\omega = 3.7E_{X0}$ and $\hbar\omega = 4.6E_{X0}$ respectively.

y_{cm} undergoes CM and ends up at least in a biexciton state, while the remaining $(1 - y_{cm})$ fraction can absorb two photons according to the Poisson probability $\frac{n_0^2}{2}$. Therefore:

$$\left(\frac{a_{BX}}{a_X}\right) / \left(\frac{a_{BX}}{a_X}\right)_{sat} = \frac{p_{\geq 2}}{p_{\geq 1}} \approx y_{cm} + \frac{1 - y_{cm}}{2}n_0 = y_{cm} + \gamma P \qquad (5.1)$$

In the last equality, P is power or any other quantity proportional to n_0 and γ is the appropriate proportionality constant. In our analysis, we choose to use the absolute value of a_X in each fit as an internal reference in place of the measured excitation power, exploiting the fact that $p_{\geq 1} \propto n_0$ in the low power limit. This provided a better estimate of the average excitation power in the signal collection volume during some of the longer integrations because of laser fluctuations and drift. Then,

$$\frac{a_{BX}}{a_X} = \left(\frac{a_{BX}}{a_X}\right)_{sat} y_{cm} + \gamma a_X = A + B a_X \qquad (5.2)$$

The slope, intercept, and their standard errors were estimated by maximum likelihood estimation assuming that each a_{BX}/a_X measurement includes normally distributed noise. Because our low power data was significantly noisier than the data at higher powers, the noise level could not be reasonably assumed the same for each point as in standard least squares fitting. Thus, it was important to independently estimate the uncertainty of each a_{BX}/a_X value (Error bars in Figs. 5-1c,d). This was done for each fitted decay by first estimating the noise level from the fit residual and then using it to simulate noisy data which were then fit again. An estimate of the standard error in a_{BX}/a_X was obtained from the statistics of the simulated fit parameters. The estimated errors in a_X alone were negligible in comparison so the fit in Eqn. 5.2 was carried out as if a_X was a controlled variable. The result of the appropriately weighted least squares fits are shown in Figs. 5-1c,d.
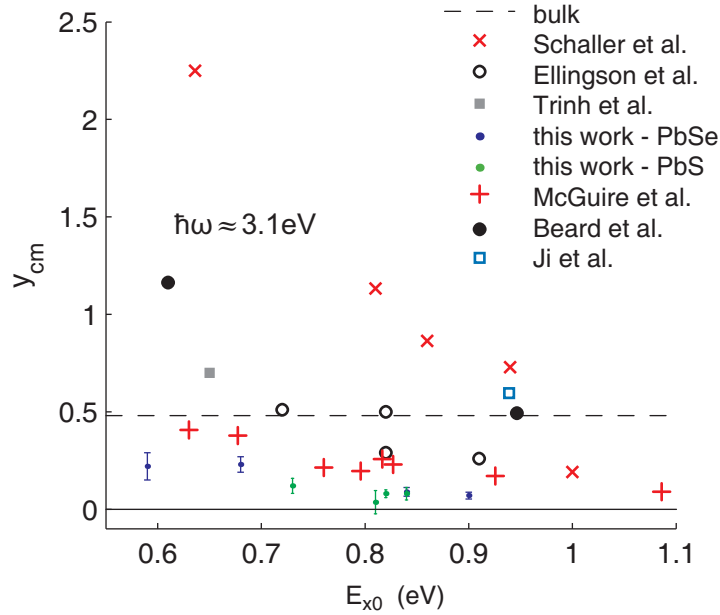
Figure 5-2: Summary of CM yields determined in this study and comparison to literature reports on PbSe NCs at excitation energies $\hbar\omega \approx 3.1$ eV by Schaller et al. [26, 28], Ellingson et al. [27], Trinh et al. [56], and reports published after our own by McGuire et al. [57], Beard et al. [58], and Ji et al [59]. Error bars on our data show approximate 95% confidence intervals reflecting uncertainties due to noise in experimental decays. The dashed line is the CM yield reported for bulk PbS at $\hbar\omega = 3.1$eV by Smith and Dutton [60].

5.3   Summary of results and comparison with NC CM literature data

We have studied a number of PbS and PbSe NC samples and found y_{cm} always in the range of $10 - 25\%$ even in samples for which $\hbar\omega > 5E_{X0}$. As is summarized in Figs. 5-2 and 5-3, our CM yield estimates are significantly lower than those previously reported for PbS and PbSe NCs.

The reports existing at the time we carried out our study had two salient characteristics. First, the CM yields reported were large, even approaching the energy conservation limit for one particular PbSe sample measured by Schaller et al [28]. The second characteristic was large variation in the estimated CM yields reported in the literature. As shown in Fig. 5-2, the data from Ellingson et al.[27] and Trinh et

al.[56] fall bellow the estimates of Schaller at al.[26, 28] by a factor of roughly two, while our own best estimates of the CM yields are an additional factor of 2-3 smaller. In fact, the findings of Schaller et al. predict not only BX formation, but also large triexciton (TX) yields for our largest samples when excited at 3.1 eV, whereas we did not observe any significant TX dynamical components in the PL decays obtained for CM determination.

Since our numerical results were in strong disagreement with the previous reports on NCs based on TA techniques, we considered the possible sources of error in our CM estimates. In Fig. 5-2 we show estimated 95% confidence intervals for y_{cm} related to uncertainties in $(a_{BX}/a_X)_{P\rightarrow 0}$ from noise in the experimental decays propagated into our low power extrapolation scheme (Section 5.2). These uncertainties in y_{cm} are all smaller than ± 0.06 and are likely unbiased.

The part of our methodology most susceptible to a systematic error is the saturation ratio of the BX to X tPL components, $(a_{BX}/a_X)_{sat}$. Any multiplicative error in this quantity translates directly into a multiplicative error in the CM yield, but we have found no rigorous way to quantify the potential error. In our study, we have estimated $(a_{BX}/a_X)_{sat}$ by fitting the sizes of X and BX decay components under 1.55 eV excitation to a population profile and then assuming that this saturation ratio should apply as well to biexcitons created by a CM process. Using these $(a_{BX}/a_X)_{sat}$ values of ≈ 2.5-4, we determined the CM yields in the range of 10-25%. For our results to roughly match the magnitudes of CM reported by Ellingson et al. we would have had to use much smaller values $(a_{BX}/a_X)_{sat} \sim 1$, with an even further reduction to $(a_{BX}/a_X)_{sat} < 1$ required to achieve agreement with the Schaller et al. reports. However, using such small $(a_{BX}/a_X)_{sat}$ would be inconsistent with our direct observation of $a_{BX} > 2a_X$ under sufficiently strong excitation conditions. We are therefore confident in our principal conclusion that the CM yields in the PbSe and PbS NC samples we have studied are significantly smaller than those previously reported for the PbX material system at $\hbar\omega \approx 3.1$ eV.

The Cd^{2+} treatment we used for some samples probably did not appreciably affect CM yields. We studied one sample of fairly large PbSe NCs ($E_{X0} = 0.68$ eV) that

did not require Cd^{2+} treatment, and found that its estimated CM yields were similar to the other large NC samples that were treated with Cd^{2+}. We also checked the effect of the Cd^{2+} treatment by applying it to NC samples that already exhibited adequate surface passivation and found no significant change of the biexciton lifetime or estimated CM yield.

We speculated that the variation between the reports of Schaller et al., Ellingson et al., and our own data must ultimately stem from either systematic differences in data acquisition procedures, variation in the way CM is determined from observed decays, or actual sample-to-sample differences of the CM efficiency. Our study was different in that we used transient PL instead of TA and because we took special precautions in sample handling, like using stirring and concentrated solutions. Indeed, a later report [57] by the same group that initially reported the largest CM yields has clarified that sample degradation and sample-to-sample variation was responsible for the large apparent CM yields reported earlier.

McGuire et al. carried out tPL and TA measurements on PbSe NC samples, studying the effect of solution chemical treatment and sample handling variables like stirring [57]. The CM yields they estimated for stirred solutions are shown in Figs. 5-2 & 5-3 and are much closer to our own values. They found for instance, that two samples of similar size but prepared by different methods showed y_{cm} yields differing by 30%. More importantly they found that if their samples were not stirred, misleading CM-like features appear, as we pointed out in section 3.2.3 for CdSe NCs. In their analysis they argue convincingly that at least a significant portion of the sample degradation under UV exposure involves long-lived charging of the NCs.

5.4 Comparison to CM in the bulk

To our knowledge the only report on CM in bulk PbS or PbSe films is the study on PbS films reported by Smith and Dutton [60]. Their estimated CM yields are included for comparison in Figs. 5-2 & 5-3. These authors studied the photoconductivity of commercial PbS films and found an increase in photocurrent response at shorter
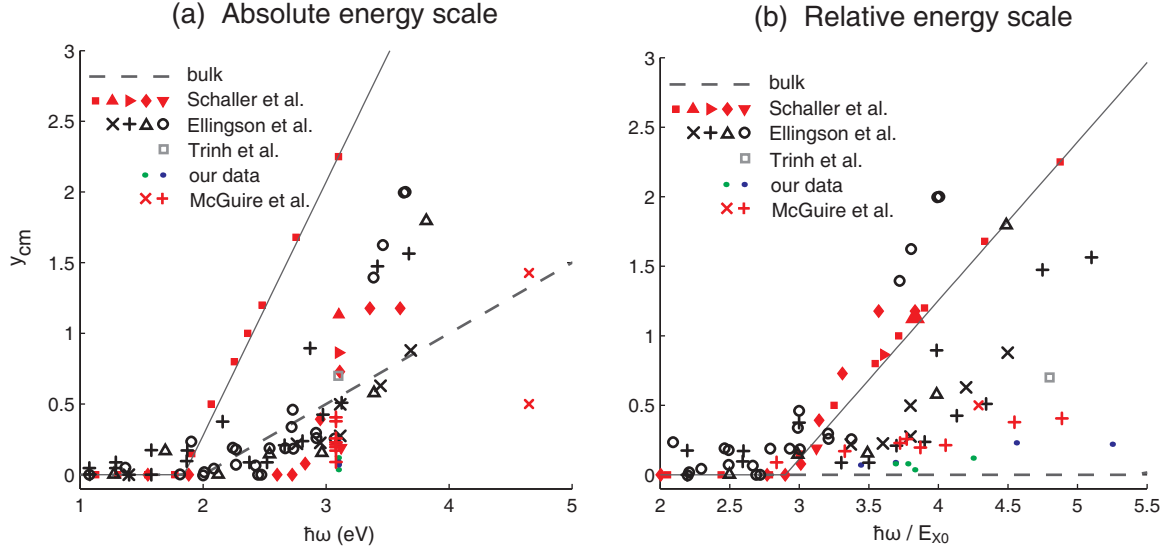
Figure 5-3: CM yields reported in the literature and in this work for PbSe and PbS NCs shown on both an absolute energy and a relative energy scale compared to bulk PbS values reported by Smith and Dutton [60]. The Schaller et al. data are for PbSe NCs with first exciton levels $E_{X0} = 0.636$ (■) , 0.81 (▲) , 0.86 (▶) , 0.94 (◆) , and 1 eV (▼) [26, 28]. The solid line is the fit by Schaller et al. to their $E_{X0} = 0.636$eV data set [28]. Data series from the Ellingson et al. report [27] are shown for PbSe NCs with $E_{X0} = 0.91$ (○), 0.82 (×), 0.72 eV (+), and a 0.85 eV PbS sample (△). The Trinh et al. data is for a 0.65 eV PbSe sample (□) [56]. Our tPL based estimates are shown for the PbS NCs (●) and PbSe NCs (●) reported in this work (all of which were studied at $\hbar\omega = 3.1$eV). CM yields from a more recent report on various PbSe NC samples by McGuire et al. [57] using both TA and tPL at $\hbar\omega \approx 3.1$ eV (+) and TA only at $\hbar\omega = 4.65$ eV (×) are also shown.

wavelengths which they attributed to a CM process, emerging from a threshold $\hbar\omega \approx$ 2 eV and rising approximately linearly to $y_{cm}^{\text{bulk}} \approx 2$ at $\hbar\omega = 6$ eV. It should be kept in mind that there are numerous potential sources of error in this bulk CM determination, some of which we detail below. It is nevertheless interesting to note that the CM yields for NCs reported in the literature appear only modestly enhanced over these bulk values when compared on the absolute energy scale. Except for the data by Schaller et al. on large $E_{X0} = 0.636$ eV NCs which were later attributed to uncontrolled charging by McGuire et al. [57], CM yields are within a factor of ≈ 2 of the bulk report, and they exhibit a similar CM energy threshold between 2-3 eV. A more detailed comparison for excitation energies $\hbar\omega \approx 3.1$ eV was shown in Fig. 5-2. At that energy, Mcguire et al.'s and our results are below the reported value for the bulk, and those of Ellingson et al. [27] and Trinh et al.[56] appear consistent with it. The results of Schaller et al.[28] on larger NCs lie well above the bulk line.

The similarity between NC CM results and the bulk estimates had previously been obscured by the common practice in the NC literature to scale the excitation energy by the size-dependent energy of the ground state exciton before comparing CM yields. This practice followed precedent from the bulk impact ionization literature where an $\hbar\omega/E_g^{bulk}$ scale is typically used for comparison of different materials, and is useful when considering certain aspects of device application. However, we argued in detail [61] that the absolute $\hbar\omega$ axis is a more appropriate basis for comparison of the underlying physical processes. The usual literature comparison at fixed $\hbar\omega/E_{X0}$, shown in Fig. 5-3(b), greatly exaggerates enhancement over the bulk simply because E_{X0} can be significantly larger than E_g^{bulk} due to the very light electron and hole effective masses and small bulk bandgap of the lead chalcogenides. For instance, even without novel NC physics, PbSe and PbS NCs with $E_{X0} > 2E_g^{\text{bulk}}$ will spuriously show at least a two-fold CM threshold reduction.

Reaching a robust conclusion at this stage on the relative strengths of CM in bulk and NC forms is difficult because of potential uncertainties which may exist in the bulk values reported by Smith and Dutton. First, the authors did not present a characterization of the commercial PbS films studied, and it is possible that significant

oxidation may have taken place since no protective coating was used [60]. This is important since exposure to O_2 is known to cause significant changes in bulk PbS photoconductivity [62]. Second, the reported yields are very sensitive to any systematic errors in determining the number of photons absorbed by the film. The third complication is the possible variation of photoconductive gain with $\hbar\omega$. For example, at blue wavelengths carriers are generated on average closer to the film surface, where the greatest concentration of trap states are expected to reside. Moreover, it is difficult to say *a priori* whether the gain would increase or decrease. These considerations highlight the need for a careful determination of CM in bulk films of PbS and PbSe before a definitive comparison with NCs can be made. With the data available at present it is difficult to conclude that nanoscale phenomena contribute to CM enhancement above what might exist in the bulk.

Chapter 6

Theoretical perspectives on Carrier Multiplication

6.1 Basic considerations

We outline the basic physics of carrier multiplication from an elementary perspective here. We start by considering the Hamiltonian for the electronic degrees of freedom in a nanocrystal [63, 64]:

$$H = H_0 + V = \sum_i \epsilon_i c_i^\dagger c_i + \sum_{ijkl} c_i^\dagger c_j^\dagger V_{ijkl} c_k c_l \qquad (6.1)$$

The $c^\dagger$ and c are creation and annihilation operators for electrons. Here H_0 includes the single particle energies ϵ_i of all occupied states, since $c_i^\dagger c_i |\psi\rangle = |\psi\rangle$ if state i is occupied. The second term is the Coulomb-mediated interaction between electrons. The representative summand $c_i^\dagger c_j^\dagger V_{ijkl} c_k c_l$ can be understood as relating to the scattering of an electron in state l with one in state k via the Coulomb interaction and ending up in states i and j respectively. The associated amplitude V_{ijkl}, assuming that the single particle states can be decomposed into products of spin and spatial wavefunctions $|s_i\rangle|\psi_i(r)\rangle$, is given by:
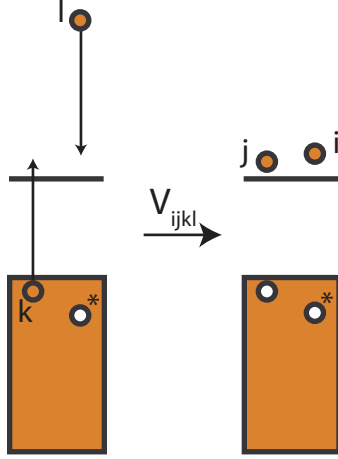
Figure 6-1: Example of a Coulomb coupling resulting in multiplication of carriers. The highly energetic electron drops to a lower level $l \to i$ while promoting a valence electron to the conduction band $k \to j$. The final many-body state can also be arrived at by $l \to j$ with $k \to i$, so these amplitudes must be summed coherently when computing rates. Note that in this "hot-electron" process the original hole, marked with a *, remains a spectator.

$$V_{ijkl} = \langle s_i | s_l \rangle \langle s_j | s_k \rangle \int \psi_i^*(r_1)\psi_j^*(r_2)V(r_2 - r_1)\psi_k(r_2)\psi_l(r_1)\mathrm{d}^3 r_2 \mathrm{d}^3 r_1 \qquad (6.2)$$

The first two factors ensure that spin is not flipped, as the Coulomb interaction acts only through space. We focus now on the terms in V relevant for the carrier multiplication process. Let us consider the case of hot electron carrier multiplication shown schematically in Fig. 6-1. A highly excited conduction band electron in state l collides with a valence band electron in k, losing energy and ending up in state i while promoting the valence electron to j, leaving behind a hole.

The nonzero amplitude of such processes means that many-body states with at least one highly excited carrier will always be mixed with configurations that have more electrons and holes.

$$|\Psi_{\text{1e-1h}}\rangle \xrightarrow{V} a|\Psi_{\text{1e-1h}}\rangle + b|\Psi_{\text{2e-2h}}\rangle + \ldots \qquad (6.3)$$

We now turn to examine the light-matter interaction that initiates the process.

For the purposes of this discussion, we can use the electric dipole approximation and consider absorption from light in a single mode with polarization $\hat{u}$ and frequency ω. The portion of the Hamiltonian that describes this interaction is [65, 64]:

$$H_1 = -\vec{\mu} \cdot \vec{E}(r,t) = \left(\sum_{ij} \langle \psi_i | \vec{\mu} \cdot \hat{u} | \psi_j \rangle c_i^\dagger c_j \right) \sqrt{\frac{\hbar \omega}{2\epsilon_0 \mathcal{V}}} \left(a e^{-i\omega t} + a^\dagger e^{i\omega t} \right) \qquad (6.4)$$

This Hamiltonian is a sum of terms of the form $c_i^\dagger c_j a$ and $c_i^\dagger c_j a^\dagger$, meaning that the creation ($a^\dagger$) or annihilation (a) of a photon is accompanied by the motion of a single electron from an initial state to a final state. When the photon energy is high, the most probable absorption event involves the promotion of an electron deep within the valence band to an empty state high in the conduction band, leaving behind a hole. As discussed above and shown in Eqn. 6.3, this resulting state is not an eigenstate of the electronic Hamiltonian or of the total Hamiltonian including the electron-phonon interaction. It is the evolution of this state under the competing influence of phonon-assisted intraband relaxation and the Coulomb potential V that ultimately determines carrier multiplication yield, as described in Chapter 1 and depicted in Fig. 1-8.

6.1.1 Impossibility of "direct" carrier multiplication

More than one group have proposed that carrier multiplication can occur in NCs "directly" in that the multiplication process is not in competition with intraband relaxation. A first suggestion along these lines was made by Schaller et al. [66], who stated a rate for CM in second order perturbation theory:

$$\frac{2\pi}{\hbar} \sum_{\text{2e-2h}} \left| \sum_{\text{1e-1h}} \frac{\langle \Psi_0 | H_1 | \Psi_{\text{1e-1h}} \rangle \langle \Psi_{\text{1e-1h}} | V | \Psi_{\text{2e-2h}} \rangle}{\hbar \omega - E_{\text{1e-1h}}} \right|^2 \delta(\hbar \omega - E_{\text{2e-2h}}) \qquad (6.5)$$

They argue that since the intraband relaxation appears nowhere in this, that the CM process can happen directly. However, the expression as written has neglected to account for the lifetime and dephasing of the highly excited 1e-1h states, which is precisely where phonon-mediated relaxation plays its role. The perturbation expres-

sion above then requires a modification $E_{\text{1e-1h}} \rightarrow E_{\text{1e-1h}} - i\Gamma$ where Γ is the relaxation rate due to phonon emission. For efficient CM, it is necessary that $\langle \Psi_{\text{1e-1h}} | V | \Psi_{\text{2e-2h}} \rangle$ be of sufficient magnitude compared to Γ.

A more recent work by Isborn et al. [67] has assumed that the significant multiexciton character in highly excited energy eigenstates, represented here in Eqn. 6.3, is enough to explain direct photo-generation of multiexcitons. However, we showed that the light-matter interactions leads, on its own, only to states with a single-particle excitation $|\Psi_{\text{1e-1h}}\rangle$. This state is a superposition of various energy eigenstates, some or all of which may have significant multiexciton character. Nevertheless, the amplitude of all the multiexciton states in the superposition cancel at the instant of photon absorption since $\langle \Psi_{\text{2e-2h}} | H_1 | 0 \rangle = 0$. The superposition state evolves from its purely excitonic initial state $|\Psi_{\text{1e-1h}}\rangle$ to a state with multiexcitonic character at a rate either $\sim |\langle \Psi_{\text{2e-2h}} | V | \Psi_{\text{1e-1h}} \rangle| / \hbar$ or $\sim |\langle \Psi_{\text{2e-2h}} | V | \Psi_{\text{1e-1h}} \rangle|^2 \rho(E) / \hbar$ in the coherent and incoherent limits (Eqn. 6.6). The CM process is therefore brought into competition with intraband relaxation because of this necessary passage of time.

$$H_1 |0\rangle \rightarrow |\Psi_{\text{1e-1h}}\rangle \xrightarrow{V} a(t)|\Psi_{\text{1e-1h}}\rangle + |\Psi_{\text{2e-2h}}(t)\rangle \qquad (6.6)$$

A related issue to "direct" carrier multiplication is the suggestion that CM should result in additional amplitude in the linear absorption spectrum of these samples at high photon energies. Shabaev et al. [68] have concisely explained why this should not be the case. As mentioned before, the light-matter interaction H_1 only connects the ground state $|0\rangle$ to the excitonic portion $|\Psi_{\text{1e-1h}}\rangle$ of any excited electronic eigenstate. Mixing with multiexcitonic states only has the effect of redistributing the oscillator strength $|\langle \Psi_{\text{1e-1h}} | H_1 | 0 \rangle|^2$ of any particular $1e - 1h$ configuration in energy. Total oscillator strength is conserved.

6.2 Calculations of CM efficiency in the literature

Several attempts have been made to theoretically explain features of the initial experimental reports of very efficient CM. The majority of them that try to obtain semi-

quantitative agreement with experiment use a Fermi-golden-rule framework, and are therefore calculated in a similar way to impact ionization rates in the bulk. We will discuss these first.

6.2.1 Impact Ionization

The impact ionization (II) rate for some initial state $|\Psi_{1e\text{-}1h}\rangle$ is the Fermi-golden-rule transition rate for production of another e-h pair via the Coulomb potential:

$$k_{II} = \frac{2\pi}{\hbar} \sum_{2e\text{-}2h} |\langle \Psi_{2e\text{-}2h}|V|\Psi_{1e\text{-}1h}\rangle|^2 \delta(E_{2e\text{-}2h} - E_{1e\text{-}1h}) \qquad (6.7)$$

Treatments differ as to the methods used to calculate the matrix elements and the energy levels of exciton and biexciton states. Franceschetti et al. [69] use atomistic pseudopotential methods to calculate the single particle state structure of PbSe NCs. They assume that $|\langle \Psi_{2e\text{-}2h}|V|\Psi_{1e\text{-}1h}\rangle|$ has a constant value v_{II} between any 1e-1h configuration and any 2e-2h configuration that shares one particle with it. All other matrix elements are zero because either the initial electron or the initial hole must remain a spectator (See Fig. 6-1). The authors estimated v_{II} from measured band-edge biexciton Auger recombination rates, because even though it is a reverse process to II, it is governed by nominally similar matrix elements. They estimate II lifetimes as fast as 10 fs for excitation $\hbar\omega = 3E_g$ in their small, 3.1 nm diameter ($E_g = 1.6$ eV) particles.

Allan and Delerue [70, 71] calculated II rates using tight-binding methods to obtain single particle energies and wavefunctions. Matrix elements $\langle f|V|i\rangle$ were computed for a screened Coulomb interaction using the calculated wavefunctions. They also computed II rates for the bulk using the same tight-binding approach, for comparison. They found that the II rates for NCs are actually *smaller* than in the bulk, converging to the bulk value as particle size increases. The II lifetimes are in the range of 10 fs - 10 ps for energies of interest in PbS, PbS, CdSe and InAs NCs. Rabani and Baer [72] also calculated wavefunctions and matrix elements in their NC II study, but using atomistic pseudopotential theory. They calculate for CdSe NCs a 10-100fs II lifetime
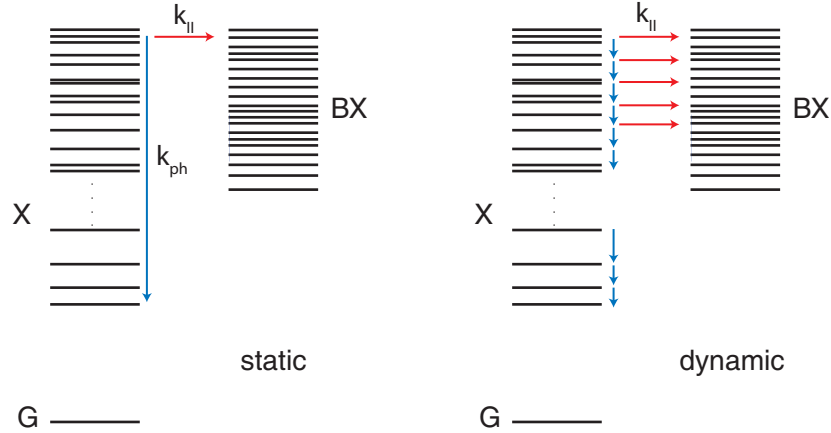
Figure 6-2: (left) Typical scheme for calculation of CM yields from Impact Ionization rates, k_{II}, in the literature. The highly excited X state is assumed to relax in a single step to the band edge. (right) Proposed scheme for CM calculation from k_{II} taking into account the fact that relaxation is a multi-step process that begins immediately after excitation. Using the same $k_{II}(E)$ rates, the two schemes will give different CM yield magnitudes and a different qualitative behavior as a function of excitation energy $\hbar\omega$.

at photon energies $\hbar\omega \approx 3E_g$.

All three studies go on to estimate CM yields by assuming a single rate k_{ph} for intraband relaxation of the excited 1e-1h configuration down to the band-edge and use k_{II}/k_{ph} as an estimate of the branching ratio between CM and relaxation pathways. As will be discussed below, this type of treatment will tend to overestimate CM yield or at least distort its dependence on the hot carrier excess energy.

6.2.2 Intraband relaxation in II-based calculations

When estimating CM yields, typical II treatments tacitly make the following assumption about population dynamics immediately after photon absorption:

$$\frac{\mathrm{d}p_{BX}}{\mathrm{d}t} = k_{II}p_X(t); \qquad \frac{\mathrm{d}p_X}{\mathrm{d}t} = -\left(k_{II} + k_{ph}\right)p_X(t) \tag{6.8}$$

where p_{BX} and p_X are the total biexciton (2e-2h) and exciton (1e-1h) populations following a high energy excitation event. The impact ionization yield becomes :

$$y_{cm} = \frac{k_{II}}{k_{II} + k_{ph}}$$

Such a model effectively assumes that the photogenerated 1e-1h configuration remains at its original excited energy until it either impact-ionizes or relaxes in a single step to the band edge ground 1e-1h state. In fact, the 1e-1h state should begin relaxing in energy immediately due to phonon relaxation. These two treatments are contrasted in Fig. 6-2. A more plausible framing of the competing physical processes could be:

$$\frac{\mathrm{d}p_{BX}}{\mathrm{d}t} = k_{II}(t)p_X(t); \qquad \frac{\mathrm{d}p_X}{\mathrm{d}t} = -k_{II}(t)p_X(t)$$

In a simple model, the time dependent II rate would be given by:

$$k_{II}(t) = k_{II}(E(t)); \qquad \frac{\mathrm{d}E}{\mathrm{d}t} = -k_{E,ph}(E(t))$$

Where $k_{E,ph}$ is a possibly-energy-dependent energy relaxation rate. Under this simplified specification, the CM yield in this more 'dynamic' framework can be solved for exactly:

$$y_{cm} = 1 - \exp\left(-\int_{2E_g}^{\hbar\omega} \frac{k_{II}(E)}{k_{E,ph}(E)}\mathrm{d}E\right)$$

This can be recast to show the significant qualitative difference with the typical 'static' treatment:

$$\text{dynamic:} \qquad \frac{1}{1 - y_{cm}}\frac{\mathrm{d}y_{cm}}{\mathrm{d}\hbar\omega} = \frac{k_{II}(\hbar\omega)}{k_{E,ph}(\hbar\omega)}$$

$$\text{static:} \qquad \frac{1}{1 - y_{cm}}y_{cm} = \frac{k_{II}(\hbar\omega)}{k_{ph}(\hbar\omega)}$$

The II literature [70, 69, 72] tends to overstate CM yields for two reasons. The first is that the value $k_{ph} \approx 1\mathrm{ps}^{-1}$ they use is obtained from experimental reports that probe only the relaxation of the lowest 1e-1h excited states [36, 37, 73, 74].

This corresponds to the rates of the processes denoted in the last few arrows of the relaxation cascade in Fig. 6-2. Bonati et al. [74] have shown using ultrafast transient photoluminescence on PbSe NCs that the intraband decay of higher excited states is faster, as expected from the higher density of electronic states. From the rise-times in their signals after 1.55 eV excitation they deduce very rapid initial energy relaxation rates of $k_{E,ph} \approx 1.5$ eV/ps. One expects that at $E = 3.1$ eV, typical of lead chalcogenide CM studies, relaxation is even faster. The second reason why CM is overstated is the use of the 'static' model described above. Calculated $k_{II}(E)$ rates rapidly increase with the energy of the initial 1e-1h configuration. However, the full benefit of $k_{II}(E)$ at high energy will not reflect on $y_{cm}(\hbar\omega)$ when step-wise 'dynamic' relaxation is taken into account because the system will spend only a very short time at $E \approx \hbar\omega$ before dropping down to an energy at which $k_{II}(E)$ is smaller.

6.2.3 Other theoretical treatments

Aside from the II-based literature, there have been several studies on aspects of CM and alternative proposals for strong CM in NCs. The study of Shabaev et al. [68] is close to the II literature since it does not invoke any new processes. They used a simplified effective mass model of the PbSe electronic structure which allowed them to carry out density-matrix calculations, thus including the possibility of coherence during carrier multiplication. They predict strong CM in PbSe NCs, relying on a near-resonance of some of the 1e-1h and 2e-2h states they calculated. However, their discrete, highly degenerate, energy state structure is at odds with the more continuous density of states found in more detailed atomistic calculations [69, 70].

Two proposals have been made in the literature for CM using mechanisms other than standard 1e-1h$\xrightarrow{V}$2e-2h coupling. Allan and Delerue have suggested [75] the possibility of a mechanism in which midgap electronic states formed by defects function as an intermediate level, reducing the threshold for impact ionization (For instance, in Fig. 6-1 state k would be a filled midgap state instead of a valence band state). They show, however, that such defects would not be able to account for CM enhancement at higher photon energies.

Rupasov and Klimov [76] have proposed an altogether different interaction sequence for carrier multiplication. In their mechanism the ground state is directly mixed in with biexcitonic states which can then undergo *intraband* light absorption, as depicted in Eqn. 6.9 and in contrast with the typical scheme in Eqn. 6.6.

$$|0\rangle \xrightarrow{V} a|0\rangle + b|\Psi_{\text{2e-2h}}\rangle \xrightarrow{H_1} b' |\Psi'_{\text{2e-2h}}\rangle + \ldots \qquad (6.9)$$

The ground state mixing is made possible by V_{ijkl} elements in which k and l are valence states and i and j are conduction states. It should be weak because the unperturbed energies of $|0\rangle$ and $|\Psi_{\text{2e-2h}}\rangle$ differ by at least $\approx 2E_g$. More importantly, in this scheme the biexciton population remains completely unchanged by the absorption of a photon. Therefore, carrier multiplication yields cannot be higher than the biexciton population already mixed into the ground state. The authors of the work were able to argue for strong CM in spite of this because they used a time-dependent perturbation theory approach which inherently neglects depopulation effects.

Lastly, we note the density-of-states arguments put forth by Allan and Delerue in their analysis of CM at extremely high photon energies [71]. They examine the limit in which the Coulomb processes are fast enough such that all excitonic and multiexcitonic configurations that share a total energy $E = \hbar\omega$ are equilibrated. As expected, at $\hbar\omega = 3E_g$, the 2e-2h density of states is higher by several orders of magnitude than the 1e-1h DOS, so $y_{cm} \approx 1$ could be achieved if the Coulomb coupling were strong enough. However, they show that at higher energies the dominant e-h multiplicity is smaller compared to $\hbar\omega/E_g$. For example, at $\hbar\omega = 7E_g$ it is not the 6e-6h but the 4e-4h configurations that have by far the highest density of states, so $y_{cm} > 3$ would be difficult to explain regardless of Coulomb coupling strength. These authors' convincing argument suggests that CM yields may not be able to approach the energy conserving limit.

6.3 Comparison to the Bulk

The original impetus for studying CM in NCs came from the suggestion that it could be significantly enhanced compared to that in the bulk [24]. However, the experimental results we described in previous chapters demonstrate that CM yields are not large, and moreover, that they are not larger than data from reports on the bulk. In this section we discuss NC CM within the context of bulk physics and discuss possible reasons why nanoscale enhancement has not been observed.

In general, the CM yield for a NC material system (for example, CdSe or PbS) may be expected to be determined both by particle size and the photon energy, $y_{cm}(r, \hbar\omega)$, which can be recast as $y_{cm}(E_{X0}, \hbar\omega)$, where E_{X0} is the size-dependent energy of the first exciton level. It is useful for interpreting CM yields from NCs to consider bulk material physics and explore how $y_{cm}(r, \hbar\omega)$ behaves if all phenomena exclusive to the nanoscale are neglected.

In the bulk limit it is intuitively clear that $y_{cm}(r, \hbar\omega)$ is an intensive quantity and thus is independent of r. The competing processes of intraband relaxation and impact ionization have the same rates for crystals of, say, 1 μm and 0.5 μm diameter, resulting in the same CM efficiency. To understand why the impact ionization rate remains constant, one can start from the first-order perturbation theory formulation in Eqn. 6.7. A reduction in volume $\mathscr{V}$ has two effects. First, the average coulomb coupling is enhanced, with $\overline{|\langle \Psi_{2e2h}|V|\Psi_{1e1h}\rangle|^2} \propto \mathscr{V}^{-4}$. [1] However, this is fully balanced by the reduction in average density of states (DOS), since $\rho_{2e2h}(E) \propto \mathscr{V}^4$. As one continues to reduce the volume and approach the nanoscale, the spacing between energy levels becomes wider, but the DOS averaged over sufficiently wide intervals remains the same as in the bulk, with volume scalings $\rho_X(E) \propto \mathscr{V}^2$ and $\rho_{BX}(E) \propto \mathscr{V}^4$. If no new physics are introduced, this process of shrinking the bulk can therefore be continued

---

[1]The steep volume dependence $\overline{|\langle \Psi_{2e2h}|V|\Psi_{1e1h}\rangle|^2} \propto \mathscr{V}^{-4}$ might appear surprising at first. It should be kept in mind that this square matrix element is averaged over *all* 2e2h configurations of nearby energy. However, for $\langle \Psi_{2e2h}|V|\Psi_{1e1h}\rangle \neq 0$, conservation of momentum and spin must be satisfied and one of either the initial electron or hole must not change state. The proportion of final 2e2h states that violate these conditions increases with volume, ultimately resulting in a stronger volume scaling of the averaged coupling coupling than would be expected from averaging only the non-zero terms.
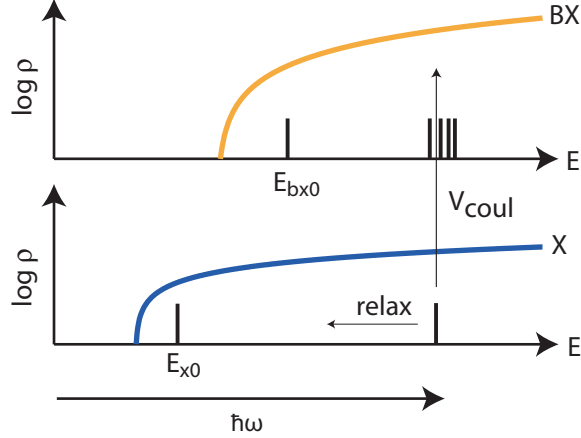
Figure 6-3: Diagram of relevant features and processes for bulk and NC carrier multiplication. The smooth curves are schematics of the bulk 1e1h and 2e2h densities of states, corresponding to X and BX states in an NC. Shown for the case of a NC are the lowest X and BX states at E_{X0} ($> E_g^{\text{bulk}}$) and $E_{BX0} \approx 2E_{X0}$ and a representative highly excited X state formed immediately after absorption of a high energy photon ($\hbar\omega \gg 2E_{X0}$) subject to subsequent intraband relaxation down the X manifold or Coulomb coupling to the BX states. The base of the logarithm in the y axis is arbitrary.

into the nanoscale with the important conclusion that for $\hbar\omega$ well above the $2E_{X0}$ energy conserving threshold, $y_{cm}(r, \hbar\omega) = y_{cm}^{bulk}(\hbar\omega)$. Divergence from this result is only to be expected if new physics appear that have a strong influence on the CM process. The fact that our experimental CM values are if anything below those of the bulk suggests that there is not much nanoscale enhancement. We discuss in turn the reasons why enhancement was expected in the first place.

The most commonly cited rationalizations of CM enhancement in NCs are the possibility of strong coulomb interaction and slow intraband relaxation [24]. It could be argued, for example, that coulomb couplings are significantly enhanced in the nanoscale based on the much faster Auger relaxation rates of band-edge multiexcitons compared to the bulk. This enhancement of Auger rates at the band edge is thought to be due to a relaxation of momentum conservation requirements brought about by the finite nature and abrupt surface of NCs [17, 16]. However, because momentum conservation is not a limiting constraint on impact ionization in the bulk at high excess kinetic energies [70], it is not clear that the nanocrystalline form should exhibit

significant enhancement. As we have mentioned in section 6.2.1, calculations by Allan and Delerue suggest that k_{II} is if anything smaller in PbSe NCs than for the bulk. [70]

Similarly, there is still no evidence of a phonon bottleneck for intraband relaxation at high electron and hole kinetic energies. Due to practical considerations relating to experimental time resolution, most studies on NCs have focused only on relaxation from some of the lowest excited states to the band edge as discussed in section 6.2.1 [36, 37, 74]. Even then, they find very fast picosecond relaxation times. Moreover, at the high excess kinetic energies required for CM, the X manifold is much denser and it seems less likely that a phonon bottleneck effect could play a very large role.

The remaining potential nanoscale CM enhancement mechanisms have to do with the discrete state structure. Certainly, the discrete nature of states in a NC is critical near the energy conservation threshold, as no CM can occur when $\hbar\omega < 2E_{X0}$ even though the bulk 2e-2h DOS is finite. However, if we restrict our attention to $\hbar\omega$ well over $2E_{X0}$, as has been the case when large CM yields have been reported [27, 28], it is plausible that the BX manifold is sufficiently dense that bulk-like behavior could result. Further, even if there were deviations, we would not expect them to be monotonic in either E_{X0} or $\hbar\omega$. Finally, it is possible that there could be strong coupling between X and BX [68], but not enough is known about phase and population relaxation mechanisms of carriers with high kinetic energies to conclude that such effects would be important for CM.

Chapter 7

Two-photon emission efficiency in single CdSe NCs

In this chapter we describe our study of the photon emission statistics of single nanocrystals under pulsed excitation. We analyze in detail the second order intensity correlation $g^{(2)}(\tau)$ of nanocrystal emission and show that the coincident photon arrival feature, often attributed to background or experimental artifacts, is actually due to biexciton emission. We show how the biexciton fluorescence quantum yield η_{bx} is manifest directly in $g^{(2)}(\tau)$ and report for the first time measurements of η_{bx} on single nanocrystals. Measurements of $g^{(2)}(\tau)$ are routinely used to determine whether or not an emitter under observation is a single emitter, but we show that there is more information in $g^{(2)}(\tau)$ than has commonly been thought.

7.1 Introduction

A $g^{(2)}(\tau)$ second order correlation measurement reports on the probability distribution of the time-separation between pairs of photons emitted by a source. When multiphoton emission is suppressed, $g^{(2)}(\tau)$ will show a dip at $\tau = 0$ and the source is said to be "antibunched", considered the signature of an inherently quantum emitter [77]. Fully antibunched sources can be employed as triggered single photon sources, a basic building block for quantum cryptography schemes [78].
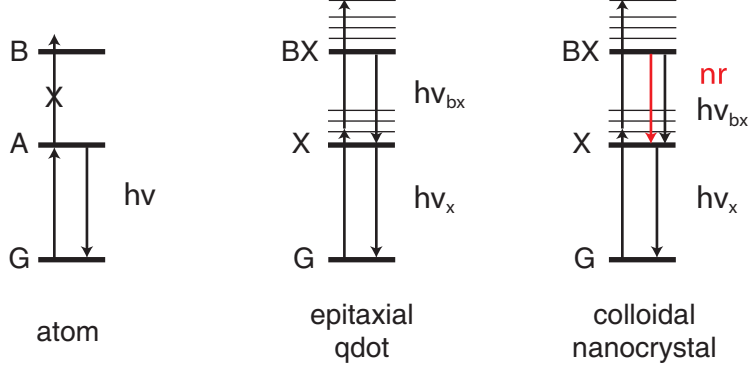
Figure 7-1: Multiphoton emission suppression mechanisms in three classes of fluorescent quantum emitters under laser excitation. In atoms, only one photon is emitted at a time because it is impossible for it to absorb two resonant photons at once owing to their discrete level structures. Epitaxial quantum dots can absorb many photons but the resulting emission cascade can be spectrally resolved due to their narrow linewidths $\Delta\nu \ll |\nu_{bx} - \nu_x|$. Only one photon at a specific frequency can be emitted at a time. In colloidal nanocrystals, $\Delta\nu$ is too large to allow for spectral separation. However, multiexciton emission in NCs is quenched by a nonradiative "Auger"-like process.

To date, photon antibunching has been observed from various types of emitters [77]. In each case multiphoton emission is suppressed in qualitatively different ways, some of which are shown schematically in Fig. 7-1. Atoms, for example, cannot absorb more than one resonant excitation photon before relaxing to the ground state, and thus they only emit one photon at a time [79]. Antibunching can be observed in epitaxial quantum dots by spectrally selecting the emission of just one step in otherwise potentially multiphoton cascades [80]. In colloidal NCs, emission from all multiexcitonic states is suppressed by an efficient "Auger"-like process whereby electrons and holes recombine nonradiatively by simultaneously transferring energy to remaining carriers until just one electron and one hole are left [14]. Antibunching in colloidal NCs [38, 6] is therefore pronounced only to the extent that the Auger recombination pathway is effective.

In this work we study samples of colloidal NCs with slow enough Auger decays that $g^{(2)}$ data display incomplete antibunching attributable to biexciton emission. We show that the normalized integrated area of the 0-time feature in $g^{(2)}$ is given by the ratio of biexciton to exciton quantum yields even in the limit of very weak excitation. We find

that within a sample there is considerable inhomogeneity in the BX quantum yield, which we argue is probably due to inhomogeneity in the BX Auger decay lifetimes that are otherwise obscured by ensemble averaging. The fundamental connection explored here between antibunching and biexciton quantum yield has important implications for the routine use of $g^{(2)}$ in micro PL NC experiments. In particular, analysis of the $g^{(2)}$ data presented in recent reports on blinking suppression in NCs [81, 82, 83] reveals some insights on the possible suppression mechanism itself. These are described in detail below.

7.2   Experimental Method

Colloidal CdSe/ZnS and CdSe/CdZnS (core/shell) nanocrystals were prepared using standard methods. One of the samples was commercial QDOT655 NCs from Quantum Dot Corporation. Samples were spun cast from a poly-(methylmethacryllate) toluene solution onto glass coverslips. Individual nanocrystals were observed by confocal sample-scanned microscopy using an oil immersion microscope objective (100x, 1.40 NA, Plan Apochromat) for excitation from a pulsed diode laser (414 nm, 2.5 MHz, $\approx$40 ps pulsewidth). Typical excitation fluences were 12 μJ/cm^2 (30 nW average power). Some of the signal was dispersed onto a CCD camera for spectral recording. The rest was split and focused onto APD-based single photon detector modules (Perkin Elmer) in a Hanbury-Brown-Twiss geometry using suitable spectral filters. Intensity time traces and $g^{(2)}$ were simultaneously recorded using pulse counters and a correlator card (Timeharp 200). Ensemble transient PL of samples in hexane dispersion were taken using a streak camera (Hamamatsu C5680) with 400 nm excitation derived from a 1 kHz amplified Ti:sapphire laser.

7.3 Theoretical background

The second order cross correlation function $g^{(2)}(\tau)$ of two channels 1 and 2 is defined as:

$$g^{(2)}(\tau) = \frac{\langle I_1(t)I_2(t+\tau)\rangle}{\langle I_1(t)\rangle\langle I_2(t+\tau)\rangle}$$

where $I_1(t)$ and $I_2(t)$ are the intensities of the two channels and the brackets denote time averaging. In our experiments the two channels are produced by splitting a single source into two, and then $g^{(2)}(\tau)$ becomes the autocorrelation of the original source. Since we are working in the few-photon regime, the $I(t)$ must be thought of as quantum mechanical operators [65]. Then $g^{(2)}(\tau)$ is most easily understood as proportional to the conditional probability density that a photon is detected at time τ given that one was detected at time 0. Experimentally, $g^{(2)}$ can be measured with high time resolution using specialized hardware that registers and histograms the time separation between electrical pulses at a "start" and a "stop" input.

In this work, as is fairly standard in the literature, our emitter is excited by a pulsed laser with a pulsewidth much faster and a repetition rate much slower than the emitter's excited state lifetime. Then the $g^{(2)}$ curve consists of a series of discrete peaks. The size of the center peak reflects the probability that two photons were emitted within a single laser cycle while any of the two adjacent $\tau \approx \pm t_{rep}$ peaks originate when two photons are emitted, one each in consecutive laser cycles (See Fig. 7-2). The ratio of the integrated area of the center and side features, hereafter referred to as $g_0^{(2)}$, is given by [84]:

$$g_0^{(2)} \equiv \frac{\int_{-\Delta t}^{\Delta t} g^{(2)}(\tau)\mathrm{d}\tau}{\int_{t_{rep}-\Delta t}^{t_{rep}+\Delta t} g^{(2)}(\tau)\mathrm{d}\tau} = \frac{\langle n(n-1)\rangle}{\langle n\rangle^2},$$

where the random variable n is the total number of photons emitted after an individual excitation pulse and Δt is an appropriate integration range. As is the case for many of the equations we developed for use in this chapter, a full derivation can be found in Appendix B.
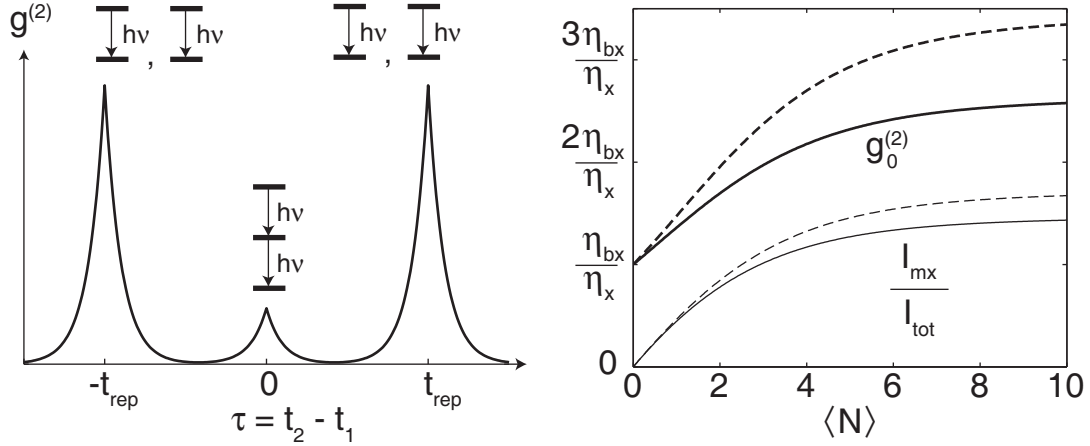
Figure 7-2: (Left) Schematic illustrating the main features of $g^{(2)}(\tau)$ on a single colloidal nanocrystal under pulsed excitation with repetition rate t_{rep}^{-1}. (Right) Calculation of the excitation power dependence of (thick lines) $g_0^{(2)}$, the ratio of the center to $+t_{rep}$ integrated peak areas, and (thin lines) I_{mx}/I_{tot}, the fraction of the total emission intensity due to multiexcitons, for a CdSe NC, plotted in units of η_{bx}/η_x, the ratio of the biexciton to exciton fluorescence quantum yields. $\langle N \rangle$ is the average number of photons absorbed. Solid curves are for $\eta_{bx}/\eta_x = 0.1$ and the dashed curve represents the $\eta_{bx}/\eta_x \to 0$ limit. A simple model was used to provide values for the quantum yields of higher multiexcitons based on the assumed η_{bx} (Appendix B.3). For small $\langle N \rangle$, $g_0^{(2)}$ grows linearly from its η_{bx}/η_x intercept and then saturates at high powers owing to the diminishing quantum yield of higher multiexcitons.

7.3.1 NC emission statistics

The emission of a single NC under pulsed excitation is governed by two types of random processes. Firstly, the NC absorbs a Poisson-distributed random number of photons N. The resulting N electrons and holes recombine one by one in a cascade to the ground state, each step of which can be radiative or nonradiative ($\xi_m = 1$ or $\xi_m = 0$). In the limit that $\langle N \rangle \to 0$ it can be shown that (see Appendix B):

$$g_{0\ \text{dot}}^{(2)} = \frac{\langle n_{\text{dot}}(n_{\text{dot}} - 1) \rangle}{\langle n_{\text{dot}} \rangle^2} \to \frac{\langle \xi_1 \xi_2 \rangle}{\langle \xi_1 \rangle^2} \approx \frac{\eta_{bx}}{\eta_x} \tag{7.1}$$

Here, $\eta_x = \langle \xi_1 \rangle$ and $\eta_{bx} = \langle \xi_2 \rangle$ are the luminescence quantum yields of the 1e-1h ("exciton" or X) and 2e-2h ("biexciton" or BX) configurations respectively, and it has been assumed that the X and BX fluorescence processes are independent of each other

[1] . Therefore, at very low powers when $\langle N \rangle \to 0$ a residual 0-time peak will persist in the normalized $g^{(2)}(\tau)$ due to biexciton emission. This is remarkable because biexciton emission itself constitutes a vanishingly small fraction of the total NC emission as the excitation intensity is minimized. We can understand this apparently non-intuitive result as follows. The size of the center 0-time peak reflects the likelihood of biexciton creation and subsequent two-photon emission. The probability of this event vanishes as $\langle N \rangle^2$. The side peaks are due to creation and emission of two excitons in consecutive laser cycles. The probability of these events involving absorption from two consecutive pulses also vanish as $\langle N \rangle^2$, and therefore $g^{(2)}_{0\,\mathrm{dot}}$ approaches a constant value, η_{bx}/η_x, as $\langle N \rangle \to 0$ even though biexcitons are created only very rarely when compared to excitons. Fig. 7-2 shows a calculation of the evolution of $g^{(2)}_0$ for higher $\langle N \rangle$. We note that an analogous result, $g^{(2)}(\tau = 0) = \eta_{bx}/\eta_x$, holds for the case of weak continuous excitation.

7.3.2 Sources of error and background

In a real experiment there are extraneous sources of error that modify $g^{(2)}_0$. Uniform background, such as from dark counts, scales and offsets the measured correlation curve, $g^{(2)}(\tau) = 1 + (1 - b_1)(1 - b_2)(g^{(2)}_{\mathrm{pulsed}}(\tau) - 1)$, where b_1 and b_2 are the fraction of the start and stop channel intensities due to background. These are easily measured and are typically very small ($b < 1\%$). Pulsed background, like laser scatter or laser induced matrix fluorescence, has an analogous effect, resulting in $g^{(2)}_0 = 1 + (1 - \mathfrak{b}_1)(1 - \mathfrak{b}_2)(g^{(2)}_{0\,\mathrm{dot}} - 1) \approx g^{(2)}_{0\,\mathrm{dot}} + \mathfrak{b}_1 + \mathfrak{b}_2$, where the $\mathfrak{b}_j$ are the pulsed background fractions. Lastly, the presence of another identical NC somewhere within the collection volume, contributing $y_j = 1 - x_j$ fractions of the $j = 1, 2$ channels' signal, leads to $g^{(2)}_0 = g^{(2)}_{0\,\mathrm{dot}} + (x_1 y_2 + x_2 y_1)(1 - g^{(2)}_{0\,\mathrm{dot}})$. Importantly, the quantities $\mathfrak{b}_{1,2}$ and $y_{1,2}$ can be estimated from intensity traces, and we will be able to show that they are too small

---

[1]Because ξ are either 0 or 1, we can write $\langle \xi_1 \xi_2 \rangle = \langle \xi_2 \rangle \cdot \langle \xi_1 \rangle|_{\xi_2=1}$. Both possible sources of X-BX quantum yield correlation are not expected to play a big role. If the BX emits there is no local energy release to modify the subsequent X emission $\langle \xi_1 \rangle|_{\xi_2=1} \approx \langle \xi_1 \rangle$. If a hidden stochastic variable like surface quality controls ξ_1 and ξ_2 we expect them to be positively correlated so $\langle \xi_1 \rangle|_{\xi_2=1} \geq \langle \xi_1 \rangle$. However, for our experiments the relevant $\langle \xi_1 \rangle$ is already ≈ 1.

to account for the observed $g_0^{(2)}$. Our analysis also shows that η_{bx}/η_x is an absolute minimum for the depth of antibunching, a result that applies to the continuously-excited case as well.

7.3.3   Generalization to time-dependent statistics

The results so far assume a fixed statistics of photon emission, but it is well known that nanocrystals blink [10]. Our photon cross-correlation histograms are accumulated over a period of time during which η_x and potentially η_{bx} change stochastically. Because the 0-time and the side peak are collected in parallel and then divided to obtain $g_{0\,\text{dot}}^{(2)}$ it can be shown that:

$$g_{0\,\text{dot}}^{(2)} = \frac{\langle \eta_x(t)\eta_{bx}(t)\rangle_t}{\langle \eta_x(t)^2\rangle_t}$$

Where $\langle \cdot \rangle_t$ denotes a time average over the course of each experiment. It is seen that $g_0^{(2)}$ weighs more heavily the η_x and η_{bx} values during bright periods. We point out that for binary on-off blinking $g_{0\,\text{dot}}^{(2)}$ is given simply by $\eta_{bx}^{\text{on}}/\eta_x^{\text{on}}$. [2] These considerations taken together show that even after including the background and blinking effects of a real experiment, $g_0^{(2)}$ can remain a direct indicator of biexciton emission efficiency.

7.4   Experimental Results

Figure 7-3 shows data from an experiment on a single CdSe/CdZnS NC under weak excitation. We ensured that our data is representative of the $\langle N \rangle \rightarrow 0$ limit by operating far from signal saturation and checking that there was little consistent variation in our $g_0^{(2)}$ values as a function of power. In all NCs we studied the center peak clearly rises above background levels. In the data shown, $g_0^{(2)} = 6\%$. For most dots the time traces showed nearly digital on-off blinking and all dots exhibited off periods with very low count rates.

---

[2] Since we are concerned only with $g^{(2)}(\tau)$ for the $\tau \sim 0$ center and $\tau \sim \pm t_{\text{rep}}$ side peaks, even rapid μs timescale switching between on and off states will result in $g_{0\,\text{dot}}^{(2)} = \eta_{bx}^{\text{on}}/\eta_x^{\text{on}}$.
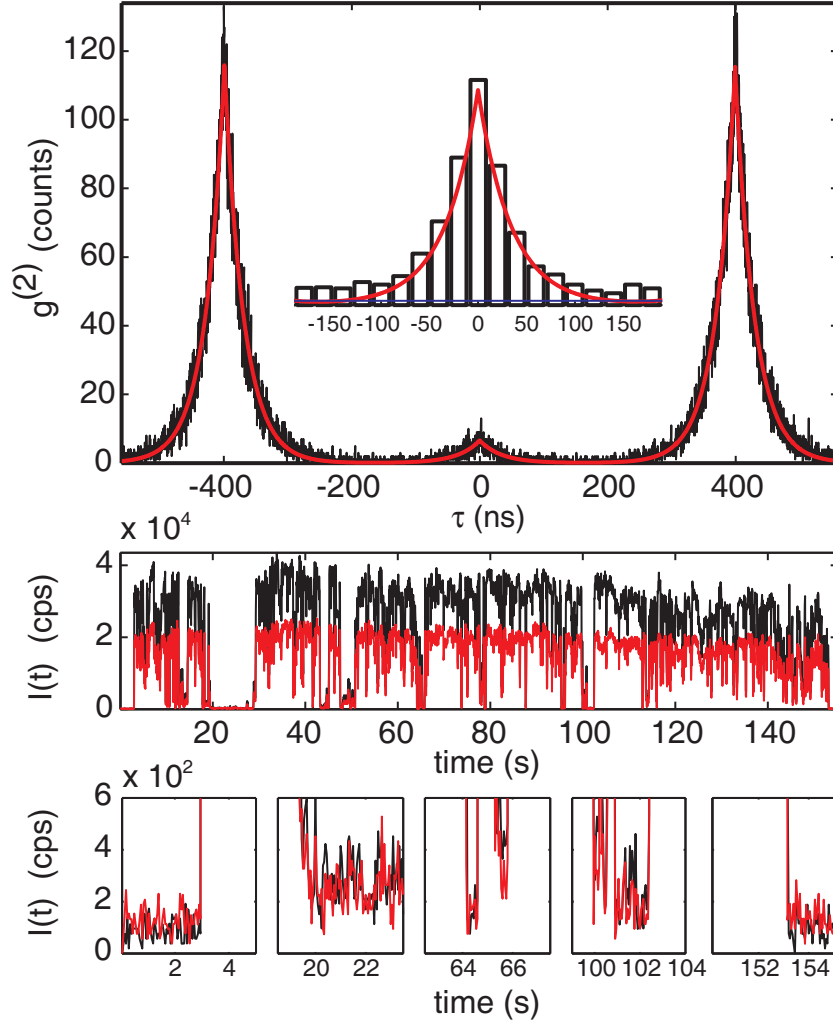
Figure 7-3: (Top) Measured, unnormalized $g^{(2)}(\tau)$ from a single CdSe/CdZnS NC under $\approx 12~\mu J/cm^2$ pulsed excitation, representative of the $\langle N \rangle \ll 1$ limit. The ratio of the center to side peak integrated areas is $g_0^{(2)} = 6\%$. Inset is a 20ns-binned detail of the center peak. Red lines are a fit to the sum of three two-sided exponentials. (Middle) Time traces of intensity in start and stop channels (black and red) during the $g^{(2)}$ acquisition. (Bottom) Details showing off-state intensities. The events in the first and last panel correspond to switching the excitation laser on and off.

7.4.1 Assignment to BX emission

We estimate by analyzing the intensity time-traces that sources extraneous to the single NC under study can account for a contribution to $g_0^{(2)}$ of at most $\approx 1.5\%$. A uniform background, estimated from on-state intensities and measured dark counts, was substracted before calculating $g_0^{(2)}$. The pulsed background signal levels $\mathfrak{b}_{1,2}$ can be estimated from a clear area in the sample, or they can be bounded above by the darkest off-intensities (see Fig. 7-3bc for a representative example). Its contribution to $g_0^{(2)}$ is $\approx 0.3\%$ or, conservatively, no more than 1.5%. [3] The same off-state intensity analysis suggests that no other NCs contribute appreciably to $g_0^{(2)}$, which was expected from the low surface density of NCs in confocal images. We rule out the possibility that our NCs are clustered because experimentally we observe similar emission intensities for all NCs belonging to a sample. The 0-time features in our $g^{(2)}$ data are thus a demonstration of the BX emission signature that is predicted to persist at arbitrarily low excitation intensity.

7.4.2 Summary of $g_0^{(2)}$ data

Fig. 7-4 shows a summary of our data on individual dots. The $g_0^{(2)}$ values we measure correlate with our measured ensemble BX lifetimes but they also display significant spread from dot to dot. While repeated measurements of $g_0^{(2)}$ of a single NC also show some variation (typically less than 20-30%), it is significantly smaller than the dot-to-dot inhomogeneity. We show in Fig. 7-5 the average $g_0^{(2)}$ for all NCs we measured. The only data point we have excluded was a single measurement on a dot from sample (e) which showed an extremely low X lifetime of ≈ 6 ns along with poor, multi-state blinking, and low emission intensity.

---

[3]It is likely that the signal level of even the darkest observed off states are mostly due to weak NC emission and not background, as suggested by our observation that there are usually other off periods with higher but comparable emission intensities. This suggests the lower 0.3% bound is more appropriate.
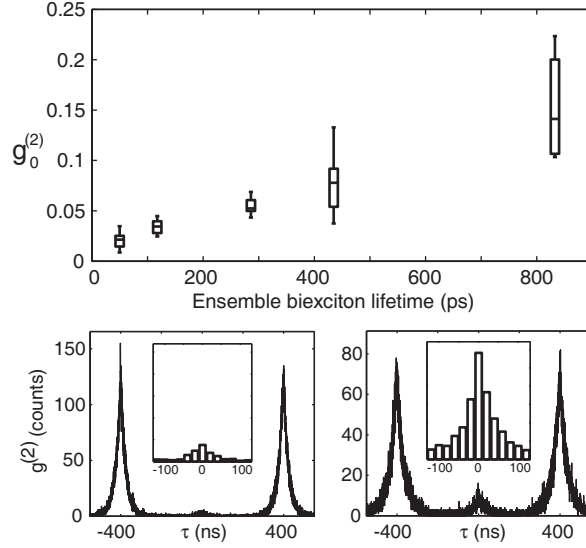
Figure 7-4: (Top) Box and whiskers plot of our measured values of $g_0^{(2)}$ on individual NCs plotted against each sample's ensemble biexciton lifetime. The box edges indicate the first and third quartiles, the line within indicates the median value, and the external lines the minimum and maximum. (Bottom Left) Raw $g^{(2)}$ data of an NC from the sample with shortest BX lifetime. In this case $g_0^{(2)} = 2.1\%$. The inset shows a 20ns-binned detail of the center feature. (Bottom Right) Same but for an NC from the sample with the longest BX lifetime, showing $g_0^{(2)} = 12.8\%$
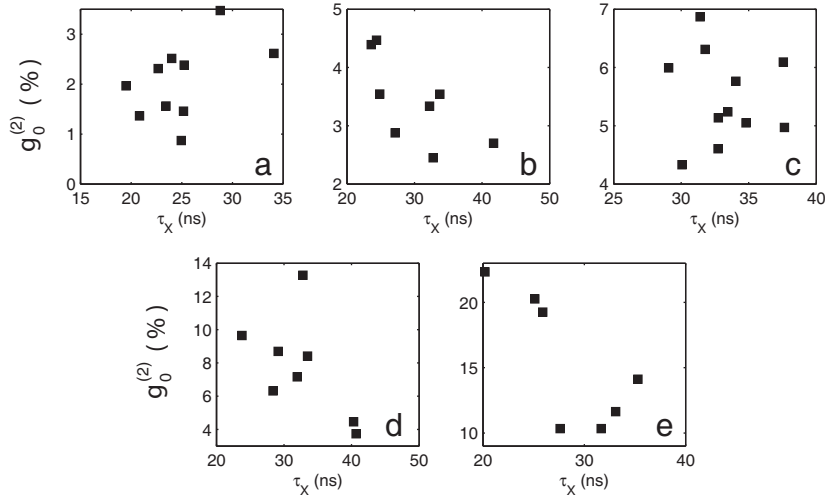
Figure 7-5: Plot of measured $g_0^{(2)}$ against the X lifetime τ_x obtained from fitting the shape of the peaks in $g^{(2)}(\tau)$ for the individual dots we measured in each sample. The ensemble BX lifetime of samples (a) through (e) are 50, 120, 290, 430, and 830 ps. We observe that, in general, τ_X does not account for the variation in $g_0^{(2)}$ within any of the samples

7.5 Interpretation of experimental $g_0^{(2)}$

The majority of the dots we studied exhibited nearly binary on-off blinking in intensity time traces, and those that did not showed similar $g_0^{(2)}$ values. Under these conditions, $g_0^{(2)} \approx \eta_{bx}^{\text{on}}/\eta_x^{\text{on}}$.

We argue, following Brokmann et al. [39] and Fisher et al. [40], that the X quantum efficiency during on-periods can be well approximated by unity. Brokmann et al. measured the radiative rate of single NCs and found that it accounts for almost the entirety of the total decay rate of those NCs. Fisher et al. analyzed the distribution and time dependence of photoluminescence decays of single NCs and concluded that the highest intensity periods probably correspond to $\eta_x \approx 1$. Then $g_0^{(2)}$ becomes $\approx \eta_{bx}$. Indeed, the average $g_0^{(2)} \approx 15\%$ for NCs in our QDOT655 sample is in good agreement with the $\eta_{bx} \approx 11\%$ ensemble estimate by Fisher et al.[7].

7.5.1 Source of η_{bx} inhomogeneity

Dot to dot variability in the BX quantum yield η_{bx} could be attributed to changes in the BX radiative rate, the BX nonradiative rate, or both. Due to the full occupancy of the band edge electron states, all band edge BX configurations are equally bright and k_{bx}^{rad} is determined just by the spatial overlap of the electron and hole wavefunctions (see section A.1). Large changes in this overlap are not expected, and they would affect the X radiative rate. However in our data (Fig. 7-5) there is no evidence of a clear correlation between $g_0^{(2)}$ and τ_X on individual NCs.

An inhomogeneous τ_{bx} within a sample is plausible because the Auger relaxation process is strongly dependent on electronic defects. Spatially smooth wavefunctions have little overlap with the high kinetic energy final state resulting from Auger relaxation. It is believed that the process is efficient in NCs because of lattice defects that "roughen" the ground "particle-in-a-box" states [16]. Subtle variations in the quality and smoothness of the core/shell and shell/ligand interfaces could therefore affect the sensitive Auger mechanism without affecting other observables like quantum yield, radiative rates or emission wavelength in measurable or systematic ways.

Inhomogeneity in τ_{bx} can be easily hidden in ensemble population dynamics since it affects only the long tail of the averaged BX decay, which is difficult to isolate from the overlapped X dynamics.

7.6 Implications for blinking suppression

Our results suggest that care must be taken when using $g^{(2)}$ for routine diagnostic analysis of single NCs. Commonly, complete antibunching is seen as a necessary and sufficient condition to prove that only a single NC is under observation in microPL experiments. In fact, unless it is known beforehand that the BX quantum yield is negligible, single NCs may not show complete antibunching. Using only NCs that do may result in sample bias. On the other hand, if an analysis of other observables such as spectral wandering or digital blinking strongly suggests that an object is a single NC, then the measured $g_0^{(2)}$ can be attributed to biexciton emission.

Application of the direct relationship discussed here between $g_0^{(2)}$ and η_{bx} to recent published data on blinking suppression reveals insights into the potential suppression mechanism. Mahler et al. [81] and then Spinicelli [82] et al. in a follow-up reported CdSe/CdS (core/shell) NCs that switch between an on state and a "grey" state with appreciable fluorescence. In their $g^{(2)}(\tau)$ data, the 0-time coincidence peak is almost completely absent. More recently, Wang et al. [83] have reported ZnCdSe/ZnSe (core/shell) NCs that emit steadily without observable blinking and show strong antibunching in a continuously-excited photon cross correlation measurement. In both these cases, blinking suppression was therefore achieved without suppression of the BX nonradiative decay pathway. A third group reporting blinking suppression in large-shell CdSe/CdS [85] did not show $g^{(2)}$ data, but in a follow-up García-Santamaría et al. [86] carried out ensemble transient PL measurements on those samples. Intriguingly, they found long ≈ 10 ns BX lifetimes and estimated large $\eta_{bx} > 34\%$ BX quantum yields, directly conflicting with the nearly complete antibunching seen in Mahler et al. and Spinicelli et al.'s $g^{(2)}$ data on nominally similar CdSe/CdS structures.

To our knowledge, there are two ways to accommodate simultaneous blinking sup-
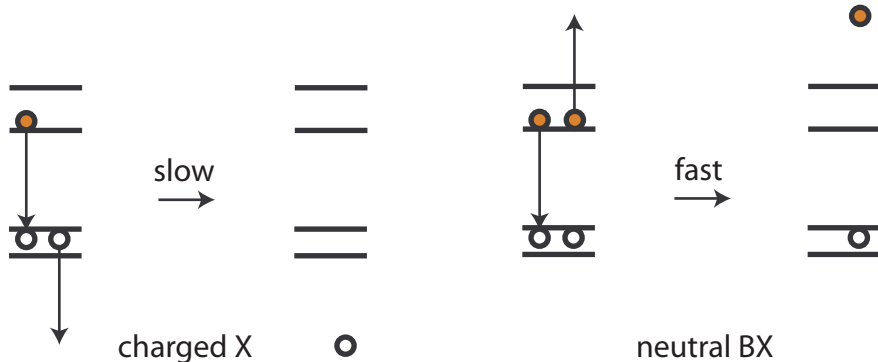
Figure 7-6: Scheme showing how a charged exciton can have a slow non-radiative "Auger" decay while a neutral biexciton's decay can be fast. Within the charging model of blinking, this type of asymmetry between hot hole (left) and hot electron (right) "Auger" pathways is necessary to explain literature results demonstrating suppressed blinking but quenched biexciton luminescence.

pression and efficient BX nonradiative recombination within the traditional charging model of blinking. The charging model proposes that the off-state nonradiative mechanism is Auger recombination involving a long lived free electron or hole left over from an exciton ionization event. One possibility is that in non-blinking NCs Auger processes remain fast but the charging event does not occur or is rapidly reversed by recombination. This cannot account for the "grey" states observed for the CdSe/CdS NCs, but is compatible with the full blinking suppression observed by Wang et al. The other option relies on the possibility that Auger decay rates are very different for two electrons and one hole, $2e1h \rightarrow 1e^*$ resulting in a hot electron, and for two holes and one electron, $1e2h \rightarrow 1h^*$ resulting in a hot hole as shown in Fig. 7-6. If the typical off-state is positively charged, it may still emit brightly if the hot hole pathway is suppressed, while the neutral BX quantum yield may remain low because the hot electron pathway is still rapid.

Chapter 8

Tests of the charging model of blinking

Semiconductor nanocrystals are known to emit light intermittently, i.e., to "blink". The blinking mechanism is usually attributed to a nonradiative Auger-like process involving excess free carriers. In this chapter, we study the blinking of exciton and, for the first time, multiexciton states of single CdSe(CdZnS) core(shell) nanocrystals. We compare the experimental on-off ratios and find them to be much larger than those that would be predicted in the charging model. The work discussed in this chapter was done in collaboration with Jing Zhao as an equal contributor.

8.1 Introduction

Since the discovery of fluorescence intermittency (blinking) in single CdSe semiconductor nanocrystals (NCs)[10], significant effort has been devoted to understanding the mechanism of its dynamics both from a fundamental science perspective and with the aim of control by judicious choice of materials. Blinking plays an important, often detrimental, role in the performance of NCs in a variety of applications. For example, LED brightness [1, 2, 52] and NC lasing [8, 4, 5] efficiency are compromised if a significant fraction of nanocrystals are off at a given moment, and the use of single NCs both as biological trackers [87] and as single photon sources [38, 6, 7] is also limited

when the NC blinks off. The ability to suppress blinking in NCs would increase their usefulness. Although blinking suppression in specific NC architectures has recently been demonstrated [81, 85, 83], the mechanism of blinking or its suppression are not fully understood, and rational design remains a challenge.

Blinking was first observed in the photoluminescence (PL) time traces of single NCs under continuous excitation [10]. These were found to consist of periods when the NC emits strongly, with a constant brightness (on), separated by periods of very weak or no signal (off). The distribution of lengths of on and off periods in CdSe NCs under a range of experimental conditions and surface treatments appears to follow a power law over many decades in time [88, 89] with an exponential cut-off of the probability at very long times [89, 90]. The cut-off is sensitive to illumination intensity, temperature and environment, and while the power law exponent is usually near -1.5, it does vary in the literature and it appears to show a weak dependence on the dielectric constant of the surrounding matrix [91]. Blinking has been observed in other materials as well: Si nanocrystals, for example, show intermittency but with rather different dynamics [92].

Theoretical models for understanding blinking and its statistics were developed soon after its discovery in CdSe NCs. Invoking a mechanism that was known to explain photodarkening of CdS nanocrystal-doped glasses [25], it was proposed that the off state NC is in fact a charged NC [10, 19]. As discussed in Chapter 1, in the presence of this additional carrier, say a hole, any photo-generated electron-hole pair could efficiently recombine and simultaneously promote the extra hole deep into the valence band via a single energy-conserving coulomb interaction. Experiments on multiexciton population dynamics had already shown that such "Auger"-like non-radiative processes are very efficient in NCs [14, 7, 16]. Many physical pictures have been developed since then to explain the intriguing statistics of the blinking process [89, 93, 94, 95, 96], most focusing on possible mechanisms of NC ionization and subsequent neutralization. The fundamental element of the original off-state mechanism remains widely accepted today as it was originally hypothesized: regardless of how the NC becomes charged, it is the fact that it is charged and hence subject to non-

radiative Auger relaxation that renders it non-emissive. Experiments have shown that NC emission can be quenched reversibly by charging [97, 98, 99, 100] and there is evidence that NCs undergo stochastic charging under illumination [101, 102], but no experiment to date has directly proven that an off NC is a charged NC.

In this work we test the key assumption of the charging model by examining the fluorescence intermittency of NCs with comparatively slow multiexciton Auger decay rates [7]. We exploit the fact that charged excitonic states and normal multiexcitonic states share the Auger process as a common fluorescence quenching mechanism to estimate the on-off intensity ratios for exciton and multiexciton emission within the charging model framework. We then measured on-off ratios of exciton and, for the first time, multiexciton emission, and have found them both to be significantly larger than would be predicted by the charging model. In particular, the NCs we studied had off-state exciton quantum yield that are 10-fold smaller than expected for a charged exciton. We reach a general conclusion that the "off" nonradiative decay pathway is too fast to be explained by Auger processes involving just a single additional carrier. We discuss possible modifications and extensions of existing models that would be compatible with our findings.

8.2   Experimental Methods

High quantum yield(QY) ($\approx 80\%$) CdSe(CdZnS) core(shell) NCs of 5 nm core radius (Quantum Dot Corp.,Catalog No. 1002-1) were used in the current study and their photoluminescene is centered at 1.89 eV (655 nm). For single NC experiments, a dilute solution of the NCs in a poly-methylmethacrylate (PMMA) matrix was spin coated onto a Gold Seal cover glass (Electron Microscopy Sciences) to produce a low-density field of single NCs. Single NCs were excited using a frequency-doubled, amplified Ti:sapphire laser at 400 nm (3.1 eV) or a pulsed diode laser at 414 nm (3.0 eV) (PicoQuant), both with 5 MHz repetition rate. The emission was split and directed into two avalanche photodiodes (Perkin Elmer) in a Hanbury-Brown-Twiss geometry. Suitable spectral filters - a band pass of 610±5 nm (2.02 $\sim$ 2.05 eV) and
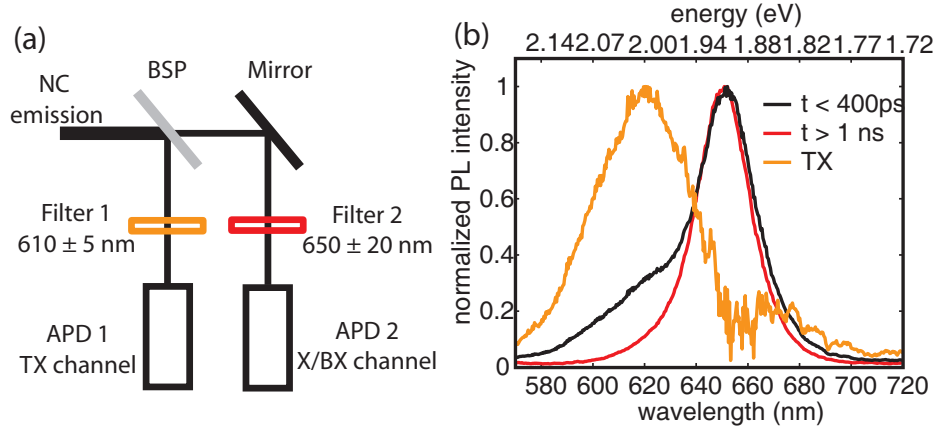
Figure 8-1: (a) Schematic illustration of the experimental setup; (b) transient PL of ensemble CdSe(CdZnS) core(shell) NCs integrated for $t < 400$ ps and for $t > 1$ ns. At short times there is a blue-shifted shoulder from 1P-1P emission of TX and higher multiexcitons, which we isolate ("TX") by subtraction of the long time spectrum after scaling and shifting. Figure composed in collaboration with J. Zhao

a band pass of 650±20 nm (1.85∼ 1.97 eV) - were inserted in the optical path to isolate multiexciton 1P-1P emission at one APD (TX channel) and band edge 1S-1S emission at the other (X/BX channel). A schematic illustration of the experimental setup is shown in Fig. 8-1. Photon cross-correlation measurements were done with a Timeharp200 card (Picoquant). Intensity time traces from both channels were simultaneously acquired with a pulse counter. Spectra of single NCs were monitored using a charge-coupled device (Pentamax, Princeton Instruments). Transient spectra from NCs in hexane solutions were obtained on a streak camera (Hamamatsu) after excitation at 400 nm (or 3.1 eV) by a frequency-doubled, amplified Ti:sapphire laser (1 kHz). All measurements were performed at room temperature.

8.3   Results

8.3.1   X on-off ratio

A measurement of a standard blinking time trace on a single NC is shown in Fig. 8-2. The "on" counts of the band edge emission is ∼ 40,000 cps while the "off" count rate is ∼ 300 cps. The on/off ratio of band edge emission is therefore greater than 100:1.
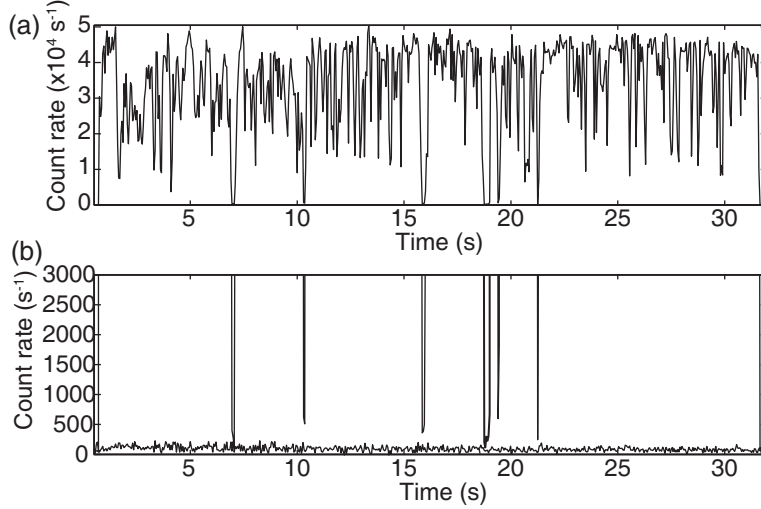
Figure 8-2: (a) Blinking time trace of a single NC and (b)an expanded view of the baseline showing off periods with count rate as low as ~ 300 cps. Figure composed by J. Zhao

The off-state quantum yield is therefore less than 1%. Similarly low off-state QYs were observed from most single NCs. For comparison, we note that the biexciton QY of this sample has been estimated as $\approx 11\%$ [7].

8.3.2 Multiexciton emission intermittency

In CdSe NCs, multiexcitons starting from the triexciton onwards, in addition to emitting at the band-edge 1S-1S energy, also emit at the blue-shifted $1P-1P$ band because of electron occupation of the $1P_e$ level [9, 103, 7, 104] as shown in Fig. 8-1(b). With the choice of appropriate spectral filters and given our sample's relatively long multiexciton lifetimes [7], we have been able to separate the 1P-1P emission of multiexcitons from the band-edge emission.

Representative data from 3.1 eV excitation are shown in Fig. 8-3. Fig. 8-3a shows the PL intensity time traces collected in both X/BX and TX channels of a single NC at 10 μJ/cm^2 (assuming a diffraction limited spot size). At low excitation power, no multiexcitons are expected to be generated; therefore, the emission collected in both TX and X channel is from X emission. At higher excitation powers of 400 μJ/cm^2, (Fig. 8-3) the ratio of PL intensity of TX channel to X/BX channel increases to 1.38%
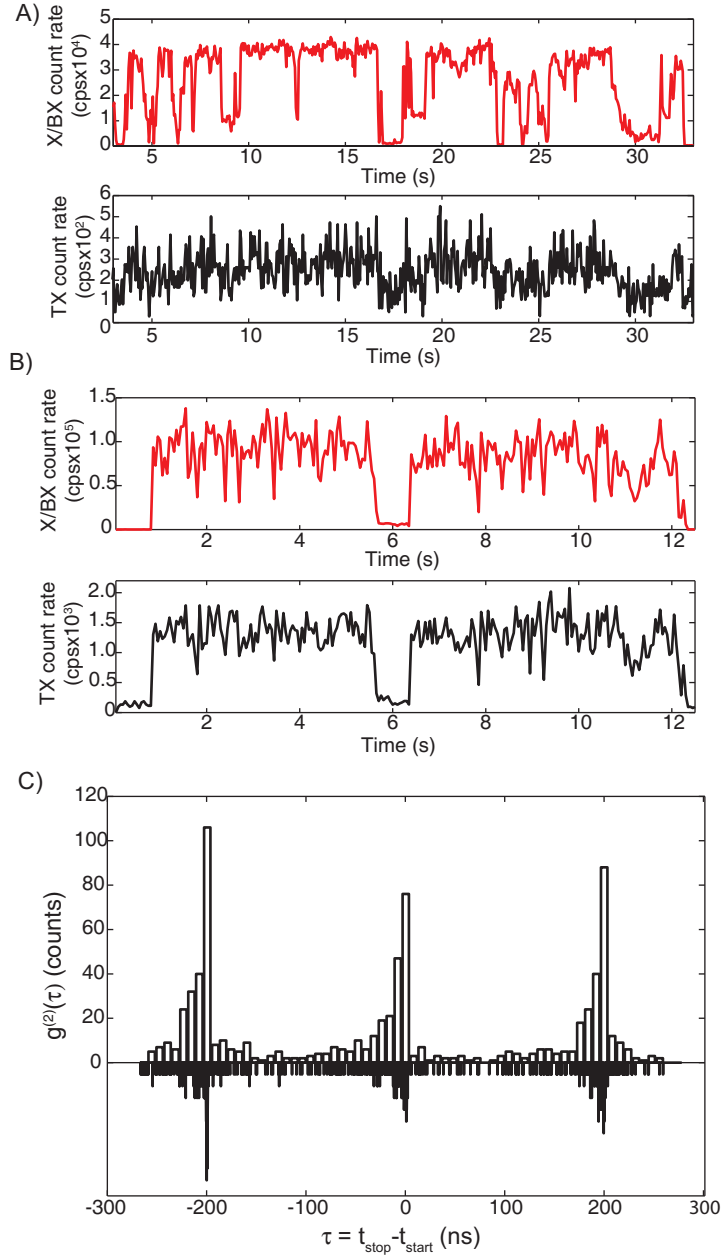
Figure 8-3: (a-b) PL intensities of X/BX (red) and TX (black) channels of a single NC excited at (a) 10 μJ/cm^{-2} and (b) 400 μJ/cm^{-2}. (c) $g^{(2)}(\tau)$ cross-correlation of X/BX and TX channel photons. Figure composed in collaboration with J. Zhao.

from 0.46%, indicating a significant contribution from multiexciton 1P-1P emission. Fig.8-3c shows the $g^{(2)}(\tau)$ cross-correlation histogram of the X and TX channels, measured concurrently with the time traces in Fig.8-3b. The appearance of a large peak at time=0 and the pronounced asymmetry of the peaks are all indications of significant multiexciton character in the TX channel intensity.

From the traces in Fig.8-3b, it is clear that multiexciton emission blinks in a correlated fashion with the band-edge emission intermittency. The correlation between the blinking time traces is not perfect, partly due to spectral diffusion. The TX channel on and off intensities are ≈ 1600 cps and ≈ 50 cps after background subtraction. As is discussed below, we are able to quantitatively estimate that at least 50% of the TX channel signal originates from multiexciton $1P - 1P$ emission. We conclude that multiexciton emission displays on/off intermittency with a contrast ratio greater than 10:1.

8.3.3 Proof of MX emission detection

The principal challenge in the experiment was to detect multiexciton emission from single NCs and quantify how well it has been isolated from the much larger X emission. Three factors complicated the assignment. The most critical is that emission from nanocrystals blue-shift under prolonged excitation in air. The band-edge emission then increasingly leaks through to the TX channel. We overcame this by using short acquisition times, simultaneously monitoring the NC spectrum at all times, and periodically checking the NC's behavior under low fluence to ensure its integrity. The second complication is that NCs under high excitation power blink on faster timescales than our binning times, preventing us from accurately measuring power-dependent signal saturation curves. The third is that the X dynamics of individual NCs tends to steepen at higher fluences, so it is not straightforward to assess MX character from PL decays.

We developed three independent metrics to assess how much of the TX channel signal is due to $1P - 1P$ multiexciton emission that can be applied despite the NC's nonideal properties. Two of them are based on the $g^{(2)}$ correlation data we

simultaneously collect, and another is estimated from time traces.

Trace analysis

As the nanocrystal is subjected to higher excitation powers, both the X and TX channel signals increase but the X channel saturates quickly, while the TX channel signal increases further. This is expected when the TX channel signal is due to multiexciton $1P - 1P$ emission because X emission will saturate when the average number of absorbed photons per pulse becomes greater than ≈ 1, but multiexciton population will continue to grow. If we assume that the spectrum of band-edge emission does not change systematically at higher excitation powers, the intensities of the two channels are related as follows:

$$I_X = I_{\text{band edge}}; \qquad I_{TX} = aI_{\text{band edge}} + I_{1P-1P}$$

At low powers, $\langle N \rangle \to 0$, no multiexcitons are generated and $I_{1P-1P} = 0$. Then:

$$f_{\text{1P-1P}} = \frac{I_{\text{1P-1P}}}{I_{TX}} = \frac{I_{TX}/I_X - (I_{TX}/I_X)_{\langle N \rangle \to 0}}{I_{TX}/I_X} \tag{8.1}$$

Intuitively, any increase in the TX to X channel ratio at higher excitation powers must stem from 1P-1P emission. Application of Eqn. 8.1 to the data in Fig. 8-3 gives an estimated value $f_{\text{1P-1P}} \approx 64\%$.

Estimate from $g_0^{(2)}$

The size of the center peak in the $g^{(2)}(\tau)$ X-TX cross correlation histograms also provides a metric for the TX fraction. If we consider that there are two types of photons, n pertaining to the band edge, and n' from the $1P - 1P$ transition, we find that the relative sizes of the center and side peaks is approximately given by:

$$g_0^{(2)} = \frac{\langle n(n-1) \rangle \theta}{\langle n \rangle (\langle n \rangle \theta + \langle n' \rangle)} + \frac{\langle nn' \rangle}{\langle n \rangle (\langle n \rangle \theta + \langle n' \rangle)} \tag{8.2}$$

where θ is the X rejection ratio, i.e. the ratio of the detection efficiency of band edge to 1P-1P photons in the TX channel. In obtaining this expression we have assumed that the leakage of 1P-1P emission into the X channel is negligible. The first term in Eqn. 8.2 corresponds to a band-edge start and a band-edge photon stopping at the TX detector, while the second corresponds to start and stop from a band-edge and a blue-shifted photon. The latter directly estimates $f_{\text{1P-1P}}$:

$$\frac{\langle nn' \rangle}{\langle n \rangle (\langle n \rangle \theta + \langle n' \rangle)} \approx \frac{\langle n' \rangle}{\langle n \rangle \theta + \langle n' \rangle} = f_{1P-1P} \tag{8.3}$$

where we've assumed that n and n' are not correlated because the electronic states that contribute most of the band edge photons are different from the ones that contribute most of the blue-shifted photons. The first term in Eqn. 8.2 can be shown to approximately estimate $2f_{\text{mx,1S-1S}}$, twice the fraction of the TX channel signal due to leakage from band-edge *multiexciton* emission. Therefore $g_0^{(2)}$ can give an upper and lower bound on $f_{\text{mx, 1S-1S}} + f_{\text{1P-1P}}$, the total multiexciton emission fraction:

$$g_0^{(2)} \approx 2f_{\text{mx,1S-1S}} + f_{\text{1P-1P}} \quad > \quad f_{\text{mx, 1S-1S}} + f_{\text{1P-1P}}$$
$$\frac{g_0^{(2)}}{2} \approx f_{\text{mx,1S-1S}} + \frac{f_{\text{1P-1P}}}{2} \quad < \quad f_{\text{mx, 1S-1S}} + f_{\text{1P-1P}}$$

The interpretation of the first term in Eqn. 8.2 requires the assumption that the X quantum yield is significantly larger than the MX quantum yields, which can break down at the higher excitation powers we use in the TX blinking experiment. Therefore, the $g_0^{(2)}$-based estimate is used mostly as a consistency check. However, this analysis explains why the central peak in $g_0^{(2)}$ is so prominent. For the Fig. 8-3, we estimate that $44\% < f_{\text{1P-1P}} < 88\%$ by this method.

Estimate from $g^{(2)}(\tau)$ asymmetry

When the PL decays of the signals on the two arms of the correlator are different, the resulting $g^{(2)}(\tau)$ will be asymmetric. In fact, the standard way of measuring the

PL decay of the signal in a channel is by replacing the other input with a trigger from the laser. We expect that the TX and X channels will have different PL decays because multiexciton lifetimes are always fast (<1 ns) but the X decay can be slow. This long decay will feature in the TX channel only to the extent that band edge signal is leaking through. We treat the simple case of decays with a fast component (represented by $\delta(t)$) and a single exponential slow component with a lifetime set to 1 :

$$I_{\text{stop}}(t) = \delta(t) + a_x e^{-t}\theta(t); \qquad I_{\text{start}}(t) = \delta(t) + a_{tx}e^{-t}\theta(t)$$

Where the X channel is the stop and the TX channel is the start. We expect $a_{tx} < a_x$. These numbers can be used to quantify the $1P - 1P$ contribution to the TX channel signal by decomposing it as follows:

$$I_{\text{start}}(t) = c_{\text{1P-1P}}\delta(t) + c_{\text{1S-1S}}I_{\text{stop}}$$

because the 1P-1P emission is necessarily fast, and assuming, reasonably, that the dynamics of the band-edge signal that leaks through is the same as that observed in the band-edge channel itself. We've also assumed that the reverse leakage of 1P-1P emission into the band edge channel is negligible. From the decomposition we note $c_{\text{1S-1S}} = a_{tx}/a_x$ and $c_{\text{1P-1P}} = 1 - a_{tx}/a_x$. This gives us an independent assessment of $f_{\text{1P}_e\text{-1P}_h}$:

$$f_{\text{1P}_e\text{-1P}_h} = \frac{c_{\text{1P-1P}}}{\int I_{start}(t)} = \frac{1 - a_{tx}/a_x}{1 + a_{tx}}$$

In our experiment we do not measure a_x and a_{tx} directly, but the information is encoded in the $g^{(2)}(\tau)$ curve. The shape of the side peaks, centered at $\tau_0 = \pm t_{rep}$, can be calculated as follows, where $\tau = \tau' + \tau_0 = t_{\text{start}} - t_{\text{stop}}$:

$$
\begin{aligned}
g^{(2)}(\tau) \quad &\propto \quad \int I_{\text{start}}(t)I_{\text{stop}}(t - \tau')\mathrm{d}t \\
&= \quad \delta(\tau') + a_{tx}e^{-\tau'}\theta(\tau') + a_x e^{\tau'}\theta(-\tau') + \frac{a_x a_{tx}}{2}e^{-|\tau'|} \\
&= \quad \delta(\tau') + a_{tx}\left(1 + \frac{a_x}{2}\right)\theta(\tau')e^{-|\tau'|} + a_x\left(1 + \frac{a_{tx}}{2}\right)\theta(-\tau')e^{-|\tau'|}
\end{aligned}
$$
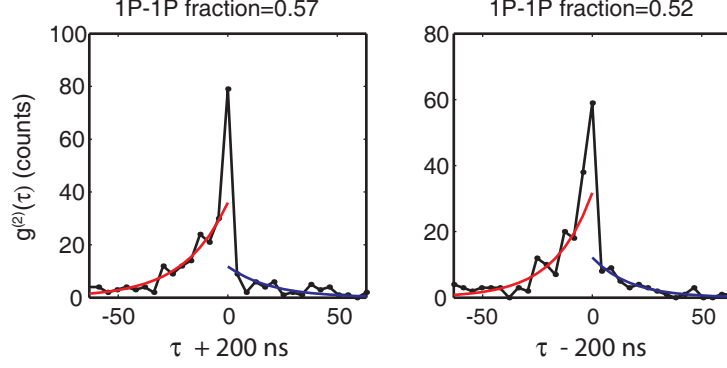
Figure 8-4: Analysis of side peaks in $g^{(2)}(\tau)$ to estimate the fraction of the TX channel signal due to 1P-1P emission

Experimentally we can measure the sizes of the three terms corresponding to $\tau \approx \tau_0$, $\tau < \tau_0$ and $\tau > \tau_0$. Taking the ratio of the integrals of the two slow components to the integral of the fast component at $\tau \approx \tau_0$, we obtain:

$$\alpha_x \equiv \frac{\int_{\tau<\tau_0} g^{(2)}(\tau)}{\int_{\tau\approx\tau_0} g^{(2)}(\tau)} = a_x(1 + a_{tx}/2) \qquad \alpha_{tx} \equiv \frac{\int_{\tau>\tau_0} g^{(2)}(\tau)}{\int_{\tau\approx\tau_0} g^{(2)}(\tau)} = a_{tx}(1 + a_x/2)$$

which are then solved for a_{tx} and a_x. The analysis can be generalized to nonexponential "slow" dynamics by letting a_{tx} and a_x be the ratios of the integrated areas of the long component to the fast component in the PL decays. The estimate of $f_{\text{1P-1P}}$ obtained by the $g^{(2)}$ asymmetry analysis requires only that band-edge dynamics be wavelength-independent, so that its leakage into the TX channel has the same decay shape as that observed in the X channel.

Figure 8-4 shows a detail of the side peaks in the X-TX cross correlation from the data in Fig. 8-3. The $\tau < \tau_0$ and $\tau > \tau_0$ slow components were fit to exponentials with equal lifetimes. The areas of the fitted curves on both sides of the peak origin were then divided by the residual fast component to give α_x and α_{tx}. For this data we find $f_{\text{1P-1P}} \approx 54\%$. This is in good agreement with the $f_{\text{1P-1P}} \approx 64\%$ estimate from time trace intensity analysis. We conclude that, for the data in Fig. 8-3(b,c), at least 50% of the TX channel signal is due to MX 1P-1P emission.

111

8.4 Comparison to Charging model

In the charging model an "off" NC is a singly charged NC, and its low quantum yield is entirely due to Auger recombination. The quantum yield is given by the ratio of the radiative rate to the total decay rate $\eta = k_{rad}/k_{tot}$. By counting the total number of recombination pathways of a CdSe NC, it can be shown that the charged exciton radiative rate is half that of a biexciton $k_{X*}^{rad} = \frac{1}{2}k_{BX}^{rad}$. The total decay rate of both species is dominated by the nonradiative Auger decay, so $k_{tot} \approx k_{nr}$. The nonradiative decay for the charged exciton is denoted by either $k_{X*}^{nr} = k_+$ or $k_{X*}^{nr} = k_-$ depending on whether the extra charge is positive or negative. The BX can decay by promoting either one of the two holes or either of the two electrons to higher kinetic energy states. Importantly, the rates of the hot electron and hot hole pathways are still given by k_+ and k_-, so $k_{BX}^{nr} = 2k_+ + 2k_-$ [17, 100]. Therefore the charged X and neutral BX QYs are related as follows:

$$\frac{\eta_{X*}}{\eta_{BX}} \approx \frac{k_+ + k_-}{k_\pm} \geq 1 \tag{8.4}$$

Where the $\pm$ again depends on the sign of the extra carrier in the charging model off-state. In this picture, the "off" state X cannot have a lower emission quantum yield than that of a biexciton state. This conflicts with our finding (section 8.3.1) that the BX quantum yield is at least ten times larger than the off-state X quantum yield.

In the charging model, the blinking "off" state entails a very specific modification of MX quantum yield. Consider the case of a TX state as shown in Fig. 8-5c, and the presumed "off" state TX, a charged TX*, in Fig. 8-5d. For similar reasons as in the BX/X* comparison, the radiative rate for 1P-1P band emission is twice as large for the charged TX as for the neutral TX. The nonradiative rates can be estimated by noting that $k_{TX}^{nr} < k_{TX*}^{nr} < k_{QX}^{nr}$ where QX denotes the 4e-4h configuration. Assuming that Auger rates scale with the number of possible Auger recombination pathways, the m-multiexciton state should have a rate $k_{mX}^{nr} \propto m^2(m-1)$ [105]. Then, $k_{QX}^{nr}/k_{TX}^{nr} \approx 2.7$. From our ensemble tPL data, we can also derive an experimental upper bound of
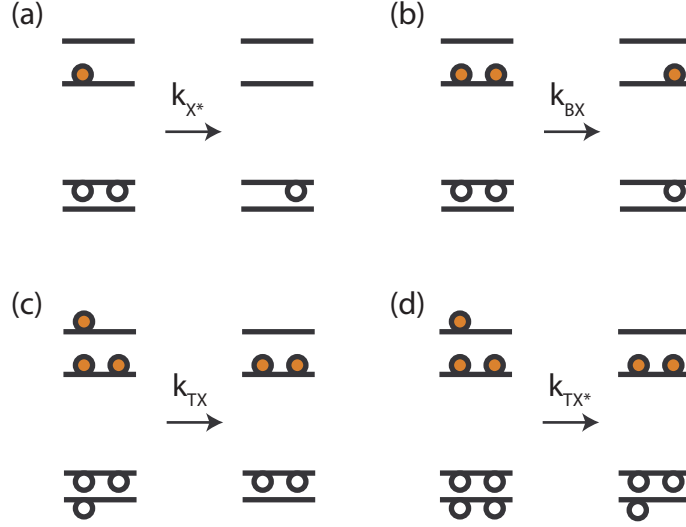
Figure 8-5: Schematics of the various recombination processes of interest for our experiment. (a) Charged exciton ("trion") Auger decay as in the off state of blinking NCs. (b) Neutral biexciton (c) Neutral triexciton (d) Charged triexciton

$k_{QX}^{nr}/k_{TX}^{nr} \approx 3.8$ given by the ratio of fast to slow rates observed in the 1P-1P emission dynamics. This gives us an estimate for the relative quantum yields of on- and off-state TX states:

$$\frac{\eta_{TX^*}}{\eta_{TX}} > 2\frac{k_{TX}^{nr}}{k_{QX}^{nr}} \approx 0.53 \tag{8.5}$$

The ratio is expected to be larger still for the quantum yield ratio of charged and neutral higher multiexcitons (m>3). Therefore, multiexcitonic emission is not expected to show "on"-"off" ratios of more than ≈ 2. As described in section 8.3.2, we find instead a MX on-off ratio of at least 10. This large on-off ratio is difficult to reconcile with the charging model. Combined with the $\eta_X^{off}/\eta_{BX}^{on}$ analysis in the previous section, we reach a general conclusion that the "off" nonradiative decay pathway is too fast to be explained by Auger processes involving just a single additional carrier.

8.5   Towards alternative blinking models

The literature on NC blinking has been dominated by the charging/Auger model to the extent that most work has focused almost exclusively on *how* the NC gets charged

and subsequently neutralized. The off-state quenching mechanism is attributed to the Auger process, which we have shown is incompatible with our data. We propose two directions for new blinking models, shown schematically in Fig. 8-6.

Our findings are inconsistent with the charging model assuming that an "off" NC is singly charged. If the "off" NC instead contains several charges, the Auger mechanism can readily ensure that both $\eta_X^{\mathrm{off}} \ll \eta_{BX}^{\mathrm{on}}$ and $\eta_{MX}^{\mathrm{off}} \ll \eta_{MX}^{\mathrm{off}}$. It is a challenge to obtain digital blinking in such a model because all charges need to be neutralized almost instantaneously when the NC blinks back on. The microscopic model developed by Frantsuzov and Marcus [96] can be extended to allow for charge build-up within an NC, because the NC blinks "off" when a large number of surface states are simultaneously brought into resonance for a specific trapping process. As long as the excitation rate is significantly faster than the trap recombination time τ_{rec}, a large number of electrons can therefore accumulate in the NC volume. When the NC blinks back "on" the trapped holes recombine with the electrons on a timescale τ_{rec}, and the NC fluorescence efficiency fully recovers. Experimentally, such models could be tested by studying single NCs under excitation rates lower than the trap recombination rate. Also, large charge build-up would have a significant effect on the NC's optical absorption spectrum due to state filling.

A class of models that has not received much attention in the literature involve trap-assisted instead of Auger-mediated recombination. Upon absorbing a photon an e-h pair is created in the NC and, in the off state, one of them becomes trapped. Then, before any other photon is absorbed, the remaining free carrier recombines with the trap and the NC returns to a neutral ground state. The "on"-"off" transition would involve switching on and off access to the trap. As long as the trapping rates are sufficiently fast, the model would be consistent with the data presented here. Importantly, our observation of multiexciton emission intermittency indicates that the trapping mechanism must be able to rapidly quench the emission of the multiple e-h pairs generated soon after laser pulse absorption. If the model involves only a single trap, trapped charges must recombine very rapidly. An alternative is that multiple traps become available at once. Generally, microscopic models based on spectral

114
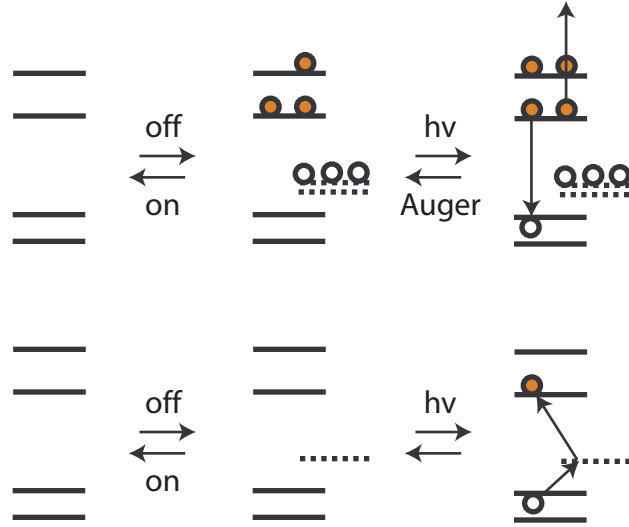
Figure 8-6: Two directions for alternative blinking mechanisms. (top) Multiple-charging. (bottom) Trapping-recombination.

diffusion-controlled access to traps, such as the one proposed by Shimizu et al. [89] and extended by Tang and Marcus [106, 95], could take a trapping-recombination form if the recombination rates are rapid enough.

Chapter 9

Conclusions

At the beginning of this work we set out to quantify Carrier Multiplication in NCs and the role of the Auger process in NC blinking. CM in NCs was found to be weak and consistent with bulk CM, implying no nanoscale enhancement. Similarly, the Auger process, at least in its simplest form, was found too weak to explain experimental blinking phenomenon. We consider here some of the new questions and directions suggested by these observations.

The study of CM has pointed out how little is known about the physics of highly excited carriers in NCs. It will be important to address intraband relaxation both theoretically and experimentally. Some work in that direction has already shown interesting results [74] but extension to the higher energies relevant to CM would be useful. Theoretical studies can elucidate the conditions under which an NC will show bulk-like Coulomb processes and relaxation rates. Lastly, the incorrect results of the early NC CM literature can be attributed ultimately to the difficulty and underdeterminacy inherent to the interpretation of population dynamics data. More direct techniques that could isolate MX and X emission with higher specificity would aid future studies of multiexcitonic states.

Our study of blinking has shown that the charging model is either incomplete or incorrect, and alternatives must be found. Most experiments on blinking have concentrated either on the statistics of the on and off periods or on attempts to externally modify luminescence of an NC. It is difficulty to establish causality because

there are usually several ways that an externally controlled variable could affect PL efficiency, and some of them may be unrelated to the blinking mechanism in the unperturbed system. What is necessary are experiments that inform on the status of a blinking NC as it blinks. A general class of such experiments would involve placing a fluorescent probe near the NC which can be monitored at the same time as the NC fluorescence but is modified by some subset of conceivable physical processes occuring in the NC itself. For example, a polarizable probe could inform on charge separation in the NC via the Stark effect. Alternatively, an energy transfer donor could report on aspects of the NC's absorption spectrum and therefore on electronic state filling in the NC. Combining these ideas with low temperature techniques that maximize the information obtained from experiments could lead to the insights necessary to identify the blinking mechanism.

Ultimately, advances in the understanding of NC photophysics may be catalyzed by the continuing improvement of materials quality and structural characterization techniques. Developing a full structure-function relationship for nanocrystals has remained a challenge because of the difficulty in measuring sub-nanometer details of the NC, especially at the interfaces, and because qualitatively different processes can result in similar features in the most typically studied experimental observables. The effort will continue, motivated by the practically useful qualities of colloidal nanocrystals and the appealing physics of free quantum particles, conveniently packaged into small nanometer-sized jars for scientists to play with.

Appendix A

Radiative rate relationships

A.1 Radiative rates of X and MX in CdSe NCs

CdSe nanocrystals have a two-fold degenerate conduction band and a four-fold degenerate valence band. The conduction band states are spatially the same but have the minimum $S_e = \frac{1}{2}$ spin degeneracy. The bulk valence states have mixed spin and orbital angular momentum $J = L + S = \frac{3}{2}$ resulting from spin-orbit mixing of p-like spatial orbitals ($L = 1$) and $S = \frac{1}{2}$, with the $J = \frac{1}{2}$ representation pushed to much lower energies. In a nanocrystal, the lowest valence states have total angular momentum $J_h = \frac{3}{2}$ including also the orbital motion of the wavefunction envelope. [107]

The lowest electron and hole states are known to mix by lattice and crystal anisotropy as well as the *e-h* exchange interaction and their degeneracy is lifted.[44] However, if we can assume that at room temperature kT is greater than the overall energy splitting all states are approximately equally populated and we can choose the unperturbed $S_e \otimes J = \frac{1}{2} \otimes \frac{3}{2}$ direct product basis to simplify calculations. We will show later that the BX result is independent of any mixing, and will therefore hold at any temperature.

Hole occupation				Recombination with		Total
3/2	1/2	-1/2	-3/2	$m_e = 1/2$	$m_e = -1/2$	rate
1	1	0	0	$1+\frac{2}{3}$	$\frac{1}{3}$	2
1	0	1	0	$1+\frac{1}{3}$	$\frac{2}{3}$	2
1	0	0	1	1	1	2
0	1	1	0	$\frac{2}{3}+\frac{1}{3}$	$\frac{1}{3}+\frac{2}{3}$	2
0	1	0	1	$\frac{2}{3}$	$\frac{1}{3}+1$	2
0	0	1	1	$\frac{1}{3}$	$\frac{2}{3}+1$	2
					Average	2

Table A.1: Squared matrix elements for radiative decay of biexciton configurations in CdSe NCs

The radiative rate of a particular electronic configuration Ψ_i is proportional to:

$$k_i^{rad} \propto \sum_f \left| \langle \Psi_f | \sum_{n,m} \mu_{nm} c_n^\dagger c_m | \Psi_i \rangle \right|^2 = \sum_{\text{occupied states}} |\langle \psi_h | \vec{\mu} | \psi_e \rangle|^2$$

Since the $|\psi_e\rangle$ and $|\psi_h\rangle$ are angular momentum states and $\vec{\mu}$ is a tensor operator, the computation of the possible dipole matrix elements can be conveniently carried out using the Wigner-Eckhart theorem:

$$
\begin{aligned}
| \langle 3/2, m_h | \vec{\mu} | 1/2, m_e \rangle |^2 &= \sum_{q=-1,0,1} \left| \langle 3/2, m_h | \mu_q^{(1)} | 1/2, m_e \rangle \right|^2 \\
&\propto \sum_{q=-1,0,1} |\langle 1/2, m_e; 1, q | 3/2, m_h \rangle|^2
\end{aligned}
$$

where the matrix elements in the last expression are the Clebsch-Gordan coefficients for adding the electron's and the dipole operator's angular momentum to give the hole's angular momentum.

The nonzero matrix elements for recombination with a $m_e = 1/2$ electron are:

$$\left|\left\langle 3/2, 3/2 \left| \mu_1^{(1)} \right| 1/2, 1/2 \right\rangle\right|^2 = k^{rad}$$

$$\left|\left\langle 3/2, 1/2 \left| \mu_0^{(1)} \right| 1/2, 1/2 \right\rangle\right|^2 = \frac{2}{3} k^{rad}$$

$$\left|\left\langle 3/2, -1/2 \left| \mu_{-1}^{(1)} \right| 1/2, 1/2 \right\rangle\right|^2 = \frac{1}{3} k^{rad}$$

Where k^{rad} is some constant. An average over all four hole states therefore gives $k_X^{rad} = k^{rad}/2$. The computation for BX states is shown in table A.1. All configurations have the same radiative rate and $k_{BX}^{rad} = 2k^{rad}$. Therefore, we expect that $k_{BX}^{rad} = 4k_X^{rad}$.

In Chapter 7 we also make use of estimates of the radiative rate of higher multi-excitons. For $m > 2$ states like the TX, we note that in the Chapter 7 study we are concerned chiefly with the band-edge fluorescence, so the radiative rates that apply are the rates of band-edge emission only. Assuming Aufbau configurations at the band edge of 2e-3h and 2e-4h for $m = 3$ and $m \geq 4$, we compute by similar methods that $k_{TX}^{rad} = 3k^{rad}$ and $k_{\geq 4X}^{rad} = 4k^{rad}$.

Proof of BX brightness in CdSe

We show that the BX radiative rate is unaffected by fine structure effects. The results above were obtained using $|\Psi_j^{bx}\rangle$ and $|\Psi_i^x\rangle$ in the occupation number basis derived from the $S_e = \frac{1}{2}$ electron and $J_h = \frac{3}{2}$ hole single particle states. When fine structure effects like e-h coulomb exchange are included, the true eigenstates $|\Psi_\alpha^{bx}\rangle$ and $|\Psi_\beta^x\rangle$ are a superposition of the occupation-number states. The radiative rate of any of the BX states is proportional to:

$$k_{BX,\alpha}^{rad} = \sum_\beta \sum_{m=-1,0,1} |\langle \Psi_\beta^x | \mu_m^{(1)} | \Psi_\alpha^{bx} \rangle|^2 = \sum_{m=-1,0,1} \langle \Psi_\alpha^{bx} | \mu_m^{(1)} P_x \mu_m^{(1)} | \Psi_\alpha^{bx} \rangle$$

Where P_x is the projection operator onto the X subspace. If we choose the occupation number basis to represent $\mu_m^{(1)}$ we note that each of the three matrices $\mu_m^{(1)} P_x \mu_m^{(1)}$ are diagonal because any of the $\mu_m^{(1)}$ connect any of the $|\Psi_i^x\rangle$ to at most one $|\Psi_j^{bx}\rangle$.

Therefore, the matrix $\mu^2 \equiv \sum_m \mu_m^{(1)} P_x \mu_m^{(1)}$ is also diagonal in the $\{|\Psi_j^{bx}\rangle\}$ basis, with all the diagonal elements $= 2k^{rad}$, as discussed previously. Writing $|\Psi_\alpha^{bx}\rangle = \sum c_j |\Psi_j^{bx}\rangle$,

$$k_{BX,\alpha}^{rad} = \sum_{j,j'} c_{j'}^* c_j \langle \Psi_{j'}^{bx} | \mu^2 | \Psi_j^{bx} \rangle = 2k^{rad} \sum_j |c_j|^2 = 2k^{rad}$$

This proves that fine structure effects play little role in BX radiation at any temperature. The result holds as long as the Wigner-Eckart theorem holds (i.e. there is not too much anisotropy) and as long as it is fair to assume that no other higher conduction or valence band states are involved.

A.2   Radiative rate of BX and X in PbSe and PbS

We present here a calculation of k_{BX}^{rad}/k_X^{rad} for a simple model of the lead chalcogenide ground state. The $1S_e$ and $1S_h$ states in lead chalcogenide are eight-fold degenerate. There are four equivalent valleys in the band structure and two-fold spin degeneracy. The possible X electronic configurations can be labeled $i_e m_h$, and the BX configurations $i_e j_e m_h n_h$, where $i, j, m, n \in 1 \dots 8$. Because total momentum and spin must be conserved during an optical interaction, only the recombination of an electron and hole with the same k and same spin is allowed. Assuming that particle momentum and spin remain good quantum numbers, each electron state is connected by a dipole transition to exactly one of the eight hole states. By symmetry, these transition dipole moments all have the same magnitude $|\mu|$. We can then calculate the radiative square transition dipole of each X and BX configuration. In the case of X, there are 8 configurations of type $1_e 1_h$ with $k_{rad} = \mu^2$, and $8 \cdot 7$ of type $1_e 2_h$ with $k_{rad} = 0$. Similarly, for the BX, there are $\binom{8}{2}$ configurations like $1_e 2_e 1_h 2_h$ with $k_{rad} = \mu^2 + \mu^2$, $8 \cdot 7 \cdot 6$ configurations of type $1_e 2_e 1_h 3_h$ with $k_{rad} = \mu^2$, and $\binom{8}{2}\binom{6}{2}$ dark $1_e 2_e 3_h 4_h$-type states. Averaging over all the available configurations, one finds $k_X^{rad} = \mu^2/8$ and $k_{BX}^{rad} = \mu^2/2$, and therefore $k_{BX}^{rad} = 4k_X^{rad}$. This result should remain approximately valid even in the presence of perturbations that mix states with different quantum numbers or couple the electrons and holes, as long as the width of the resulting energy

fine structure is sufficiently smaller than the available thermal energy, kT.

Appendix B

Analytical expressions for $g^{(2)}(t)$

B.1   Relationship between n and $g_0^{(2)}$

In this section we derive a relationship between measured correlation histograms and the underlying statistics of photon emission. We can begin the calculation at the first pulse *after* the correlator card has finished a single recording. This source emission pulse contains n photons with probability $p(n)$. There are a number of possibilities:

1. Start and stop occur during this pulse. Stop can actually occur slightly before start because the cabling was set up to allow recording of negative start-stop times.

2. Start occurs during this pulse. Stop does not occur in this pulse.

3. Stop occurs during this pulse but start does not.

Option 1 leads to a count at the center peak. If option 2 occurs *and* a stop pulse is detected at the next pulse, there will be a count at the side peak. Option 3 can only lead to counts at negative-time peaks, and does not need to be treated further.

The probability of start and stop occuring during the same n-photon pulse is the probability that at least one photon is detected at the start APD and at least one photon is detected at the stop APD. Let N_α and N_β be random variables representing

the number of photons detected at the start and the stop.

$$
\begin{aligned}
P_n(center) &= P(N_\alpha \geq 1 \,\&\, N_\beta \geq 1) \\
&= 1 - P(N_\alpha = 0 \,\text{or}\, N_\beta = 0) \\
&= 1 - P(N_\alpha = 0) - P(N_\beta = 0) + P(N_\alpha = 0 \,\&\, N_\beta = 0) \\
&= 1 - (1 - \alpha)^n - (1 - \beta)^n + (1 - \alpha - \beta)^n
\end{aligned}
$$

Now for the side peak. The probability of start occuring at the n-photon pulse and the stop occuring at the next is the probability that at least one photon is detected at the start APD and *no* photon is detected at the stop multiplied by the probability that at least one photon is detected at the stop APD *at the next pulse*. Let P_β equal this last probability. Then:

$$
\begin{aligned}
P_n(side) &= P(N_\alpha \geq 1 \,\&\, N_\beta = 0)P_\beta \\
&= [P(N_\beta = 0) - P(N_\alpha = 0 \,\&\, N_\beta = 0)]\, P_\beta \\
&= [(1 - \beta)^n - (1 - \alpha - \beta)^n]\, P_\beta
\end{aligned}
$$

where
$$
P_\beta = \sum_{m=0}^{\infty} p(m)P(N_\beta \geq 1) = \sum_{m=0}^{\infty} p(m)\left[1 - (1 - \beta)^m\right]
$$

By adding the contributions from all possible values of n weighted by their probabilities, we get the total intensities at the center and the side peak:

$$
\begin{aligned}
center &= \sum p(n)P_n(center) \\
&= \sum p(n)\left[1 - (1 - \alpha)^n - (1 - \beta)^n + (1 - \alpha - \beta)^n\right] \\
side &= \sum p(n)P_n(side) \\
&= \sum p(n)\left[(1 - \beta)^n - (1 - \alpha - \beta)^n\right] P_\beta
\end{aligned}
$$

126

B.1.1 Low detection efficiency limit

The expressions are simplified in the limit where α and β are small, typical of most experiments.

$$1 - (1-\alpha)^n - (1-\beta)^n + (1-\alpha-\beta)^n \approx n(n-1)\alpha\beta$$
$$(1-\beta)^n - (1-\alpha-\beta)^n \approx n\alpha$$
$$1 - (1-\beta)^m \approx m\beta \tag{B.1}$$

The center and side peak intensities become:

$$center = \alpha\beta \sum_n n(n-1)p(n) \qquad side = \alpha\beta \sum_n np(n) \sum_m mp(m)$$

And the ratio is therefore:

$$
\begin{aligned}
g_0^{(2)} \equiv \frac{center}{side} &= \left(\sum_{n=2}^{\infty} n(n-1)p(n) \right) \Big/ \left(\sum_{n=1}^{\infty} np(n) \right)^2 = \frac{\langle n(n-1) \rangle}{\langle n \rangle^2} \\
&= \frac{2p(2) + 6p(3) + \ldots}{(p(1) + 2p(2) + 3p(3) + \ldots)^2}
\end{aligned}
$$

If the probability distribution of n change over time, as in the case of nanocrystal blinking, the histogrammed counts at the center and side peaks are still accumulated separately, so that:

$$center = \alpha\beta \left\langle \sum_n n(n-1)p(n,t) \right\rangle_t \qquad side = \alpha\beta \left\langle \left(\sum_n np(n,t) \right)^2 \right\rangle_t$$

Therefore,
$$g_0^{(2)} = \frac{\langle\langle n(n-1)\rangle\rangle_t}{\langle\langle n\rangle^2\rangle_t} \tag{B.2}$$

where $\langle \cdot \rangle_t$ denote time averages.

B.2 Nanocrystal emission

A colloidal NC can absorb a random number N of photons from the excitation pulse. Each step in the resulting N-length recombination cascade can occur radiatively or nonradiatively. ξ_m is a random variable that takes the value 1 if the m-th multiexcitonic state decay is radiative, 0 otherwise. Then, the emitted photon number from an NC is given by:

$$n_{\text{dot}} = \sum_m \xi_m I_{N \geq m}$$

Where $I_{N \geq m}$ is an indicator variable equal to 1 if $N \geq m$. We compute the random variable in the numerator of $g_0^{(2)}$:

$$n_{\text{dot}}(n_{\text{dot}} - 1) = 2 \sum_m I_{N \geq m} \sum_{m' < m} \xi_m \xi_{m'}$$

Where we have made use of the fact that $I_{N \geq m} I_{N \geq m'} = I_{N \geq m}$ when $m \geq m'$ and that $\xi_m^2 = \xi_m$. Taking expectation values:

$$g_0^{(2)} = \frac{\langle n_{\text{dot}}(n_{\text{dot}} - 1) \rangle}{\langle n_{\text{dot}} \rangle^2} = \frac{2 \sum_m P_{N \geq m} \sum_{m' < m} \langle \xi_m \xi_{m'} \rangle}{\left(\sum_m P_{N \geq m} \langle \xi_m \rangle \right)^2}$$

Here $P_{N \geq m}$ is the probability that at least m photons are absorbed by the NC. In our experiments the excitation wavelength is well above the exciton energy so the absorption process can be treated as Poissonian, with $P_{N=m} = \frac{\langle N \rangle^m}{m!} \exp(-\langle N \rangle)$. In the limit of low power,

$$\lim_{\langle N \rangle \to 0} g_0^{(2)} = \lim_{\langle N \rangle \to 0} \frac{2 P_{N \geq 2} \langle \xi_2 \xi_1 \rangle}{P_{N \geq 1}^2 \langle \xi_1 \rangle^2} = \frac{\langle \xi_2 \xi_1 \rangle}{\langle \xi_1 \rangle^2}$$

Which is the key result used in the paper. If the NC blinks, we apply Eqn. B.2, to obtain:

$$\lim_{\langle N \rangle \to 0} g_0^{(2)} = \frac{\langle \langle \xi_2 \xi_1 \rangle \rangle_t}{\langle \langle \xi_1 \rangle^2 \rangle_t} = \frac{\langle \eta_x(t) \eta_{bx}(t) \rangle_t}{\langle \eta_x(t)^2 \rangle_t}$$

Where $\eta_x(t)$ and $\eta_{bx}(t)$ are the time-varying X and BX quantum yields. The power dependence at low power can be obtained by expansion, keeping terms up to order

$\langle N \rangle^3$ in the numerator and denominator:

$$g_0^{(2)} \approx \frac{\langle \xi_1 \xi_2 \rangle}{\langle \xi_1 \rangle^2} \left[1 + \frac{\langle N \rangle}{3} - \frac{\langle \xi_2 \rangle}{\langle \xi_1 \rangle} \langle N \rangle \right] + \left(\frac{\langle \xi_3 \xi_1 \rangle}{\langle \xi_1 \rangle^2} + \frac{\langle \xi_3 \xi_2 \rangle}{\langle \xi_1 \rangle^2} \right) \frac{\langle N \rangle}{3}$$

B.3 Estimates of multiexciton quantum yields

In Chapter 7 we computed the evolution of $g_0^{(2)}$ for an NC using a simple model to estimate the multiexciton quantum efficiencies $\eta_m = \langle \phi_m \rangle$ from an assumed value of $\eta_2 = \eta_{bx}$. We note that $\eta_m = k_m^{rad} \tau_m$. We assume that the multiexciton lifetimes are dominated by the Auger mechanism. By counting the number of possible trion recombination pathways and assuming every trion's recombination occurs with the same rate, one finds that the Auger rate for multiexcitons scales as $k_m \propto m^2(m-1)$.

Radiative rates for band edge emission in CdSe have been estimated in Appendix A.1. We found that $k_{BX}^{rad} = 2k^{rad}$, $k_{TX}^{rad} = 3k^{rad}$ and $k_{\geq 4X}^{rad} = 4k^{rad}$, where k^{rad} is a constant. Combining this with the Auger rate scaling, we can estimate the band-edge emission quantum yields of all higher multiexcitons from the biexciton QY:

$$\eta_m \approx \frac{2\min(m, 4)}{m^2(m-1)} \eta_{bx} \tag{B.3}$$

B.4 Background effects

The results calculated in B.1 can be extended to the case where there are two types of photons. $n = n_{\text{dot}}$ is the photon number from the source of interest and n' is a background source, which has detection probabilities α' and β'. Then,

$$
\begin{aligned}
center &= \sum p_{nn'} \left[n(n-1)\alpha\beta + n'(n'-1)\alpha'\beta' + nn'(\alpha\beta' + \alpha'\beta) \right] \\
side &= \sum p_{nn'}(n\alpha + n'\alpha') \sum p_{nn'}(n\beta + n'\beta')
\end{aligned}
$$

and

$$g_0^{(2)} = \frac{\alpha\beta\langle n(n-1)\rangle + \alpha'\beta'\langle n'(n'-1)\rangle + \langle nn'\rangle(\alpha\beta' + \alpha'\beta)}{(\langle n\rangle\alpha + \langle n'\rangle\alpha')(\langle n\rangle\beta + \langle n'\rangle\beta')}$$

We use the facts that $\langle n(n-1)\rangle = g_{0\ \text{dot}}^{(2)}\langle n\rangle^2$ and $\langle n'(n'-1)\rangle = g_{0\ \text{backg}}^{(2)}\langle n\rangle^2$ and assume that n and n' are independant. The fraction of the signal from the extra source in channel 1 is given by $y_1 = \frac{\alpha'\langle n'\rangle}{\alpha\langle n\rangle + \alpha'\langle n'\rangle}$ and similarly for y_2. Thus, we find:

$$g_0^{(2)} = (1-y_1)(1-y_2)g_{0\ \text{dot}}^{(2)} + y_1 y_2 g_{0\ \text{backg}}^{(2)} + (1-y_1)y_2 + (1-y_2)y_1 \tag{B.4}$$

For the case where n' is simply a Poissonian background, as would be the case for laser scatter, etc., then $g_{0\ \text{backg}}^{(2)} = 1$ and we obtain:

$$g_0^{(2)} = 1 + (1-\mathfrak{b}_1)(1-\mathfrak{b}_2)\left[g_{0\ \text{dot}}^{(2)} - 1\right] \tag{B.5}$$

Where $\mathfrak{b}_{(1,2)} = y_{1,2}$ are the background to total signal ratios. If instead n' is due to another NC, which we assume for simplicity has an identical $g_{0\ \text{backg}}^{(2)} = g_{0\ \text{dot}}^{(2)}$, then we obtain:

$$g_0^{(2)} = g_{0\ \text{dot}}^{(2)} + (x_1 y_2 + x_2 y_1)\left[1 - g_{0\ \text{dot}}^{(2)}\right] \tag{B.6}$$

where $x_{1,2} = 1 - y_{1,2}$ and $y_{1,2}$ are the signal fractions of the dot of interest and the additional NC in each channel.

B.5   CW antibunching

B.5.1   Population dynamics

Consider the three level system formed by ground, exciton and biexciton states. The photon absorption rate is γ and the decay rates of X and BX are k_x and k_{bx} respectively. Then:

$$\frac{\mathrm{d}}{\mathrm{d}t}\begin{bmatrix} \sigma_2 \\ \sigma_1 \\ \sigma_0 \end{bmatrix} = \begin{bmatrix} -k_{bx} & \gamma & 0 \\ k_{bx} & -\gamma - k_x & \gamma \\ 0 & k_x & -\gamma \end{bmatrix} \begin{bmatrix} \sigma_2 \\ \sigma_1 \\ \sigma_0 \end{bmatrix}$$

The system has three eigenvalues, the first of which corresponds to equilibrium:

$$\lambda_0 = 0 \quad \boldsymbol{\sigma}_{eq} = \frac{1}{k_x + \gamma + \gamma^2/k_{bx}} \begin{bmatrix} \gamma^2/k_{bx} \\ \gamma \\ k_x \end{bmatrix}$$

The other two eigenvalues are:

$$\lambda_{\pm} = -\frac{k_x + k_{bx} + 2\gamma \pm \sqrt{(k_{bx} - k_x)^2 + 4\gamma k_x}}{2}$$

which in the limit of $\gamma \ll |k_{bx} - k_x|$ are approximately $\lambda_+ \approx -k_{bx}$ and $\lambda_- \approx -k_x$ for the usual case where $k_{bx} > k_x$.

The related eigenvectors do not have a simple form in the general case, so we approach the problem numerically, and write formal solutions as follows:

$$\boldsymbol{\sigma}(t) = \exp{(\mathbf{A}t)}\boldsymbol{\sigma}(0)$$

where $\mathbf{A}$ is the matrix of rate constants that specifies the dynamics.

B.5.2 Cross-correlation calculation

The measured photon cross-correlation $g^{(2)}(t)$ is proportional to the probability density of detecting a photon at time t given that a photon has been detected at time 0. If photons can be attributed to various sources like X or BX emission or even background, $g^{(2)}(t)$ can be decomposed as follows:

$$
\begin{aligned}
g^{(2)}(t) \quad &\propto \quad P(\text{detect } h\nu \text{ at } t|\text{detect } h\nu \text{ at } 0)\\
&= \quad P(h\nu \text{ at } t|\text{X } h\nu \text{ at } 0) \times \frac{I_X}{I_{total}}\\
&\quad + P(h\nu \text{ at } t|\text{BX } h\nu \text{ at } 0) \times \frac{I_{BX}}{I_{total}}\\
&\quad + P(h\nu \text{ at } t|\text{noise } h\nu \text{ at } 0) \times \frac{I_{backg}}{I_{total}}
\end{aligned}
$$

Each one of the possible t=0 events prepares the system in a particular state. If an X photon is detected, the system is in the ground state, while if a background photon is detected, the system remains at steady state. The light intensity is described by:

$$
I(t) = \begin{bmatrix} \eta_{bx} k_{bx} & \eta_x k_x & 0 \end{bmatrix} \cdot \boldsymbol{\sigma}(t) + I_{backg}
$$

Where η_{bx} and η_x are proportional to the BX and X quantum yields and other factors like detection efficiency. At steady state $\boldsymbol{\sigma}(t) = \boldsymbol{\sigma}_{eq}$:

$$
I_{total} = \underbrace{\frac{\eta_{bx}\gamma^2}{k_x + \gamma + \gamma^2/k_{bx}}}_{I_{BX}} + \underbrace{\frac{\eta_x k_x \gamma}{k_x + \gamma + \gamma^2/k_{bx}}}_{I_X} + I_{backg}
$$

Therefore:

$$
\begin{aligned}
g^{(2)}(t) \quad &\propto \quad I_{BX} \begin{bmatrix} \eta_{bx} k_{bx} & \eta_x k_x & 0 \end{bmatrix} \cdot \exp\left(\mathbf{A}t\right) \begin{bmatrix} 0 \\ 1 \\ 0 \end{bmatrix}\\
&\quad + I_X \begin{bmatrix} \eta_{bx} k_{bx} & \eta_x k_x & 0 \end{bmatrix} \cdot \exp\left(\mathbf{A}t\right) \begin{bmatrix} 0 \\ 0 \\ 1 \end{bmatrix}\\
&\quad + I_{backg}^2 + 2I_{backg}(I_X + I_{BX})
\end{aligned}
$$

For proper normalization the expression above can be divided by value at infinity
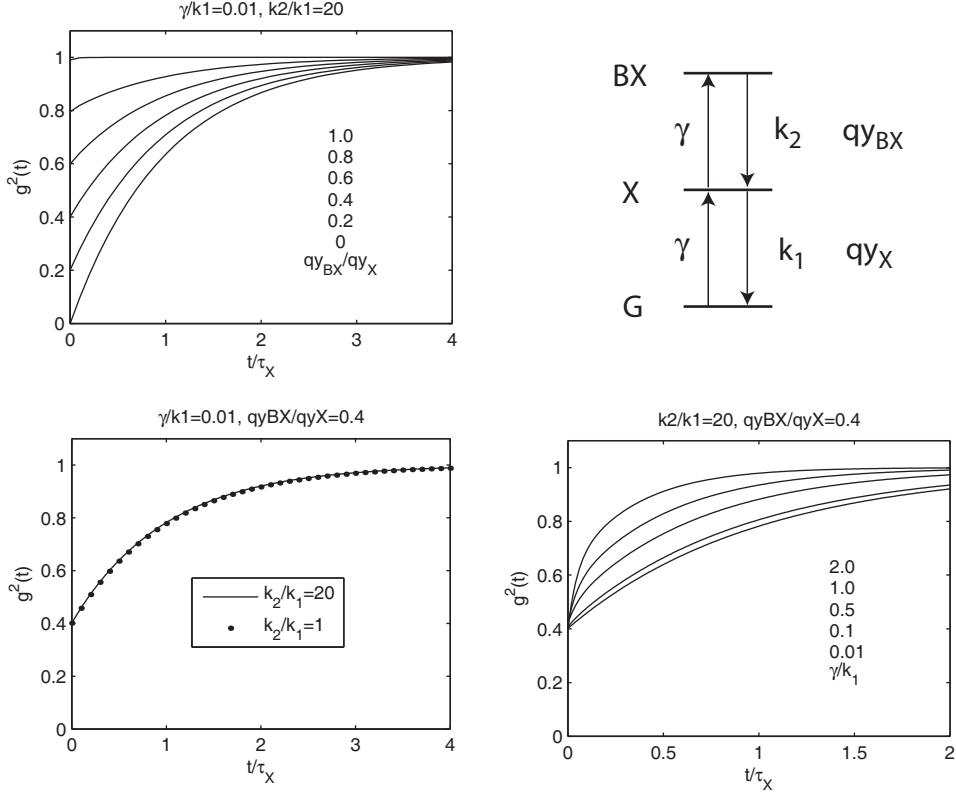
Figure B-1: Calculated normalized $g^{(2)}(t)$ using expressions shown in text for various cases of interest and a schematic of the states and rate constants involved. Background counts are assumed to be negligible.

$$g^{(2)}(\infty) = (I_X + I_{BX} + I_{backg})^2.$$

B.5.3   Numerical results

The figure shows numerical results for some cases relevant to nanocrystal antibunching studies, as well as some to illustrate the effects of various parameters on the normalized $g^{(2)}$. We find, most importantly, that the antibunching dip at $t = 0$ reduces as the BX quantum yield approaches that of the X. In particular, the correlation at $t = 0$ is approximately η_{bx}/η_x irrespective of the values of k_{bx} and k_x. We also see that $g^{(2)}$ is independent of the pump absorption rate except when it becomes comparable to k_x at which point its main effect is to speed up the return to steady state without significantly affecting the magnitude of the $t = 0$ dip.

B.5.4 Analytical expressions for $g^{(2)}(0)$

A normalized expression for $g^{(2)}(0)$ can be obtained from the $g^{(2)}(t)$ expression above.

$$g^{(2)}(0) = \frac{I_{BX}\eta_x k_x + I_{backg}^2 + 2I_{backg}(I_X + I_{BX})}{(I_X + I_{BX} + I_{backg})^2}$$

In the ideal case of no background:

$$g_{id}^{(2)}(0) = \frac{\eta_{bx}}{\eta_x} \times \frac{1 + \frac{\gamma}{k_x} + \frac{\gamma^2}{k_{bx}k_x}}{\left(1 + \frac{\gamma}{k_x}\frac{\eta_{bx}}{\eta_x}\right)^2} \approx \frac{\eta_{bx}}{\eta_x} \text{ for } \gamma \ll k_x$$

For the general case, we can write $I_{BX}\eta_x k_x = g_{id}^{(2)}(0)(I_X + I_{BX})^2$ and obtain:

$$g^{(2)}(0) = 1 - \frac{1 - g_{id}^{(2)}(0)}{(1 + I_{backg}/I_{signal})^2} \approx g_{id}^{(2)}(0)\left(1 - 2\frac{I_{backg}}{I_{signal}}\right) + 2\frac{I_{backg}}{I_{signal}}$$

In these expressions $I_{signal} = I_X + I_{BX}$. This shows that the experimental anti-bunching dip is a good indicator of η_{bx}/η_x as long as the background to signal ratio is much smaller than the quantum yield ratio. Alternatively, if the signal to background ratio is known, the above expressions allow direct determination of η_{bx}/η_x from the measured $g^{(2)}(0)$.

Bibliography

[1] V.I. Colvin, M.C. Schlamp, and A.P. Alivisatos. Light-emitting-diodes made from cadmium selenide nanocrystals and a semiconducting polymer. *Nature*, 370(6488):354–357, 1994.

[2] S. Coe-Sullivan, W.K. Woo, J.S. Steckel, M. G. Bawendi, and V. Bulovic. Electroluminescence from single monolayers of nanocrystals in molecular organic devices. *Nature*, 420:800–803, 2002.

[3] D. C. Oertel, M. G. Bawendi, A. C. Arango, and V. Bulovic. Photodetectors based on treated cdse quantum-dot films. *Appl. Phys. Lett.*, 87:213505, 2005.

[4] V. Sundar, H. J. Eisler, T. Deng, Y. Chan, E. L. Thomas, and M. G. Bawendi. Soft-lithographically embossed, multilayered distributed-feedback nanocrystal lasers. *Adv. Mater.*, 16(23-24):2137–2141, 2004.

[5] Y. Chan, J-M. Caruge, P.T. Snee, and M. G. Bawendi. Multiexcitonic two-state lasing in a cdse nanocrystal laser. *Appl. Phys. Lett.*, 85(13):2460–2462, 2004.

[6] X. Brokmann, E. Giacobino, M. Dahan, and J. P. Hermier. Highly efficient triggered emission of single photons by colloidal cdse/zns nanocrystals. *Appl. Phys. Lett.*, 85:712–714, 2004.

[7] B. R. Fisher, J-M. Caruge, D. Zehnder, and M. G. Bawendi. Room-temperature ordered photon emission from multiexciton states in single cdse core-shell nanocrystals. *Phys. Rev. Lett.*, 94:087403, 2005.

[8] V. I. Klimov, A. A. Mikhailovsky, S. Xu, A. Malko, J.A. Hollingsworth, C. A. Leatherdale, H. J. Eisler, and M. G. Bawendi. Optical gain and stimulated emission in nanocrystal quantum dots. *Science*, 290:314–317, 2000.

[9] J-M. Caruge, Y. Chan, V. Sundar, H. J. Eisler, and M. G. Bawendi. Transient photoluminescence and simultaneous amplified spontaneous emission from multiexciton states in cdse quantum dots. *Phys. Rev. B*, 70:085316, 2004.

[10] M. Nirmal, B. O. Dabbousi, M. G. Bawendi, J. J. Macklin, J. K. Trautman, T. D. Harris, and L. E. Brus. Fluorescence intermittency in single cadmium selenide nanocrystals. *Nature*, 383(6603):802–804, 1996.

[11] C. B. Murray, D. J. Norris, and M. G. Bawendi. Synthesis and characterization of nearly monodisperse cde(e=sulfur, selenium, tellurium) semiconductor nanocrystallites. *J. Am. Chem. Soc.*, 115:8706–8715, 1993.

[12] M. A. Hines and G. D. Scholes. Colloidal pbs nanocrystals with size-tunable near-infrared emission: Observation of post-synthesis self-narrowing of the particle size distribution. *Advanced Materials*, 15:1844–1849, 2003.

[13] N. W. Ashcroft and N. D. Mermin. *Solid State Physics*. Saunders College Publishing, 1976.

[14] V. I. Klimov, A. A. Mikhailovsky, D. W. McBranch, C. A. Leatherdale, and M. G. Bawendi. Quantization of multiparticle auger rates in semiconductor quantum dots. *Science*, 287(5455):1011–1013, 2000.

[15] M. Achermann, J.A. Hollingsworth, and V. I. Klimov. Multiexcitons confined within a subexcitonic volume: Spectroscopic and dynamical signatures of neutral and charged biexcitons in ultrasmall semiconductor nanocrystals. *Phys. Rev. B*, 68:245302, 2003.

[16] Al. L. Efros, D. J. Lockwood, and L. Tsybeskov. *Semiconductor nanocrystals, from basic principles to applications*. Kluwer Academic, 2003.

[17] L.-W. Wang, M. Califano, A. Zunger, and A. Franceschetti. Pseudopotential theory of auger processes in cdse quantum dots. *Phys. Rev. Lett.*, 91(5):056404, 2003.

[18] I. Robel, R. Gresback, U. Kortshagen, R. D. Schaller, and V. I. Klimov. Universal size-dependent trend in auger recombination in direct-gap and indirect-gap semiconductor nanocrystals. *Physical Review Letters*, 102:177404, 2009.

[19] Al. L. Efros. Random telegraph signal in the photoluminescence intensity of single quantum dot. *Phys. Rev. Lett.*, 78(6):1110, 1997.

[20] M. Wolf, R. Brendel, J. H. Werner, and H. J. Queisser. Solar cell efficiency and carrier multiplication in si1-xgex alloys. *J. Appl. Phys.*, 83(8):4213–4221, 1998.

[21] D. Harrison, R. A. Abram, and S. Brand. Characteristics of impact ionization rates in direct and indirect gap semiconductors. *J. Appl. Phys.*, 85(12):8186–8192, 1999.

[22] W. Shockley and H. J. Queisser. Detailed balance limit of efficiency of p-n junction solar cells. *J. Appl. Phys.*, 32(3):510–519, 1961.

[23] V. I. Klimov. Detailed-balance power conversion limits of nanocrystal-quantum-dot solar cells in the presence of carrier multiplication. *Appl. Phys. Lett.*, 89:123118, 2006.

[24] A. J. Nozik. Spectroscopy and hot electron relaxation dynamics in semiconductor quantum wells and quantum dots. *Annu. Rev. Phys. Chem.*, 52:193–231, 2001.

[25] D.I. Chepic, Al. L. Efros, A.I. Ekimov, M.G. Ivanov, V.A. Kharchenko, I.A. Kudriavtsev, and T.V. Yazeva. Auger ionization of semiconductor quantum drops in a glass matrix. *J. Lumin.*, 47(3):113–127, 1990.

[26] R. D. Schaller and V. I. Klimov. High efficiency carrier multiplication in pbse nanocrystals: Implications for solar energy conversion. *Phys. Rev. Lett.*, 92:186601, 2004.

[27] R. J. Ellingson, M. C. Beard, J. C. Johnson, P. Yu, O. I. Micic, A. J. Nozik, A. Shabaev, and Al. L. Efros. Highly efficient multiple exciton generation in colloidal pbse and pbs quantum dots. *Nano Lett.*, 5:865, 2005.

[28] R. D. Schaller, M. Sykora, J. M. Pietryga, and V. I. Klimov. Seven excitons at a cost of one: Redefining the limits for conversion efficiency of photons into charge carriers. *Nano Lett.*, 6(3):424–429, 2006.

[29] M. C. Beard, K. P. Knutsen, P. Yu, J. M. Luther, Q. Song, W. K. Metzger, R. J. Ellingson, and A. J. Nozik. Multiple exciton generation in colloidal silicon nanocrystals. *Nano Lett.*, 7:2506–2512, 2007.

[30] R. D. Schaller, M.A. Petruska, and V. I. Klimov. Effect of electronic structure on carrier multiplication efficiency: Comparative study of pbse and cdse nanocrystals. *Appl. Phys. Lett.*, 87:253102, 2005.

[31] R. D. Schaller, M. A. Petruska, and V. I. Klimov. Tunable near-infrared optical gain and amplified spontaneous emission using pbse nanocrystals. *J. Phys. Chem. B*, 107(50):13765–13768, 2003.

[32] J. J. H. Pijpers, E. Hendry, M. T. W. Milder, R. Fanciulli, J. Savolainen, J. L. Herek, D. Vanmaekelbergh, S. Ruhman, D. Mocatta, D. Oron, A. Aharoni, U. Banin, and M. Bonn. Carrier multiplication and its reduction by photodoping in colloidal inas quantum dots. *J. Phys. Chem. C.*, 111:4146–4152, 2007.

[33] R. D. Schaller, J. M. Pietryga, and V. I. Klimov. Carrier multiplication in inas nanocrysta quantum dots with an onset defined by the energy conservation limit. *Nano Lett.*, 7:3469–3476, 2007.

[34] J. M. Luther, M. C. Beard, Q. Song, M. Law, R. J. Ellingson, and A. J. Nozik. Multiple exciton generation in films of electronically coupled pbse quantum dots. *Nano Lett.*, 7:1779–1784, 2007.

[35] P. Guyot-Sionnest, B. L. Wehrenberg, and D. Yu. Intraband relaxation in cdse nanocrystals and the strong influence of the surface ligands. *J. Chem. Phys.*, 123:074709, 2005.

[36] B. L. Wehrenberg, C. J. Wang, and P. Guyot-Sionnest. Interband and intraband optical studies of pbse colloidal quantum dots. *J. Phys. Chem. B*, 106(41):10634–10640, 2002.

[37] J. M. Harbold, H. Du, T. D. Krauss, K. S. Cho, C. B. Murray, and F. W. Wise. Time-resolved intraband relaxation of strongly confined electrons and holes in colloidal pbse nanocrystals. *Phys. Rev. B*, 72(19):195312, 2005.

[38] B. Lounis, H.A. Bechtel, D. Gerion, P. Alivisatos, and W. E. Moerner. Photon antibunching in single cdse/zns quantum dot fluorescence. *Chem. Phys. Lett.*, 329:399–404, 2000.

[39] X. Brokmann, L. Coolen, M. Dahan, and J.-P. Hermier. Measurement of the radiative and nonradiative decay rates of single cdse nanocrystals through a controlled modification of their spontaneous emission. *Phys. Rev. Lett.*, 93:107403, 2004.

[40] B. R. Fisher, H. J. Eisler, N. E. Stott, and M. G. Bawendi. Emission intensity dependence and single-exponential behavior in single colloidal quantum dot fluorescence lifetimes. *J. Phys. Chem. B*, 108(1):143–148, 2004.

[41] G. Kalyuzhny and R. W. Murray. Ligand effects on optical properties of cdse nanocrystals. *J. Phys. Chem. B*, 109:7012–7021, 2005.

[42] C. A. Leatherdale, W. K. Woo, F. V. Mikulec, and M. G. Bawendi. On the absorption cross section of cdse nanocrystal quantum dots. *J. Phys. Chem. B*, 106(31):7619–7622, 2002.

[43] G. Nair and M. G. Bawendi. Carrier multiplication yields of cdse and cdte nanocrystals by transient photoluminescence spectroscopy. *Physical Review B*, 76:081304(R), 2007.

[44] A. L. Efros, M. Rosen, M. Kuno, M. Nirmal, D. J. Norris, and M. Bawendi. Band-edge exciton in quantum dots of semiconductors with a degenerate valence band: Dark and bright exciton states. *Phys. Rev. B*, 54(7):4843–4856, 1996.

[45] M. Nirmal, D. J. Norris, M. Kuno, M. G. Bawendi, A. L. Efros, and M. Rosen. Observation of the "dark exciton" in cdse quantum dots. *Phys. Rev. Lett.*, 75(20):3728–3731, 1995.

[46] J. Shumway, A. Franceschetti, and A. Zunger. Correlation versus mean-field contributions to excitons, multiexcitons, and charging energies in semiconductor quantum dots. *Phys. Rev. B*, 63:155316, 2001.

[47] P.T. Snee, Y. Chan, D. G. Nocera, and M. G. Bawendi. Whispering-gallery-mode lasing from a semiconductor nanocrystal/microsphere resonator composite. *Adv. Mater.*, 17:1131–1136, 2005.

[48] B. L. Sowers, M. W. Williams, R. N. Hamm, and E. T. Arakawa. Optical properties of liquid carbon tetracholoride, n-hexane, and cyclohexane in the vacuum ultraviolet. *J. Chem. Phys.*, 57:167–170, 1972.

[49] R. D. Schaller, M. Sykora, S. Jeong, and V. I. Klimov. High-efficiency carrier multiplication and ultrafast charge separation in semiconductor nanocrystals studied via time-resolved photoluminescence. *J. Phys. Chem. B*, 110:25332–25338, 2006.

[50] F. Zernike and J. E. Midwinter. *Applied Nonlinear Optics*. Wiley series in pure and applied optics. John Wiley & Sons, New York, 1973.

[51] J. Shah. Ultrafast luminescence spectroscopy using sum frequency generation. *IEEE J. Quantum Electron.*, 24(2):276–288, 1988.

[52] J. S. Steckel, S. Coe-Sullivan, V. Bulović, and M. G. Bawendi. 1.3 μm to 1.55 μm tunable electroluminescence from pbse quantum dots embedded within an organic device. *Adv. Mater.*, 15:1862–1866, 2003.

[53] J. M. Pietryga, D. J. Werder, D. J. Williams, J. L. Casson, R. D. Schaller, V. I. Klimov, and J. A. Hollingsworth. Utilizing the lability of lead selenide to produce heterostructured nanocrystals with bright, stable infrared emission. *J. Am. Chem. Soc.*, 130:4879–4885, 2008.

[54] L. Cademartiri, E. Montanari, G. Calestani, A. Migliori, A. Guagliardi, and G. A. Ozin. Size-dependent extinction coefficients of pbs quantum dots. *J. Am. Chem. Soc.*, 128(31):10337–10346, 2006.

[55] J.S. Steckel. *The Synthesis of Inorganic Semiconductor Nanocrystalline Materials for the Purpose of Creating Hybrid Organic/Inorganic Light-Emitting Devices*. PhD thesis, Massachusetts Institute of Technology, 2006.

[56] M. T. Trinh, A. J. Houtepen, J. M. Schins, T. Hanrath, J. Piris, W. Knulst, A. P. L. M. Goossens, and L. D. A. Siebbeles. In spite of recent doubts carrier multiplication does occur in pbse nanocrystals. *Nano Letters*, 8:1713–1718, 2008.

[57] J. A. McGuire, J. Joo, J. M. Pietryga, R. D. Schaller, and V. I. Klimov. New aspects of carrier multiplication in semiconductor nanocrystals. *Acc. Chem. Res.*, 41:1810–1819, 2008.

[58] M. C. Beard, A. G. Midgett, M. Law, O. E. Semonin, R. J. Ellingson, and A. J. Nozik. Variations in the quantum efficiency of multiple exciton generation for a series of chemically treated pbse nanocrystal films. *Nano Lett.*, 9:836–845, 2009.

[59] M. Ji, S. Park, S. T. Connors, T. Mokari, Y. Cui, and K. J. Gaffney. Efficient multiple exciton generation observed in colloidal pbse quantum dots with temporally and spectrally resolved intraband excitation. *Nano Lett.*, 9:1217–1222, 2009.

[60] A. Smith and D. Dutton. Behavior of lead sulfide photocells in the ultraviolet. *Journal of the Optical Society of America*, 48:1007, 1958.

[61] G. Nair, S. G. Geyer, L.-Y. Chang, and M. G. Bawendi. Carrier multiplication yields in pbs and pbse nanocrystals measured by transient photoluminescence. *Phys. Rev. B*, 78:125325, 2008.

[62] R. H. Bube. *Photoelectronic Properties of Semiconductors*. Cambridge University Press, 1992.

[63] A. L. Fetter and J. D. Walecka. *Quantum Theory of Many-Particle Systems*. Dover, 2003.

[64] G. C. Schatz and M. A. Ratner. *Quantum Mechanics in Chemistry*. Dover, 2002.

[65] M. O. Scully and M. S. Zubairy. *Quantum Optics*. Cambridge University Press, 1997.

[66] R. D. Schaller, V. M. Agranovich, and V. I. Klimov. High-efficiency carrier multiplication through direct photogeneration of multi-excitons via virtual single-exciton states. *Nat. Phys.*, 1:189–194, 2005.

[67] C. M. Isborn, S. V. Kilina, X. Li, and O. V. Prezhdo. Generation of multiple excitons in pbse and cdse quantum dots by direct photoexcitation: First-principles calculations on small pbse and cdse clusters. *J. Phys. Chem. C.*, 112:18291–18294, 2008.

[68] A. Shabaev, Al. L. Efros, and A. J. Nozik. Multiexciton generation by a single photon in nanocrystals. *Nano Lett.*, 6:2856–2863, 2006.

[69] A. Franceschetti, J.M. An, and A. Zunger. Impact ionization can explain carrier multiplication in pbse quantum dots. *Nano Lett.*, 6:2191–2195, 2006.

[70] G. Allan and C. Delerue. Role of impact ionization in multiple exciton generation in pbse nanocrystals. *Phys. Rev. B*, 73:205423, 2006.

[71] G. Allan and C. Delerue. Influence of electronic structure and multiexciton spectral density on multiple-exciton generation in semiconductor nanocrystals: Tight-binding calculations. *Physical Review B*, 77:125340, 2008.

[72] E. Rabani and R. Baer. Distribution of carrier multiplication rates in cdse and inas nanocrystals. *Nano Lett.*, 8:4488–4492, 2008.

[73] R. D. Schaller, J. M. Pietryga, S. V. Goupalov, M. A. Petruska, S. A. Ivanov, and V. I. Klimov. Breaking the phonon bottleneck in semiconductor nanocrystals via multiphonon emission induced by intrinsic nonadiabatic interactions. *Phys. Rev. Lett.*, 95:196401, 2005.

[74] C. Bonati, A. Cannizzo, D. Tonti, A. Tortschanoff, F. van Mourik, and M. Chergui. Subpicosecond near-infrared fluorescence upconversion study of relaxation processes in pbse quantum dots. *Physical Review B*, 76:033304, 2007.

[75] G. Allan and C. Delerue. Fast relaxation of hot carriers by impact ionization in semiconductor nanocrystals: Role of defects. *Phys. Rev. B*, 79:195324, 2009.

[76] V. I. Rupasov and V. I. Klimov. Carrier multiplication in semiconductor nanocrystals via intraband optical transitions involving virtual biexciton states. *Phys. Rev. B*, 76:125321, 2007.

[77] B. Lounis and M. Orrit. Single-photon sources. *Rep. Prog. Phys.*, 68:1129–1179, 2005.

[78] Z. Yuan, B. E. Kardynal, R. M. Stevenson, A. J. Shields, C. J. Lobo, K. Cooper, N. S. Beattie, D. A. Ritchie, and M. Pepper. Electrically driven single-photon source. *Science*, 295:102–105, 2002.

[79] H. J. Kimble, M. Dagenais, and L. Mandel. Photon antibunching in resonance fluorescence. *Phys. Rev. Lett.*, 39:691, 1977.

[80] R. M. Thompson, R. M. Stevenson, A. J. Shields, I. Farrer, C. J. Lobo, D. A. Ritchie, M. L. Leadbeater, and M. Pepper. Single-photon emission from exciton complexes in individual quantum dots. *Phys. Rev. B*, 64:201302, 2001.

[81] B. Mahler, P. Spinicelli, S. Buil, X. Quelin, J.-P. Hermier, and B. Dubertret. Towards non-blinking colloidal quantum dots. *Nature Materials*, 7:659–664, 2008.

[82] P. Spinicelli, S. Buil, X. Quélin, B. Mahler, B. Dubertret, and J.-P. Hermier. Bright and grey states in cdse-cds nanocrystals exhibiting strongly reduced blinking. *Phys. Rev. Lett.*, 102:136801, 2009.

[83] X. Wang, X. Ren, K. Kahen, M. A. Hahn, M. Rajeswaran, S. Maccagnano-Zacher, J. Silcox, G. E. Cragg, A. L. Efros, and T. D. Krauss. Non-blinking semiconductor nanocrystals. *Nature*, 459:686–689, 2009.

[84] C. Santori, D. Fattal, J. Vuckovic, G. S. Solomon, and Y. Yamamoto. Single-photon generation with inas quantum dots. *New J. Phys.*, 6:1–16, 2004.

[85] Y. Chen, J. Vela, H. Htoon, J. L. Casson, D. J. Werder, D. A. Bussian, V. I. Klimov, and J. A. Hollingsworth. "giant" multishell cdse nanocrystal quantum dots with suppressed blinking. *J. Am. Chem. Soc.*, 130:5026–5027, 2008.

[86] F. García-Santamaría, Y. Chen, J. Vela, R. D. Schaller, J. A. Hollingsworth, and V. I. Klimov. Suppressed auger recombination in "giant" nanocrystals boosts optical gain performance. *Nano Lett.*, ASAP:doi:10.1021/nl901681d, 2009.

[87] M. Dahan, L. Sabine, C. Luccardini, P. Rostaing, B. Riveau, and A. Triller. Diffusion dynamics of glycine receptors revealed by single-quantum dot tracking. *Science*, 302:442–445, 2003.

[88] M. Kuno, D.P. Fromm, H.F. Hafmann, A. Gallagher, and D.J. Nesbitt. Non-exponential "blinking" kinetics of single cdse quantum dots: A universal power law behavior. *J. Chem. Phys.*, 112(7):3117, 2000.

[89] K.T. Shimizu, R.G. Neuhauser, C. A. Leatherdale, S.A. Empedocles, W.K. Woo, and M. G. Bawendi. Blinking statistics in single semiconductor nanocrystal quantum dots. *Phys. Rev. B*, 63:205316, 2001.

[90] F. D. Stefani, W. Knoll, M. Kreiter, X. Zhong, and M. Y. Han. Quantification of photoinduced and spontaneous quantum-dot luminescence blinking. *Phys. Rev. B*, 72(12):125304, 2005.

[91] A. Isaac, C. von Borczyskowski, and F. Cichos. Correlation between photo-luminescence intermittency of cdse quantum dots and self-trapped states in dielectric media. *Phys. Rev. B*, 71:161302(R), 2005.

[92] F. Cichos, J. Martin, and C. von Borczyskowski. Emission intermittency in silicon nanocrystals. *Phys. Rev. B*, 70:115314, 2005.

[93] Rogier Verberk, Antoine M. van Oijen, and Michael Orrit. Simple model for the power-law blinking of single semiconductor nanocrystals. *Phys. Rev. B*, 66:233202, 2002.

[94] M. Kuno, D.P. Fromm, S.T. Johnson, A. Gallagher, and D.J. Nesbitt. Modeling distributed kinetics in isolated semiconductor quantum dots. *Phys. Rev. B*, 67:125304, 2003.

[95] J. Tang and R. A. Marcus. Mechanisms of fluorescence blinking in semiconductor nanocrystal quantum dots. *J. Chem. Phys.*, 123(5):054704, 2005.

[96] P. A. Frantsuzov and R. A. Marcus. Explanation of quantum dot blinking without the long-lived trap hypothesis. *Phys. Rev. B*, 72(15):155321, 2005.

[97] M. Shim, C. Wang, and P. Guyot-Sionnest. Charge-tunable optical properties in colloidal semiconductor nanocrystals. *J. Phys. Chem. B*, 105:2369–2373, 2001.

[98] W.K. Woo, K.T. Shimizu, M. V. Jarosz, R.G. Neuhauser, C. A. Leatherdale, M.A. Rubner, and M. G. Bawendi. Reversible charging of cdse nanocrystals in a simple solid-state device. *Adv. Mater.*, 14(15):1068–1071, 2002.

[99] C. Wang, B. L. Wehrenberg, C. Y. Woo, and P. Guyot-Sionnest. Light emission and amplification in charged cdse quantum dots. *J. Phys. Chem. B*, 108:9027–9031, 2004.

[100] P. P. Jha and P. Guyot-Sionnest. Trion decay in colloidal quantum dots. *ACS Nano*, 3:1011–1015, 2009.

[101] T. D. Krauss, S. O'Brien, and L.E. Brus. Charge and photoionization properties of single semiconductor nanocrystals. *J. Phys. Chem. B*, 105:1725–1733, 2001.

[102] O. Cherniavskaya, L. Chen, and L.E. Brus. Imaging the photoionization of individual cdse/cds core-shell nanocrystals on n- and p-type silicon substrates with thin oxides. *J. Phys. Chem. B*, 108:4946–4961, 2004.

[103] C. Bonati, M.B. Mohamed, D. Tonti, G. Zgrablic, S. Haacke, F. van Mourik, and M. Chergui. Spectral and dynamical characterization of multiexcitons in colloidal cdse semiconductor quantum dots. *Phys. Rev. B*, 71:205317, 2005.

[104] A. Franceschetti and M. C. Troparevsky. Radiative recombination of triexcitons in cdse colloidal quantum dots. *J. Phys. Chem. C.*, 111:6154–6157, 2007.

[105] V. I. Klimov, J. A. McGuire, R. D. Schaller, and V. I. Rupasov. Scaling of multiexciton lifetimes in semiconductor nanocrystals. *Phys. Rev. B*, 77:195324, 2008.

[106] J. Tang and R. A. Marcus. Diffusion-controlled electron transfer processes and power-law statistics of fluorescence intermittency of nanoparticles. *Phys. Rev. Lett.*, 95(10):107401, 2005.

[107] D. J. Norris and M. G. Bawendi. Measurement and assignment of the size-dependent optical spectrum in cdse quantum dots. *Phys. Rev. B*, 53(24):16338–16346, 1996.

Gautham Padmanabhan Nair

Education

Massachusetts Institute of Technology. *Ph.D. in Chemistry, September 2009.*

Thesis work focused on laser-based assessment of the potential of a promising class of semiconductor nanomaterials in third generation solar cells and optical microscopy of single quantum emitters.

Involved in a range of multidisciplinary projects either directly as a specialist in optical materials characterization, or through informal discussions, active participation in meetings, mentorship, and teaching.

Relevant courses: Theory of Solids, Electromagnetism, Nonlinear Optics, Sustainable Energy. Term paper subject - Economic Impacts of a Carbon Tax in the Manufacturing Sector. *GPA: 4.8/5.0*

California Institute of Technology. *Bachelor of Science with Honors, Chemical Engineering (Materials), June 2004.* Conducted research through the Summer Undergraduate Research Fellowship program in 2001, 2002 and 2003 on several topics:

- Magnetic resonance study of the shape of small molecules

- Spectroscopic studies of a chemical reaction important to the atmosphere

- Electrochemistry of nanoporous silicon

Relevant courses: Thermodynamics, Transport Phenomena, Electronic Properties of Materials, Applied Mathematics, Computer Science, Quantum Mechanics, Spectroscopy, Optimal Design of Chemical Systems, Finance, Macroeconomics, Game Theory. *GPA: 4.2/4.3*

Experience

Teaching Assistant, Statistical Mechanics. *Department of Chemistry, MIT, 2005.* As the only TA for the class, gave several recitation and tutorial sessions a week throughout the semester, prepared detailed solution sets and supplementary notes, and contributed exam questions. Given an award in connection with this work (see below).

Treasurer, Mexican Student Association. *MIT, July 2007- August 2009.* Wrote proposals, negotiated with internal funding sources, and secured reimbursements. Assisted in planning and executing cultural events and academic seminars.

Awards

Robert T. Haslam Presidential Graduate Fellowship for outstanding undergraduate record, exceptional background, and promising future (MIT, 2004); **Department of Chemistry Award** for outstanding teaching by a graduate student (MIT, 2005); **Richard P. Schuster Memorial Prize** for academic promise in a junior or senior in chemistry or chemical engineering (Caltech, 2004); **John Stauffer Merit Scholarship** (Caltech, 2003 and 2004)

SKILLS & PERSONAL

Equipment   Confocal microscopy, Time-resolved and standard optical spectroscopy.

Software   MATLAB, LabVIEW, LaTeX, MS Office.

Languages   English and Spanish (both native fluency). French (familiar)

REFEREED PAPERS

Nair G, Geyer SM, Chang LY, Bawendi MG. Carrier multiplication yields in PbS and PbSe nanocrystals measured by transient photoluminescence. *Physical Review B* 78:125325. (2008)

Nair G, Bawendi MG. Carrier multiplication yields of CdSe and CdTe nanocrystals by transient photoluminescence spectroscopy. *Physical Review B* 76: 081304(R). (2007)

Nair G, Roberts JD. Conformations of 2-Carboxy-1,4-butanedioic Acid as a Function of Ionization State in Dimethyl Sulfoxide. *Organic Letters* 5: 3699-3701 (2003)

Huang H, Dorn A, Nair G, Bulovic V, Bawendi MG. Bias induced photoluminescence quenching of single colloidal quantum dots embedded in organic semiconductors. *Nano Letters* 7: 3781 - 3786. (2007)

Snee PT, Somers RC, Nair GP, Zimmer JP, Bawendi MG, Nocera DG. A Ratiometric CdSe/ZnS Nanocrystal pH Sensor. *Journal of the American Chemical Society* 128: 13320-13321. (2006)

Chan YT, Snee PT, Caruge J-M, Yen BK, Nair GP, Nocera DG, Bawendi MG. A Solvent Stable Nanocrystal-Silica Composite Laser. *Journal of the American Chemical Society*, 128: 3146-3147 (2006)

Bean BD, Mollner AK, Nizkorodov SA, Nair G, Okumura M., Sander SP, Peterson KA, Francisco JS. Cavity Ringdown Spectroscopy of cis-cis HOONO and the HOONO/HONO$_2$ Branching Ratio in the Reaction OH+NO$_2$+M. *Journal of Physical Chemistry A* 107, 6974-6985 (2003)